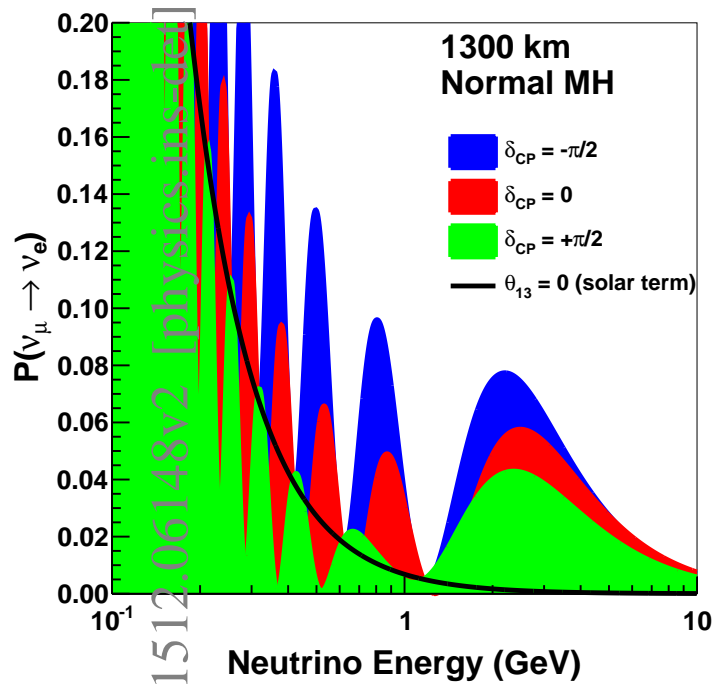# Long-Baseline Neutrino Facility (LBNF) and Deep Underground Neutrino Experiment (DUNE)

Conceptual Design Report

Volume 2: The Physics Program for DUNE at LBNF

January 25, 2016

DEEP UNDERGROUND
NEUTRINO EXPERIMENT

The DUNE Collaboration

R. Acciarri[43], M. A. Acero[10], M. Adamowski[43], C. Adams[144], P. Adamson[43], S. Adhikari[77], Z. Ahmad[135],
C. H. Albright[43], T. Alion[120], E. Amador[131], J. Anderson[8], K. Anderson[43], C. Andreopoulos[76], M. Andrews[43],
R. Andrews[43], I. Anghel[62], J. d. Anjos[99], A. Ankowski[137], M. Antonello[72], A. Aranda Fernandez[31], A. Ariga[13],
T. Ariga[13], D. Aristizabal[75], E. Arrieta-Diaz[87], K. Aryal[131], J. Asaadi[129], D. Asner[103], M. S. Athar[6], M. Auger[13],
A. Aurisano[29], V. Aushev[68], D. Autiero[63], M. Avila[131], J. J. Back[139], X. Bai[122], B. Baibussinov[106], M. Baird[61],
A. B. Balantekin[142], B. Baller[43], P. Ballett[41], B. Bambah[52], M. Bansal[107], S. Bansal[107], G. J. Barker[139],
W. A. Barletta[83], G. Barr[102], N. Barros[109], L. Bartoszek[78], A. Bashyal[131], M. Bass[102], F. Bay[133], J. Beacom[100],
B. R. Behera[107], G. Bellettini[110], V. Bellini[26], O. Beltramello[16], P. A. Benetti[108], A. Bercellie[114], M. Bergevin[19],
E. Berman[43], H. Berns[20], R. Bernstein[43], S. Bertolucci[16], B. Bhandari[49], V. Bhatnagar[107], B. Bhuyan[60], J. Bian[90],
K. Biery[43], M. Bishai[15], T. Blackburn[128], A. Blake[73], F. d. M. Blaszczyk[14], E. Blaufuss[82], B. Bleakley[124],
E. Blucher[28], V. Bocean[43], F. Boffelli[108], J. Boissevain[78], S. Bolognesi[117], T. Bolton[65], M. Bonesini[89], T. Boone[33],
C. Booth[118], S. Bordoni[53], M. Borysova[68], B. Bourguille[53], S. B. Boyd[139], D. Brailsford[73], A. Brandt[131],
J. Bremer[16], S. Brice[43], C. Bromberg[87], G. Brooijmans[34], G. Brown[131], R. Brown[15], G. Brunetti[43], X. Bu[43],
N. Buchanan[33], H. Budd[114], B. Bugg[130], P. Calafiura[74], E. Calligarich[108], E. Calvo[17], L. Camilleri[34],
M. Campanelli[77], C. Cantini[147], B. Carls[43], R. Carr[34], M. Cascella[77], C. Castromonte[44], E. Catano Mur[62],
F. Cavanna[43], S. Centro[106], A. Cervera Villanueva[136], V. B. Chandratre[12], A. Chatterjee[131], S. Chattopadhyay[43],
S. Chattopadhyay[135], L. Chaussard[63], S. Chembra[52], H. Chen[15], K. Chen[15], M. Chen[21], D. Cherdack[33], C. Chi[34],
S. Childress[43], S. Choubey[47], B. C. Choudhary[38], G. Christodoulou[76], C. Christofferson[122], E. Church[103],
D. Cianci[81], D. Cline[21], T. Coan[125], A. Cocco[93], J. Coelho[134], P. Cole[58], G. Collin[83], J. M. Conrad[83],
M. Convery[115], R. Corey[122], L. Corwin[122], J. Cranshaw[8], P. Crivelli[147], D. Cronin-Hennessy[90], A. Curioni[89],
J. Cushing[28], D. L. Adams[15], D. Dale[58], S. R. Das[60], T. Davenne[116], G. S. Davies[61], J. Davies[128], J. Dawson[2],
K. De[131], A. de Gouvea[97], J. K. de Jong[102], P. de Jong[92], P. De Lurgio[8], M. Decowski[92], A. Delbart[117],
C. Densham[116], R. Dharmapalan[8], N. Dhingra[107], S. Di Luise[147], M. Diamantopoulou[9], J. S. Diaz[61],
G. Diaz Bautista[114], M. Diwan[15], Z. Djurcic[8], J. Dolph[15], G. Drake[8], D. Duchesneau[71], M. Duvernois[142],
H. Duyang[120], D. A. Dwyer[74], S. Dye[48], S. Dytman[111], B. Eberly[115], R. Edgecock[50], D. Edmunds[87], S. Elliott[78],
M. Elnimr[21], S. Emery[117], E. Endress[105], S. Eno[82], A. Ereditato[13], C. O. Escobar[43], J. Evans[81], A. Falcone[108],
L. Falk[128], A. Farbin[131], C. Farnese[106], Y. Farzan[57], A. Fava[106], L. Favilli[18], J. Felde[82], J. Felix[46], S. Fernandes[4],
L. Fields[43], A. Finch[73], M. Fitton[116], B. Fleming[144], T. Forest[58], J. Fowler[40], W. Fox[61], J. Fried[15], A. Friedland[78],
S. Fuess[43], B. Fujikawa[74], A. Gago[105], H. Gallagher[134], S. Galymov[63], T. Gamble[118], R. Gandhi[47],
D. Garcia-Gamez[81], S. Gardiner[20], G. Garvey[78], V. M. Gehman[74], A. Gendotti[147], G. d. Geronimo[15], C. Ghag[77],
P. Ghoshal[47], D. Gibin[106], I. Gil-Botella[17], R. Gill[15], D. Girardelli[25], A. Giri[55], S. Glavin[109], D. Goeldi[13],
S. Golapinni[65], M. Gold[96], R. A. Gomes[44], J. J. Gomez Cadenas[136], M. C. Goodman[8], D. Gorbunov[56],
S. Goswami[47], N. Graf[111], N. Graf[115], M. Graham[115], E. Gramelini[144], R. Gran[91], C. Grant[20], N. Grant[139],
V. Greco[26], H. Greenlee[43], L. Greenler[142], C. Greenley[79], M. Groh[29], S. Grullon[109], T. Grundy[73], K. Grzelak[138],
E. Guardincerri[78], V. Guarino[8], E. Guarnaccia[137], G. P. Guedes[42], R. Guenette[102], A. Guglielmi[106], A. T. Habig[91],
R. W. Hackenburg[15], A. Hackenburg[144], H. Hadavand[131], R. Haenni[13], A. Hahn[43], M. D. Haigh[139], T. Haines[78],
T. Hamernik[43], T. Handler[130], S. Hans[15], D. Harris[43], J. Hartnell[128], T. Hasegawa[67], R. Hatcher[43],
A. Hatzikoutelis[130], S. Hays[43], E. Hazen[14], M. Headley[123], A. Heavey[43], K. Heeger[144], J. Heise[123], K. Hennessy[76],
J. Hewes[81], A. Higuera[49], T. Hill[58], A. Himmel[43], M. Hogan[33], P. Holanda[25], A. Holin[77], W. Honey[73],
S. Horikawa[147], G. Horton-Smith[65], B. Howard[61], J. Howell[43], P. Hurh[43], J. Huston[87], J. Hylen[43], R. Imlay[79],
J. Insler[79], G. Introzzi[108], D. Ioanisyan[145], A. Ioannisian[145], K. Iwamoto[114], A. Izmaylov[136], C. Jackson[131],
D. E. Jaffe[15], C. James[43], E. James[43], F. Jediny[36], C. Jen[137], A. Jhingan[107], S. Jiménez[17], J. H. Jo[127],
M. Johnson[43], R. Johnson[29], J. Johnstone[43], B. J. Jones[83], J. Joshi[15], H. Jostlein[43], C. K. Jung[127], T. Junk[43],
A. Kaboth[59], R. Kadel[74], T. Kafka[134], L. Kalousis[137], Y. Kamyshkov[130], G. Karagiorgi[81], D. Karasavvas[9],
Y. Karyotakis[71], A. Kaur[107], P. Kaur[107], B. Kayser[43], N. Kazaryan[145], E. Kearns[14], P. Keener[109], S. Kemboi[131],
E. Kemp[25], S. H. Kettell[15], M. Khabibullin[56], M. Khandaker[58], A. Khotjantsev[56], B. Kirby[15], M. Kirby[43],
J. Klein[109], T. Kobilarcik[43], S. Kohn[19], G. Koizumi[43], A. Kopylov[56], M. Kordosky[141], L. Kormos[73], U. Kose[16],
V. A. Kostelecký[61], M. Kramer[19], I. Kreslo[13], R. Kriske[90], W. Kropp[21], Y. Kudenko[56], V. A. Kudryavtsev[118],
S. Kulagin[56], A. Kumar[107], G.K. Kumar[69], J. Kumar[48], L. Kumar[107], T. Kutter[79], A. Laminack[4], K. Lande[109],
C. Lane[39], K. Lang[132], F. Lanni[15], J. Learned[48], P. Lebrun[43], D. Lee[78], H. Lee[114], K. Lee[21], W. M. Lee[43],
M. A. Leigui de Oliveira[1], Q. Li[43], S. Li[15], S. Li[100], X. Li[127], Y. Li[15], Z. Li[40], J. Libo[120], C. S. Lin[74], S. Lin[33],
J. Ling[15], J. Link[137], Z. Liptak[32], D. Lissauer[15], L. Littenberg[15], B. Littlejohn[54], Q. Liu[78], T. Liu[125], S. Lockwitz[43],
N. Lockyer[43], T. Loew[74], M. Lokajicek[3], K. Long[59], M. D. L. Lopes[43], J. P. Lopez[32], J. Losecco[98], W. Louis[78],

J. Lowery[61], M. Luethi[13], K. B. Luk[19], B. Lundberg[43], T. Lundin[43], X. Luo[144], T. Lux[53], J. Lykken[43],
A. A. Machado[72], J. R. Macier[43], S. Magill[8], G. Mahler[15], K. Mahn[87], M. Malek[59], S. Malhotra[12], D. Malon[8],
F. Mammoliti[26], S. Mancina[8], S. K. Mandal[38], S. Mandodi[52], S. L. Manly[114], A. Mann[134], A. Marchionni[43],
W. Marciano[15], C. Mariani[137], J. Maricic[48], A. Marino[32], M. Marshak[90], C. Marshall[114], J. Marshall[24],
J. Marteau[63], J. Martin-Albo[102], D. Martinez[54], S. Matsuno[48], J. Matthews[79], C. Mauger[78], K. Mavrokoridis[76],
D. Mayilyan[145], E. Mazzucato[117], N. McCauley[76], E. McCluskey[43], N. McConkey[118], K. McDonald[112],
K. S. McFarland[114], A. M. McGowan[114], C. McGrew[127], R. McKeown[141], D. McNulty[58], R. McTaggart[124],
A. Mefodiev[56], M. Mehrian[33], P. Mehta[95], D. Mei[121], O. Mena[136], S. Menary[146], H. Mendez[85], A. Menegolli[108],
G. Meng[106], Y. Meng[21], H. Merritt[59], D. Mertins[4], M. Messier[61], W. Metcalf[79], M. Mewes[61], H. Meyer[140],
T. Miao[43], R. Milincic[48], W. Miller[90], G. Mills[78], O. Mineev[56], O. Miranda[30], C. S. Mishra[43], S. R. Mishra[120],
B. Mitrica[51], D. Mladenov[16], I. Mocioiu[104], R. Mohanta[52], N. Mokhov[43], C. Montanari[16], D. Montanari[43],
J. Moon[83], M. Mooney[15], C. Moore[43], J. Morfin[43], B. Morgan[139], C. Morris[49], W. Morse[15], Z. Moss[83], C. Mossey[43],
C. A. Moura[1], J. Mousseau[86], L. Mualem[23], M. Muether[140], S. Mufson[61], S. Murphy[147], J. Musser[61], R. Musser[131],
Y. Nakajima[74], D. Naples[111], J. Navarro[10], D. Navas[17], J. Nelson[141], M. Nessi[16], M. Newcomer[109], Y. Ng[131],
R. Nichol[77], T. C. Nicholls[116], K. Nikolics[147], E. Niner[61], B. Norris[43], F. Noto[16], P. Novakova[15], P. Novella[136],
J. Nowak[73], M. S. Nunes[25], H. O'Keeffe[73], R. Oldeman[24], R. Oliveira[25], T. Olson[134], Y. Onishchuk[68], J. Osta[43],
T. Ovsjannikova[56], B. Page[87], S. Pakvasa[48], S. Pal[118], O. Palamara[43], A. Palazzo[84], J. Paley[43], C. Palomares[17],
E. Pantic[20], V. Paolone[111], V. Papadimitriou[43], J. Park[137], S. Parke[43], Z. Parsa[15], S. Pascoli[41], R. Patterson[23],
S. Patton[74], T. Patzak[2], B. Paulos[142], L. Paulucci[1], Z. Pavlovic[43], G. Pawloski[90], S. Peeters[128], E. Pennacchio[63],
A. Perch[77], G. N. Perdue[43], L. Periale[147], J. D. Perkin[118], H. Pessard[71], G. Petrillo[43], R. Petti[120], A. Petukhov[122],
F. Pietropaolo[106], R. Plunkett[43], S. Pordes[43], M. Potekhin[15], R. Potenza[26], B. Potukuchi[64], N. Poudyal[121],
O. Prokofiev[43], N. Pruthi[107], P. Przewlocki[94], D. Pushka[43], X. Qian[15], J. L. Raaf[43], R. Raboanary[7], V. Radeka[15],
A. Radovic[141], G. Raffelt[84], I. Rakhno[43], H. T. Rakotondramanana[7], L. Rakotondravohitra[7], Y. A. Ramachers[139],
R. Rameika[43], J. Ramsey[78], A. Rappoldi[108], G. Raselli[108], P. Ratoff[73], B. Rebel[43], C. Regenfus[147],
J. Reichenbacher[122], D. Reitzner[43], A. Remoto[71], A. Renshaw[49], S. Rescia[15], M. Richardson[118], K. Rielage[78],
K. Riesselmann[43], M. Robinson[118], L. Rochester[115], O. B. Rodrigues[25], P. Rodrigues[114], B. Roe[86], M. Rosen[48],
R. M. Roser[43], M. Ross-Lonergan[41], M. Rossella[108], A. Rubbia[147], C. Rubbia[45], R. Rucinski[43],
C. Rudolph von Rohr[13], B. Russell[144], D. Ruterbories[114], R. Saakyan[77], N. Sahu[55], P. Sala[88], N. Samios[15],
F. Sanchez[53], M. Sanchez[62], B. Sands[112], S. Santana[85], R. Santorelli[17], G. Santucci[127], N. Saoulidou[9],
A. Scaramelli[88], H. Schellman[101], P. Schlabach[43], R. Schmitt[43], D. Schmitz[28], J. Schneps[134], K. Scholberg[40],
A. Schukraft[43], J. Schwehr[33], E. Segreto[72], S. Seibert[109], J. A. Sepulveda-Quiroz[62], F. Sergiampietri[147],
L. Sexton-Kennedy[43], D. Sgalaberna[147], M. Shaevitz[34], J. Shahi[107], S. Shahsavarani[131], P. Shanahan[43],
S. U. Shankar[47], R. Sharma[15], R. K. Sharma[113], T. Shaw[43], R. Shrock[127], I. Shyrma[68], N. Simos[15], G. Sinev[40],
I. Singh[107], J. Singh[107], J. Singh[80], V. Singh[11], G. Sinnis[78], W. Sippach[34], D. Smargianaki[16], M. Smy[21],
E. Snider[43], P. Snopok[54], J. Sobczyk[143], H. Sobel[21], M. Soderberg[129], N. Solomey[140], W. Sondheim[78], M. Sorel[136],
A. Sousa[29], K. Soustruznik[27], J. Spitz[86], N. J. Spooner[118], M. Stancari[43], I. Stancu[4], D. Stefan[16], H. M. Steiner[74],
J. Stewart[15], J. Stock[122], S. Stoica[51], J. Stone[14], J. Strait[43], M. Strait[28], T. Strauss[43], S. Striganov[43], R. Sulej[94],
G. Sullivan[82], Y. Sun[48], L. Suter[8], C. M. Sutera[26], R. Svoboda[20], B. Szczerbinska[37], A. Szelc[81],
S. Söldner-Rembold[81], R. Talaga[8], M. Tamsett[128], S. Tariq[43], E. Tatar[58], R. Tayloe[61], C. Taylor[78], D. Taylor[123],
K. Terao[34], M. Thiesse[118], J. Thomas[77], L. F. Thompson[118], M. Thomson[24], C. Thorn[15], M. Thorpe[116], X. Tian[120],
D. Tiedt[122], S. C. Timm[43], A. Tonazzo[2], T. Tope[43], A. Topkar[12], F. R. Torres[25], M. Torti[108], M. Tortola[136],
F. Tortorici[26], M. Toups[83], C. Touramanis[76], M. Tripathi[20], I. Tropin[43], Y. Tsai[115], K. V. Tsang[74], R. Tsenov[119],
S. Tufanli[144], C. Tull[74], J. Turner[41], M. Tzanov[79], E. Tziaferi[9], Y. Uchida[59], J. Urheim[61], T. Usher[115], M. Vagins[66],
P. Vahle[141], G. A. Valdiviesso[5], L. Valerio[43], Z. Vallari[127], J. Valle[136], R. Van Berg[109], R. Van de Water[78],
P. Van Gemmeren[8], F. Varanini[106], G. Varner[48], G. Vasseur[117], K. Vaziri[43], G. Velev[43], S. Ventura[106],
A. Verdugo[17], T. Viant[147], T. V. Vieira[25], C. Vignoli[72], C. Vilela[127], B. Viren[15], T. Vrba[36], T. Wachala[70],
D. Wahl[142], M. Wallbank[118], N. Walsh[20], B. Wang[125], H. Wang[22], L. Wang[121], T. Wang[41], T.K. Warburton[118],
D. Warner[33], M. Wascko[59], D. Waters[77], T. B. Watson[131], A. Weber[116], M. Weber[13], W. Wei[121], A. Weinstein[62],
D. Wells[122], D. Wenman[142], M. Wetstein[62], A. White[131], L. Whitehead[49], D. Whittington[61], M. Wilking[127],
J. Willhite[43], P. Wilson[43], R. J. Wilson[33], L. Winslow[83], P. Wittich[35], S. Wojcicki[126], H. H. Wong[19], K. Wood[120],
E. Worcester[15], M. Worcester[15], S. Wu[147], T. Xin[62], C. Yanagisawa[127], S. Yang[29], T. Yang[43], K. Yarritu[78], J. Ye[125],
M. Yeh[15], N. Yershov[56], K. Yonehara[43], B. Yu[15], J. Yu[131], J. Zalesak[3], A. Zalewska[70], B. Zamorano[128], L. Zang[118],
A. Zani[16], G. Zavala[46], G. Zeller[43], C. Zhang[15], C. Zhang[121], E. D. Zimmerman[32], M. Zito[117], and R. Zwaska[43]

[1] *ABC Federal University, Santo André –SP, 09210-580, Brazil*
[2] *APC-Paris, Batiment Condorcet; 10, rue Alice Domon et L'eonie Duquet; F-75205 Paris CEDEX 13, France*
[3] *Institute of Physics ASCR, v. v. i. , Na Slovance 2; 182 21 Praha 8, Czech Republic*
[4] *University of Alabama (Tuscaloosa), Tuscaloosa, AL 35487-0324, USA*
[5] *University Federal de Alfenas em Poços de Caldas, 11999, CEP 37715-900 Poços de Caldas-MG, Brazil*

2

[6] *Aligarh Muslim University, Department of Physics Aligarh-202002, India*

[7] *Antananarivo, Présidence de l'Université d'Antananarivo: BP 566, Antananarivo 101, Madagascar*

[8] *Argonne National Lab., Argonne, IL 60439, USA*

[9] *University of Athens, University Campus, Zografou GR 157 84 Greece, Greece*

[10] *Universidad del Atlantico, Km 7 antigua vi a Puerto Colombia, Barranquilla, Colombia*

[11] *Banaras Hindu University, Dept. of Physics, Varanasi UP 221005, India*

[12] *Bhabha Atmoic Research Center, Trombay, Mumbai, India*

[13] *University of Bern, Lab for High Energy Physics; Sidlerstrasse 5; CH-3012 Bern, Switzerland*

[14] *Boston University, Boston, MA 02215, USA*

[15] *Brookhaven National Lab., Upton, NY 11973-5000, USA*

[16] *CERN, European Organization for Nuclear Research European Laboratory for Particle Physics; 1211 Gen'eve 23, Switzerland*

[17] *CIEMAT, División de Física de Partículas; Avenida Complutense 40; E-28040 Madrid, Spain*

[18] *CNR Pisa, 1, 56124 Pisa PI, Italy*

[19] *University of California (Berkeley), Berkeley, CA 94720-7300, USA*

[20] *University of California (Davis), Davis, CA 95616, USA*

[21] *University of California (Irvine), Irvine, CA 92697-4575, USA*

[22] *University of California (Los Angeles), Los Angeles, CA 90095-1547, USA*

[23] *California Inst. of Tech., MC 356-48; Pasadena, CA 91125, USA*

[24] *University of Cambridge, JJ Thomson Avenue, Cambridge CB3 0HE, UK*

[25] *University de Campinas, Av. Sérgio Buarque de Holanda, 777 CEP 13083-859 Campinas-SP, Brazil*

[26] *University di Catania, Via Santa Sofia, I-95123 Catania, Italy*

[27] *Institute of Particle and Nuclear Physics of the Faculty of Mathematics and Physics of the Charles University in Prague, V Holešovičkách 747/2; 180 00 Praha 8-Libeň, Czech Republic*

[28] *University of Chicago, Chicago, IL 60637-1434, USA*

[29] *University of Cincinnati, Cincinnati, OH 45221-0011, USA*

[30] *Cinvestav, 07360 Ciudad de México, D.F., Mexico*

[31] *Universidad de Colima, Facultad de Ciencias Bernal Diaz del Castillo 340 Colonia Villa San Sebastian Colima, Colima, Mexico*

[32] *University of Colorado, Boulder, CO 80309, USA*

[33] *Colorado State University, Fort Collins, CO 80523, USA*

[34] *Columbia University, New York, NY 10027, USA*

[35] *Cornell University, Laboratory for Elementary-Particle Physics; Newman Lab; Ithaca, NY 14853–5001, USA*

[36] *Czech Technical University in Prague, Brehova 7; 115 19 Praha 1, Czech Republic*

[37] *Dakota State University, Madison, SD 57042, USA*

[38] *University of Delhi, Department of Physics and Astrophysics, Delhi 110007, India*

[39] *Drexel University, Philadelphia, PA 19104, USA*

[40] *Duke University, Durham, NC 27706, USA*

[41] *University of Durham, Institute for Particle Physics Phenomenology; Dept. of Physics, Ogden Centre for Fund. Physics; South Road; Durham DH1 3LE, UK*

[42] *University Estadual de Feira de Santana, S/N;44036-900, Feira de Santana-BA, Brazil*

[43] *Fermi National Accelerator Lab, Batavia, IL 60510-0500, USA*

[44] *University Federal de Goias, Goiania, GO, Brazil*

[45] *Gran Sasso Science Institute, 7, L'Aquila, Italy*

[46] *Universidad de Guanajuato, Gto., C.P.37000, Mexico*

[47] *Harish-Chandra Research Institute, Jhunsi, Allahabad 211 019, India*

[48] *University of Hawaii, Honolulu, HI 96822-2219, USA*

[49] *University of Houston, Houston, TX 77204, USA*

[50] *Huddersfield, Huddersfield, West Yorkshire HD1 3DH, UK*

[51] *Horia Hulubei National Institute of Physiscs and Nuclear Engineering, Horia Hulubei National Institute of Physiscs and Nuclear Engineering, Bucharest-Magurele, Romania*

[52] *University of Hyderabad, Gachibowli, Hyderabad - 500 046, India*

[53] *Institut de Física d'Altes Energies (IFAE); Campus Universitat Autonoma de Barcelona , E-08193 Cerdanyola del Valles (Barcelona), Spain*

[54] *Illinois Institute of Technology , Room 182LS; Chicago, IL 60616, USA*

[55] *IIT Hyderabad, Kandi, Hyderabad - 502205, India*

[56] *Institute for Nuclear Research of the Russian Academy of Sciences (INR RAS), 60th October Anniversary Prosp. 7a Moscow, Russia 117312, Russia*

[57] *Institute for Research in Fundamental Sciences (IPM), Tehran, Iran. Postal code: 19538-33511 PO Box:*

3

19395-5531, Iran

[58]Idaho State University, Department of Physics 921 South 8th Ave. Stop 8106 Pocatello, ID 83209-8106, USA

[59]Imperial College of Science Tech. & Medicine, Blackett Lab.; Prince Consort Road; London SW7 2BZ, UK

[60]Indian Institute of Technology Guwahati, Guwahati, 781 039, India

[61]Indiana University, Bloomington, IN 47405-7105, USA

[62]Iowa State University, Ames, IA 50011, USA

[63]Institut de Physique Nucleaire de Lyon (IPNL), Rue E. Fermi 4 69622 Villeurbanne, France

[64]University of Jammu, Physics Department, JAMMU-180006, India

[65]Kansas State University, Manhattan, KS 66506, USA

[66]Kavli IPMU, University of Tokyo, Kashiwa Shi, Chiba 277-8568, Japan

[67]KEK, High Energy Accelerator Research Organization 1–1 Oho, Tsukuba-shi; Ibaraki-ken 305-0801, Japan

[68]KYIV National University, Department of Nuclear Physics, 64, 01601 Kyiv, Ukraine

[69]Koneru Lakshmaiah, India

[70]Krakow, Golebia 24, 31-007 Kraków, Poland

[71]Lab. d'Annecy-le-Vieux de Phys. des Particules, BP 110; F-74941 Annecy-le-Vieux CEDEX, France

[72]Laboratori Nazionali del Gran Sasso, I-67010 Assergi, AQ, Italy

[73]Lancaster University, Bailrigg, Lancaster LA1 4YB, UK

[74]Lawrence Berkeley National Lab., Berkeley, CA 94720-8153, USA

[75]Université de Liège, Bat B5, Sart Tilman B-4000, Belgium

[76]University of Liverpool, L69 7ZE, Liverpool, UK

[77]University College London, London, WC1E 6BT, UK

[78]Los Alamos National Laboratory, Los Alamos, NM 87545, USA

[79]Louisiana State University, Baton Rouge, LA 70803-4001, USA

[80]University of Lucknow, Department of Physics Lucknow 226007 Uttar Pradesh, India

[81]University of Manchester, Oxford Road, Manchester M13 9PL, UK

[82]University of Maryland, College Park, MD 20742-4111, USA

[83]Massachusetts Institute of Technology, Cambridge, MA 02139-4307, USA

[84]Max Planck MPP, Max-Planck-Institut fuer Physik (Werner-Heisenberg-Institut) Foehringer Ring 6 80805 Muenchen, Germany

[85]University of Puerto Rico, Box 9016; Mayaguez, PR 00681-9000, USA

[86]University of Michigan, 450 Church Street Ann Arbor, Michigan 48109-1040, USA

[87]Michigan State University, East Lansing, MI 48824, USA

[88]University di Milano, INFN Sezione di Milano, I-20133 Milano, Italy

[89]INFN Sezione di Milano Bicocca, Piazza della Scienza 3, 20126 Milano, Italy

[90]University of Minnesota (Twin Cities), Minneapolis, MN 55455, USA

[91]University of Minnesota (Duluth), Duluth, MN 55812, USA

[92]NIKHEF, Science Park, Amsterdam, Netherlands

[93]Istituto Nazionale di Fisica Nucleare - Sezione di Napoli, Complesso Universitario di Monte S. Angelo, I-80126 Napoli, Italy

[94]National Centre for Nuclear Research, A. Soltana 7, 05 400 Otwock, Poland

[95]Jawaharlal Nehru University, New Delhi 110067, INDIA, India

[96]University of New Mexico, MSC07 4220; Albuquerque, NM 87131, USA

[97]Northwestern University, Evanston, Il 60208, USA

[98]University of Notre Dame, Notre Dame, IN 46556-5670, USA

[99]Observatorio Nacional, R. Lourival Bpo., 89 - Madruga, Vassouras - RJ, 27700-000, Brazil

[100]Ohio State University, Dept. of Physics; 191 W. Woodruff Ave.; Columbus, OH 43210, USA

[101]Oregon State University, Dept. of Physics; 301 Weniger Hall; Corvallis, OR 97331–6507, USA

[102]University of Oxford, Oxford, OX1 3RH, UK

[103]Pacific Northwest National Lab, , USA

[104]Pennsylvania State University, PMB 264; University Park, PA 16802-6300, USA

[105]PUCP, Av. Universitaria 1801, Lima, Peru

[106]University of Padova, Dip. Fisica e Astronomia G. Galilei and INFN Sezione di Padova, I-35131 Padova, Italy

[107]Panjab University, Chandigarh, 160014 U.T., India

[108]University of Pavia, INFN Sezione di Pavia, I-27100 Pavia, Italy

[109]University of Pennsylvania, Philadelphia, PA 19104-6396, USA

[110]University di Pisa, Theor. Division; Largo B. Pontecorvo 3, Ed. B-C; I-56127 Pisa, Italy

[111]University of Pittsburgh, Pittsburgh, PA 15260, USA

[112]Princeton University, Princeton, New Jersey 08544-0708, USA

[113]Punjab Agri. University, Centre for High Energy Physics; Lahore - 54590, India

4

[114] *University of Rochester, Rochester, NY 14627-0171, USA*

[115] *SLAC National Acceleratory Laboratory, Menlo Park, CA 94025, USA*

[116] *STFC Rutherford Appleton Laboratory, Harwell Oxford, Didcot OX11 0QX, UK*

[117] *CEA/Saclay, IPhT; Inst. de Physique Theorique; Orme des Merisiers, Point Courrier 136; F-91191 Gif-sur-Yvette CEDE, France*

[118] *University of Sheffield, Sheffield, S3 7RH, UK*

[119] *University of Sofia, Atomic Physics Dept., Faculty of Physics; 5 James Bourchier Blvd.; BG-1164 Sofia, Bulgaria*

[120] *University of South Carolina, Columbia, SC 29208, USA*

[121] *University of South Dakota, Vermillion, SD 57069, USA*

[122] *South Dakota School of Mines and Technology, Rapid City, SD 57701, USA*

[123] *South Dakota Science And Technology Authority, Lead, SD 57754, USA*

[124] *South Dakota State University, Brookings, SD 57007, USA*

[125] *Southern Methodist University, Dallas, TX 75275, USA*

[126] *Stanford University, Varian Physics Bldg.; 382 Via Pueblo Mall; Stanford, CA 94305–4060, USA*

[127] *Stony Brook University, Nucleon Decay and Neutrino Physics Group Department of Physics and Astronomy Stony Brook University Stony Brook, NY 11794-3800, USA*

[128] *University of Sussex, Brighton, BN1 9RH, UK*

[129] *Syracuse University, Syracuse, NY 13244-1130, USA*

[130] *University of Tennessee at Knoxville, Knoxville, TN, USA*

[131] *University of Texas (Arlington), Arlington, TX 76019, USA*

[132] *University of Texas (Austin), Austin, TX 78712-0264, USA*

[133] *TUBITAK Space Technologies Research Institute , TR-06800, Ankara, Turkey*

[134] *Tufts University, Medford, MA 02155, USA*

[135] *Variable Energy Cyclotron Centr, 1/AF, Bidhannagar Kolkata - 700 064 West Bengal, India*

[136] *Instituto de Fisica Corpuscular, C/Catedratico Jose Beltran, 2 E-46980 Paterna (Valencia), Spain*

[137] *Virginia Tech., Blacksburg, VA 24061-0435, USA*

[138] *University of Warsaw, Faculty of Physics ul. Pasteura 5 02-093 Warsaw, Poland*

[139] *University of Warwick, Coventry CV4 7AL, UK*

[140] *Wichita State University, Physics Division 1845 Fairmount St. Wichita, KS 67260-0032, USA*

[141] *College of William and Mary, Williamsburg, VA 23187-8795, USA*

[142] *University of Wisconsin, Madison, WI 53706, USA*

[143] *Wroclaw University, Plac Maxa Borna 9, 50-204 Wroclaw, Poland*

[144] *Yale University, New Haven, CT 06520, USA*

[145] *Yerevan Institute for Theoretical Physics and Modeling, Halabian Str. 34; Yerevan 0036, Armenia*

[146] *York, Physics and Astronomy Dept.; 4700 Keele St.; Toronto M3J 1P3, Canada*

[147] *ETH Zurich, HPK F 23 Schafmattstr. 20 8093 Zürich, Switzerland*

2015-11-25

Contents

List of Figures

List of Tables

Acronyms, Abbreviations and Terms

$\mathcal{O}(n)$ of order n

$M_\odot$ solar mass

3D   3 dimensional (also 1D, 2D, etc.)

$\mathrm{kt \cdot MW \cdot year}$ exposure, expressed in kilotonnes $\times$ megawatts $\times$ years, based on 56% beam uptime and efficiency

$\mathrm{kt \cdot year}$ exposure (without beam), expressed in kilotonnes times years

BR   branching ratio

C.L.   confidence level

CC   charged current (interaction)

CDR   Conceptual Design Report

CF   Conventional Facilities

CKM   (CKM matrix) Cabibbo-Kobayashi-Maskawa matrix, also known as quark mixing matrix

CP   product of charge and parity transformations

CPT   product of charge, parity and time-reversal transformations

CPV   violation of charge and parity symmetry

DAQ   data acquisition

DIS   deep inelastic scattering

DM   dark matter

DOE	U.S. Department of Energy
DSNB	Diffuse Supernova Neutrino Background
DUNE	Deep Underground Neutrino Experiment
ESH	Environment, Safety and Health
eV	electron volt, unit of energy (also keV, MeV, GeV, etc.)
FD	far detector
FGT	Fine-Grained Tracker
FSCF	far site conventional facilities
FSI	final-state interactions
GEANT4	GEometry ANd Tracking, a platform for the simulation of the passage of particles through matter using Monte Carlo methods
GENIE	Generates Events for Neutrino Interaction Experiments (an object-oriented neutrino Monte Carlo generator)
GLoBES	General Long-Baseline Experiment Simulator (software package)
GUT	grand unified theory
L	level, indicates depth in feet underground at the far site, e.g., 4850L
L/E	length-to-energy ratio
LAr	liquid argon
LArTPC	liquid argon time-projection chamber
LBL	long-baseline (physics)
LBNF	Long-Baseline Neutrino Facility
LRI	long-range interactions
MC	Monte Carlo (detector simulation methods)
MH	mass hierarchy
MI	Main Injector (at Fermilab)

MSW	Mikheyev-Smirnov-Wolfenstein (effect)
NC	neutral current (interaction)
ND	near neutrino detector
NDS	Near Detector Systems; refers to the collection of detector systems at the near site
near detector	except in Volume 4 Chapter 7, *near detector* refers to the *neutrino* detector system in the NDS
NH	normal (mass) hierarchy
NSCF	near site conventional facilities
NSI	nonstandard interactions
octant	any of the eight parts into which 4π is divided by three mutually perpendicular axes; the range of the PMNS angles is 0 to $\pi/2$, which spans only two of the eight octants
PMNS	(PMNS matrix) Pontecorvo-Maki-Nakagawa-Sakata matrix, also known as the lepton or neutrino mixing matrix
POT	protons on target
QA	quality assurance
QE	quasi-elastic (interaction)
SM	Standard Model of particle physics
SME	Standard-Model Extension
SUSY	supersymmetry
t	metric ton, written *tonne* (also kt)
tonne	metric ton
TPC	time-projection chamber (not used as 'total project cost' in the CDR)
WIMP	weakly-interacting massive particle

Chapter 1

Introduction to LBNF and DUNE

1.1   An International Physics Program

The global neutrino physics community is developing a multi-decade physics program to measure unknown parameters of the Standard Model of particle physics and search for new phenomena. The program will be carried out as an international, leading-edge, dual-site experiment for neutrino science and proton decay studies, which is known as the Deep Underground Neutrino Experiment (DUNE). The detectors for this experiment will be designed, built, commissioned and operated by the international DUNE Collaboration. The facility required to support this experiment, the Long-Baseline Neutrino Facility (LBNF), is hosted by Fermilab and its design and construction is organized as a DOE/Fermilab project incorporating international partners. Together LBNF and DUNE will comprise the world's highest-intensity neutrino beam at Fermilab, in Batavia, IL, a high-precision near detector on the Fermilab site, a massive liquid argon time-projection chamber (LArTPC) far detector installed deep underground at the Sanford Underground Research Facility (SURF) 1300 km away in Lead, SD, and all of the conventional and technical facilities necessary to support the beamline and detector systems.

The strategy for executing the experimental program presented in this Conceptual Design Report (CDR) has been developed to meet the requirements set out in the P5 report [1] and takes into account the recommendations of the European Strategy for Particle Physics [2]. It adopts a model where U.S. and international funding agencies share costs on the DUNE detectors, and CERN and other participants provide in-kind contributions to the supporting infrastructure of LBNF. LBNF and DUNE will be tightly coordinated as DUNE collaborators design the detectors and infrastructure that will carry out the scientific program.

The scope of LBNF is

- an intense neutrino beam aimed at the far site

- conventional facilities at both the near and far sites

- cryogenics infrastructure to support the DUNE detector at the far site

The DUNE detectors include

- a high-performance neutrino detector and beamline measurement system located a few hundred meters downstream of the neutrino source

- a massive liquid argon time-projection chamber (LArTPC) neutrino detector located deep underground at the far site

With the facilities provided by LBNF and the detectors provided by DUNE, the DUNE Collaboration proposes to mount a focused attack on the puzzle of neutrinos with broad sensitivity to neutrino oscillation parameters in a single experiment. The focus of the scientific program is the determination of the neutrino mass hierarchy and the explicit demonstration of leptonic CP violation, if it exists, by precisely measuring differences between the oscillations of muon-type neutrinos and antineutrinos into electron-type neutrinos and antineutrinos, respectively. Siting the far detector deep underground will provide exciting additional research opportunities in nucleon decay, studies utilizing atmospheric neutrinos, and neutrino astrophysics, including measurements of neutrinos from a core-collapse supernova should such an event occur in our galaxy during the experiment's lifetime.

1.2   The LBNF/DUNE Conceptual Design Report Volumes

1.2.1   A Roadmap of the CDR

The LBNF/DUNE CDR describes the proposed physics program and technical designs at the conceptual design stage. At this stage, the design is still undergoing development and the CDR therefore presents a *reference design* for each element as well as *alternative designs* that are under consideration.

The CDR is composed of four volumes and is supplemented by several annexes that provide details on the physics program and technical designs. The volumes are as follows

- Volume 1: *The LBNF and DUNE Projects* provides an executive summary of and strategy for the experimental program and introduces the CDR.

- Volume 2: *The Physics Program for DUNE at LBNF* outlines the scientific objectives and describes the physics studies that the DUNE Collaboration will undertake to address them.

- Volume 3: *The Long-Baseline Neutrino Facility for DUNE* describes the LBNF Project, which includes design and construction of the beamline at Fermilab, the conventional facilities at both Fermilab and SURF, and the cryostat and cryogenics infrastructure required for the DUNE far detector.

- Volume 4: *The DUNE Detectors at LBNF* describes the DUNE Project, which includes the design, construction and commissioning of the near and far detectors.

More detailed information for each of these volumes is provided in a set of annexes listed on the *CD-1-R Reports and Documents* page.

1.2.2   About this Volume

Volume 2: *The Physics Program for DUNE at LBNF* outlines the science objectives in Chapter 2, describes each of the areas of study in the following chapters, and concludes with a summary.

The LBNF/DUNE science objectives are categorized as primary, ancillary and additional, with the primary objectives driving the experiment and facility designs that together will also enable pursuit of the ancillary objectives. Pursuit of the additional goals may require technological developments beyond the current designs.

Chapters 3, 4 and 5 describe the physics program for the DUNE far detector in the areas of long-baseline neutrino oscillations, nucleon decay, atmospheric neutrinos and detection of supernova neutrino bursts and low-energy neutrinos; they also discuss the requirements that these studies impose on the detector design.

Chapter 6 discusses the role that the near detector plays in the overall DUNE physics program and the requirements that it must satisfy, and describes the measurements and new physics searches that the near detector will enable on its own.

Chapter 2

LBNF/DUNE Scientific Goals

2.1   Overview of Goals

LBNF/DUNE will address fundamental questions key to our understanding of the Universe. These include

- **What is the origin of the matter-antimatter asymmetry in the Universe?** Immediately after the Big Bang, matter and antimatter were created equally, but now matter dominates. By studying the properties of neutrino and antineutrino oscillations to determine if charge-parity (CP) symmetry is violated in the lepton sector, LBNF/DUNE will pursue the current most promising avenue for understanding this asymmetry.

- **What are the fundamental underlying symmetries of the Universe?** The patterns of mixings and masses between the particles of the Standard Model are not understood. By making precise measurements of the mixing between the neutrinos and the ordering of neutrino masses and comparing these with the quark sector, LBNF/DUNE could reveal new underlying symmetries of the Universe.

- **Is there a Grand Unified Theory of the Universe?** Results from a range of experiments suggest that the physical forces observed today were unified into one force at the birth of the Universe. Grand Unified Theories (GUTs), which attempt to describe the unification of forces, predict that protons should decay, a process that has never been observed. DUNE will search for proton decay in the range of proton lifetimes predicted by a wide range of GUT models.

- **How do supernovae explode and what new physics will we learn from a neutrino burst?** Many of the heavy elements that are the key components of life were created in the super-hot cores of collapsing stars. DUNE would be able to detect the neutrino bursts from core-collapse supernova within our galaxy (should any occur). Measurements of the time, flavor and energy structure of the neutrino burst will be critical for understanding the dynamics of this important astrophysical phenomenon, as well as providing information on neutrino

properties and other particle physics.

The LBNF/DUNE scientific objectives are categorized into: the *primary science program*, addressing the key science questions highlighted by the particle physics project prioritization panel (P5); a high-priority *ancillary science program* that is enabled by the construction of LBNF and DUNE; and *additional scientific objectives*, that may require developments of the LArTPC technology. The goals of the primary science program define the high-level requirements for LBNF and the DUNE detectors. The ancillary science program provides further requirements, specifically on the design of the near detector, required for the full scientific exploitation of this world leading facility.

2.2   The Primary Science Program

The primary science program of the LBNF/DUNE experiment focuses on fundamental open questions in neutrino and astroparticle physics:

- precision measurements of the parameters that govern $\nu_\mu \to \nu_e$ and $\overline{\nu}_\mu \to \overline{\nu}_e$ oscillations with the goal of

  – measuring the charge-parity (CP) violating phase δ_{CP} — where a value differing from zero or π would represent the discovery of CP-violation in the leptonic sector, providing a possible explanation for the matter-antimatter asymmetry in the universe;

  – determining the neutrino mass ordering (the sign of $\Delta m^2_{31} \equiv m^2_3 - m^2_1$), often referred to as the neutrino *mass hierarchy*;

  – precision tests of the three-flavor neutrino oscillation paradigm through studies of muon neutrino disappearance and electron neutrino appearance in both ν_μ and $\overline{\nu}_\mu$ beams, including the measurement of the mixing angle θ_{23} and the determination of the octant in which this angle lies;

- search for proton decay in several important decay modes, for example $p \to K^+\overline{\nu}$, where the observation of proton decay would represent a ground-breaking discovery in physics, providing a portal to Grand Unification of the forces;

- detection and measurement of the ν_e flux from a core-collapse supernova within our galaxy, should any occur during the lifetime of the DUNE experiment.

2.3   The Ancillary Science Program

The intense neutrino beam from LBNF, the massive DUNE LArTPC far detector and the highly capable DUNE near detector provide a rich ancillary science program, beyond the primary mission of the experiment. The ancillary science program includes:

- other accelerator-based neutrino flavor transition measurements with sensitivity to Beyond Standard Model (BSM) physics, such as:

  - non-standard interactions (NSIs);

  - the search for sterile neutrinos at both the near and far sites;

  - measurements of tau neutrino appearance;

- measurements of neutrino oscillation phenomena using atmospheric neutrinos;

- a rich neutrino interaction physics program utilizing the DUNE near detector, including:

  - a wide-range of measurements of neutrino cross sections;

  - studies of nuclear effects, including neutrino final-state interactions;

  - measurements of the structure of nucleons;

  - measurement of $\sin^2 \theta_{\mathrm{W}}$;

- and the search for signatures of dark matter.

Furthermore, a number of previous breakthroughs in particle physics have been serendipitous, in the sense that they were beyond the original scientific objectives of their experiments. The intense LBNF neutrino beam and novel capabilities for both the DUNE near and far detectors will probe new regions of parameter space for both the accelerator-based and astrophysical frontiers, providing the opportunity for discoveries that are not currently anticipated.

2.4 Additional Scientific Objectives

There are a number of opportunities that could be enabled by developments/improvements to the LArTPC detector technology over the course of the DUNE installation. These include:

- measurements of neutrino oscillation phenomena and of solar physics using solar neutrinos;

- detection and measurement of the diffuse supernova neutrino flux;

- measurement of neutrinos from astrophysical sources at energies from gamma-ray bursts, active galactic nuclei, black-hole and neutron-star mergers, or other transient sources.

Chapter 3

Long-Baseline Neutrino Oscillation Physics

3.1 Overview and Theoretical Context

The Standard Model of particle physics presents a remarkably accurate description of the elementary particles and their interactions. However, its limitations pose deeper questions about Nature. With the discovery of the Higgs boson at CERN, the Standard Model would be "complete" except for the discovery of neutrino mixing, which indicated neutrinos had a very small but nonzero mass. In the Standard Model, the simple Higgs mechanism is responsible for both quark and charged lepton masses, quark mixing and charge-parity (CP) violation. However, the small size of neutrino masses and their relatively large mixing bears little resemblance to quark masses and mixing, suggesting that different physics – and possibly different mass scales – in the two sectors may be present, thus motivating precision study of mixing and CP violation in the lepton sector of the Standard Model.

DUNE plans to pursue a detailed study of neutrino mixing, resolve the neutrino mass ordering, and search for CP violation in the lepton sector by studying the oscillation patterns of high-intensity ν_μ and $\bar{\nu}_\mu$ beams measured over a long baseline. Neutrino oscillation arises from mixing between the flavor ν_e, ν_μ, ν_τ and mass (ν_1, ν_2, ν_3) eigenstates of neutrinos. In direct correspondence with mixing in the quark sector, the transformations between basis states is expressed in the form of a complex unitary matrix, known as the *PMNS mixing matrix*:

$$\begin{pmatrix} \nu_e \\ \nu_\mu \\ \nu_\tau \end{pmatrix} = \underbrace{\begin{pmatrix} U_{e1} & U_{e2} & U_{e3} \\ U_{\mu1} & U_{\mu2} & U_{\mu3} \\ U_{\tau1} & U_{\tau2} & U_{\tau3} \end{pmatrix}}_{U_{\mathrm{PMNS}}} \begin{pmatrix} \nu_1 \\ \nu_2 \\ \nu_3 \end{pmatrix}. \tag{3.1}$$

The PMNS matrix in full generality depends on just three mixing angles and a CP-violating phase[1]. The mixing angles and phase are designated as (θ_{12}, θ_{23}, θ_{13}) and δ_{CP}. This matrix can be parameterized as the product of three two-flavor mixing matrices as follows [3], where $c_{\alpha\beta} = \cos\theta_{\alpha\beta}$

---

[1]There are two additional CP phases (Majorana phases), but they are unobservable in the oscillation processes.

and $s_{\alpha\beta} = \sin\theta_{\alpha\beta}$:

$$U_{\text{PMNS}} = \underbrace{\begin{pmatrix} 1 & 0 & 0 \\ 0 & c_{23} & s_{23} \\ 0 & -s_{23} & c_{23} \end{pmatrix}}_{\text{I}} \underbrace{\begin{pmatrix} c_{13} & 0 & e^{-i\delta_{\text{CP}}}s_{13} \\ 0 & 1 & 0 \\ -e^{i\delta_{\text{CP}}}s_{13} & 0 & c_{13} \end{pmatrix}}_{\text{II}} \underbrace{\begin{pmatrix} c_{12} & s_{12} & 0 \\ -s_{12} & c_{12} & 0 \\ 0 & 0 & 1 \end{pmatrix}}_{\text{III}} \tag{3.2}$$

The parameters of the PMNS matrix determine the probability amplitudes of the neutrino oscillation phenomena that arise from mixing. The frequency of neutrino oscillation depends on the difference in the squares of the neutrino masses, $\Delta m_{ij}^2 \equiv m_i^2 - m_j^2$; a set of three neutrino mass states implies two independent mass-squared differences (the "solar" mass splitting, Δm_{21}^2, and the "atmospheric" mass splitting, Δm_{31}^2), where $\Delta m_{31}^2 = \Delta m_{32}^2 + \Delta m_{21}^2$. The ordering of the mass states is known as the *neutrino mass hierarchy*. An ordering of $m_1 < m_2 < m_3$ is known as the *normal hierarchy* since it matches the mass ordering of the charged leptons in the Standard Model, whereas an ordering of $m_3 < m_1 < m_2$ is referred to as the *inverted hierarchy*.

The entire complement of neutrino experiments to date has measured five of the mixing parameters [4, 5, 6]: the three angles θ_{12}, θ_{23} and (recently) θ_{13}, and the two mass differences Δm_{21}^2 and Δm_{31}^2. The sign of Δm_{21}^2 is known, but not that of Δm_{31}^2, which is the crux of the mass hierarchy ambiguity. The values of θ_{12} and θ_{23} are large, while θ_{13} is smaller. The value of δ_{CP} is unknown. The absolute values of the entries of the PMNS matrix, which contains information on the strength of flavor-changing weak decays in the lepton sector, can be expressed in approximate form as

$$|U_{\text{PMNS}}| \sim \begin{pmatrix} 0.8 & 0.5 & 0.1 \\ 0.5 & 0.6 & 0.7 \\ 0.3 & 0.6 & 0.7 \end{pmatrix}. \tag{3.3}$$

using values for the mixing angles given in Table 3.4. The three-flavor-mixing scenario for neutrinos is now well established. However, the mixing parameters are not known to the same precision as are those in the corresponding quark sector, and several important quantities, including the value of δ_{CP} and the sign of the large mass splitting, are still undetermined.

The relationships between the values of the parameters in the neutrino and quark sectors suggest that mixing in the two sectors is qualitatively different. Illustrating this difference, the value of the entries of the CKM quark-mixing matrix (analogous to the PMNS matrix for neutrinos, and thus indicative of the strength of flavor-changing weak decays in the quark sector) can be expressed in approximate form as

$$|V_{\text{CKM}}| \sim \begin{pmatrix} 1 & 0.2 & 0.004 \\ 0.2 & 1 & 0.04 \\ 0.008 & 0.04 & 1 \end{pmatrix}. \tag{3.4}$$

for comparison to the entries of the PMNS matrix given in Equation 3.3. As discussed in [7], the question of why the quark mixing angles are smaller than the lepton mixing angles is an important part of the flavor pattern question.

To quote the discussion in [8], "while the CKM matrix is almost proportional to the identity matrix plus hierarchically ordered off-diagonal elements, the PMNS matrix is far from diagonal and, with the possible exception of the U_{e3} element, all elements are $\mathcal{O}(1)$." It is important here to note that

the smaller of the lepton mixing angles is of similar magnitude to the larger of the quark mixing parameters, namely the Cabibbo angle [9]. One theoretical method often used to address this question involves the use of non-Abelian discrete subgroups of $SU(3)$ as flavor symmetries; the popularity of this method is due in part from the fact that these symmetries can give rise to the nearly *tri-bi-maximal*[2] structure of the PMNS matrix. Whether employing these flavor symmetries or other methods, any theoretical principle that attempts to describe the fundamental symmetries implied by the observed organization of quark and neutrino mixing — such as those proposed in unification models — leads to testable predictions such as sum rules between CKM and PMNS parameters [7, 8, 11, 12]. Data on the patterns of neutrino mixing are already proving crucial in the quest for a relationship between quarks and leptons and their seemingly arbitrary generation structure.

Clearly much work remains in order to complete the standard three-flavor mixing picture, particularly with regard to θ_{23} (is it less than, greater than, or equal to 45°?), mass hierarchy (normal or inverted?) and δ_{CP}. Additionally, there is great value in obtaining a set of measurements for multiple parameters *from a single experiment*, so that correlations and systematic uncertainties can be handled properly. Such an experiment would also be well positioned to extensively test the standard picture of three-flavor mixing. DUNE is designed to be this experiment.

3.2 Expected Event Rate and Sensitivity Calculations

The oscillation probability of $\nu_\mu \to \nu_e$ through matter in a constant density approximation is, to first order [13]:

$$
\begin{aligned}
P(\nu_\mu \to \nu_e) \;\simeq\; & \sin^2\theta_{23}\sin^2 2\theta_{13}\frac{\sin^2(\Delta_{31}-aL)}{(\Delta_{31}-aL)^2}\Delta_{31}^2 \\
& + \sin 2\theta_{23}\sin 2\theta_{13}\sin 2\theta_{12}\frac{\sin(\Delta_{31}-aL)}{(\Delta_{31}-aL)}\Delta_{31}\frac{\sin(aL)}{(aL)}\Delta_{21}\cos(\Delta_{31}+\delta_{\mathrm{CP}}) \\
& + \cos^2\theta_{23}\sin^2 2\theta_{12}\frac{\sin^2(aL)}{(aL)^2}\Delta_{21}^2,
\end{aligned}
\tag{3.5}
$$

where $\Delta_{ij} = \Delta m_{ij}^2 L/4E_\nu$, $a = G_F N_e/\sqrt{2}$, G_F is the Fermi constant, N_e is the number density of electrons in the Earth, L is the baseline in km, and E_ν is the neutrino energy in GeV. In the equation above, both δ_{CP} and a switch signs in going from the $\nu_\mu \to \nu_e$ to the $\bar{\nu}_\mu \to \bar{\nu}_e$ channel; i.e., a neutrino-antineutrino asymmetry is introduced both by CP violation (δ_{CP}) and the matter effect (a). The origin of the matter effect asymmetry is simply the presence of electrons and absence of positrons in the Earth. In the few-GeV energy range, the asymmetry from the matter effect increases with baseline as the neutrinos pass through more matter, therefore an experiment with a longer baseline will be more sensitive to the neutrino mass hierarchy. For baselines longer than $\sim$1200 km, the degeneracy between the asymmetries from matter and CP-violation effects can be

---

[2]Tri-bi-maximal mixing refers to a form of the neutrino mixing matrix with effective bimaximal mixing of ν_μ and ν_τ at the atmospheric scale ($L/E \sim 500\,\mathrm{km}/\,\mathrm{GeV}$) and effective trimaximal mixing for ν_e with ν_μ and ν_τ at the solar scale ($L/E \sim 15{,}000\,\mathrm{km}/\,\mathrm{GeV}$) [10].

resolved [14]; hence DUNE, with a baseline of $\sim$1300 km, will be able to unambiguously determine the neutrino mass hierarchy *and* measure the value of δ_{CP} [15].

The electron neutrino appearance probability, $P(\nu_\mu \to \nu_e)$, is shown in Figure 3.1 at a baseline of 1300 km as a function of neutrino energy for several values of δ_{CP}. As this figure illustrates, the value of δ_{CP} affects both the amplitude and frequency of the oscillation. The difference in probability amplitude for different values of δ_{CP} is larger at higher oscillation nodes, which correspond to energies less than 1.5 GeV. Therefore, a broadband experiment, capable of measuring not only the rate of ν_e appearance but of mapping out the spectrum of observed oscillations down to energies of at least 500 MeV, is desirable [16]. Since there are terms proportional to $\sin \delta_{CP}$ in Equation 3.6, changes to the value of δ_{CP} induce opposite changes to ν_e and $\bar{\nu}_e$ appearance probabilities, so a beam that is capable of operating in neutrino mode (forward horn current) and antineutrino mode (reverse horn current) is also a critical component of the experiment.
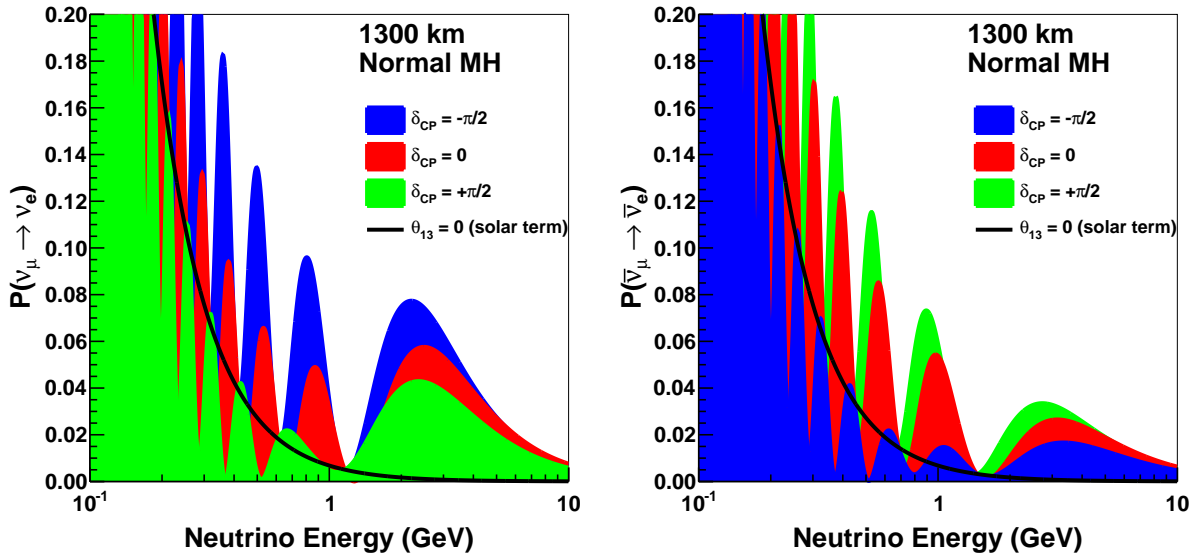
Figure 3.1: The appearance probability at a baseline of 1300 km, as a function of neutrino energy, for $\delta_{CP} = -\pi/2$ (blue), 0 (red), and $\pi/2$ (green), for neutrinos (left) and antineutrinos (right), for normal hierarchy. The black line indicates the oscillation probability if θ_{13} were equal to zero.

The experimental sensitivities presented here are estimated using GLoBES[17, 18]. GLoBES takes neutrino beam fluxes, cross sections, and detector-response parameterization as inputs. This document presents a range of possible physics sensitivities depending on the design of the neutrino beam, including the proton beam energy and power used. The beam power as a function of proton beam energy from the PIP-II upgrades and the number of protons-on-target per year assumed in the sensitivities are shown in Table 3.1. These numbers assume a combined uptime and efficiency of the FNAL accelerator complex and the LBNF beamline of 56%.

A conservative estimate of sensitivity is calculated using neutrino fluxes produced from a detailed GEANT4 beamline simulation that is based on the reference design of the beamline as presented in Volume 3: *The Long-Baseline Neutrino Facility for DUNE.* Neutrino fluxes from a simulation based on an optimized beam design are used to show the goal sensitivity. There is a range of design options that produce sensitivities in between the sensitivity of the reference beam design and the optimized

Table 3.1: Expected POT per year at various primary proton beam momenta.

Proton Momentum (GeV/c)	Expected Beam Power (MW)	Expected POT/year
120	1.2	1.1×10^{21}
80	1.07	1.47×10^{21}
60	1.03	1.89×10^{21}

beam design, and further optimization is possible. The actual flux will depend upon details of the hadron production and focusing design; optimization of the beam design to maximize experimental sensitivity is a critical aspect of the experiment design. Table 3.2 summarizes the key properties of the GEANT4 beamline simulations used to produce fluxes for the sensitivity studies. The main differences between the two beam designs are the target geometry, horn current, horn design and decay pipe length; the choice of horn design has the biggest effect on the sensitivity. Section 3.7 describes the beamline simulations in more detail and explores the potential improvements that could be achieved by variations in the reference beam design.

Table 3.2: A comparison of the beamline parameters assumed for the CDR Reference Design flux and the Optimized Design flux used in the sensitivity calculations presented in this chapter. Section 3.9.1 provides the details.

Parameter	CDR Reference Design	Optimized Design
Proton Beam Energy	80 GeV	80 GeV
Proton Beam Power	1.07 MW	1.07 MW
Target	Graphite	Graphite
Horn Current	230 kA	297 kA
Horn Design	NuMI-style	Genetic Optimization
Decay Pipe Length	204 m	241 m
Decay Pipe Diameter	4 m	4 m

The signal for ν_e appearance is an excess of charged-current (CC) ν_e and $\bar{\nu}_e$ interactions over the expected background in the far detector. The background to ν_e appearance is composed of: (1) CC interactions of ν_e and $\bar{\nu}_e$ intrinsic to the beam; (2) misidentified ν_μ and $\bar{\nu}_\mu$ CC events; (3) neutral current (NC) backgrounds and (4) ν_τ and $\bar{\nu}_\tau$ CC events in which the τ's decay leptonically into electrons/positrons. NC and ν_τ backgrounds are due to interactions of higher-energy neutrinos but they contribute to backgrounds mainly at low energy, which is important for the sensitivity to CP violation.

The LArTPC performance parameters that go into the GLoBES calculation are generated using the DUNE Fast Monte Carlo (MC) simulation, which is described in detail in [19]. The Fast MC combines the simulated flux, the GENIE neutrino interaction generator [20], and a parameterized detector response that is used to simulate the reconstructed energy and momentum of each final-state particle. The detector response parameters used to determine the reconstructed quantities[3] are summarized in Table 3.3. The simulated energy deposition of the particles in each interaction is

---

[3]The assumptions on detector response used in the Fast MC are preliminary, and are expected to improve as the full detector simulation advances and more information on the performance of LArTPC detectors becomes available.

then used to calculate reconstructed kinematic quantities (e.g., the neutrino energy). Event sample classifications (ν_e CC-like, ν_μ CC-like, or NC-like), including mis-ID rates, are determined by the identification of lepton candidates. Lepton candidates are selected based on a variety of criteria including particle kinematics, detector thresholds, and probabilistic estimates of particle fates. To reduce the NC and ν_τ CC backgrounds in the ν_e CC-like sample, an additional discriminant is formed using reconstructed transverse momentum along with reconstructed neutrino and hadronic energy as inputs to a k-Nearest-Neighbor (kNN) machine-learning algorithm. Figures 3.2 and 3.3 show the true-to-reconstructed energy smearing matrices extracted from the Fast MC and used as inputs to GLoBES. Figure 3.4 shows the analysis sample detection × selection efficiencies for the various signal and background modes used by GLoBES, also extracted from the Fast MC.

Table 3.3: Summary of the single-particle far detector response used in the Fast MC. For some particles, the response depends upon behavior or momentum, as noted in the table. If a muon or a pion that is mis-identified as a muon is contained within the detector, the momentum is smeared based on track length. Exiting particles are smeared based on the contained energy. For neutrons with momentum < 1 GeV/c, there is a 10% probability that the particle will escape detection, so the reconstructed energy is set to zero. For neutrons that are detected, the reconstructed energy is taken to be 60% of the deposited energy after smearing.

Particle type	Detection Threshold (KE)	Energy/Momentum Resolution	Angular Resolution
$\mu^\pm$	30 MeV	Contained track: track length Exiting track: 30%	1°
$\pi^\pm$	100 MeV	μ-like contained track: track length π-like contained track: 5% Showering or exiting: 30%	1°
$e^\pm/\gamma$	30 MeV	$2\% \oplus 15\%/\sqrt{E}$[GeV]	1°
p	50 MeV	p<400 MeV/c: 10% p>400 MeV/c: $5\% \oplus 30\%/\sqrt{E}$[GeV]	5°
n	50 MeV	$40\%/\sqrt{E}$[GeV]	5°
other	50 MeV	$5\% \oplus 30\%/\sqrt{E}$[GeV]	5°

The cross section inputs to GLoBES have been generated using GENIE 2.8.4 [20]. The neutrino oscillation parameters and the uncertainty on those parameters are taken from the Nu-Fit [4] global fit to neutrino data; the values are given in Table 3.4. (See also [5] and [6] for other recent global fits.) Most of the sensitivities in this chapter are shown assuming normal hierarchy; this is an arbitrary choice for simplicity of presentation.

Figures 3.5 and 3.6 show the expected event rate for ν_e appearance and ν_μ disappearance, respectively, including expected flux, cross section, and oscillation probabilities as a function of neutrino energy at a baseline of 1300 km. The spectra are shown for a 150 kt · MW · year exposure each for neutrino and antineutrino beam mode, for a total 300 kt · MW · year exposure. The optimized beam design results in an increased signal rate in the lower-energy region. Tables 3.5 and 3.6 give the integrated rate for the ν_e appearance and ν_μ disappearance spectra, respectively. The spectra and rates are shown for both the reference beam design and the optimized beam design.
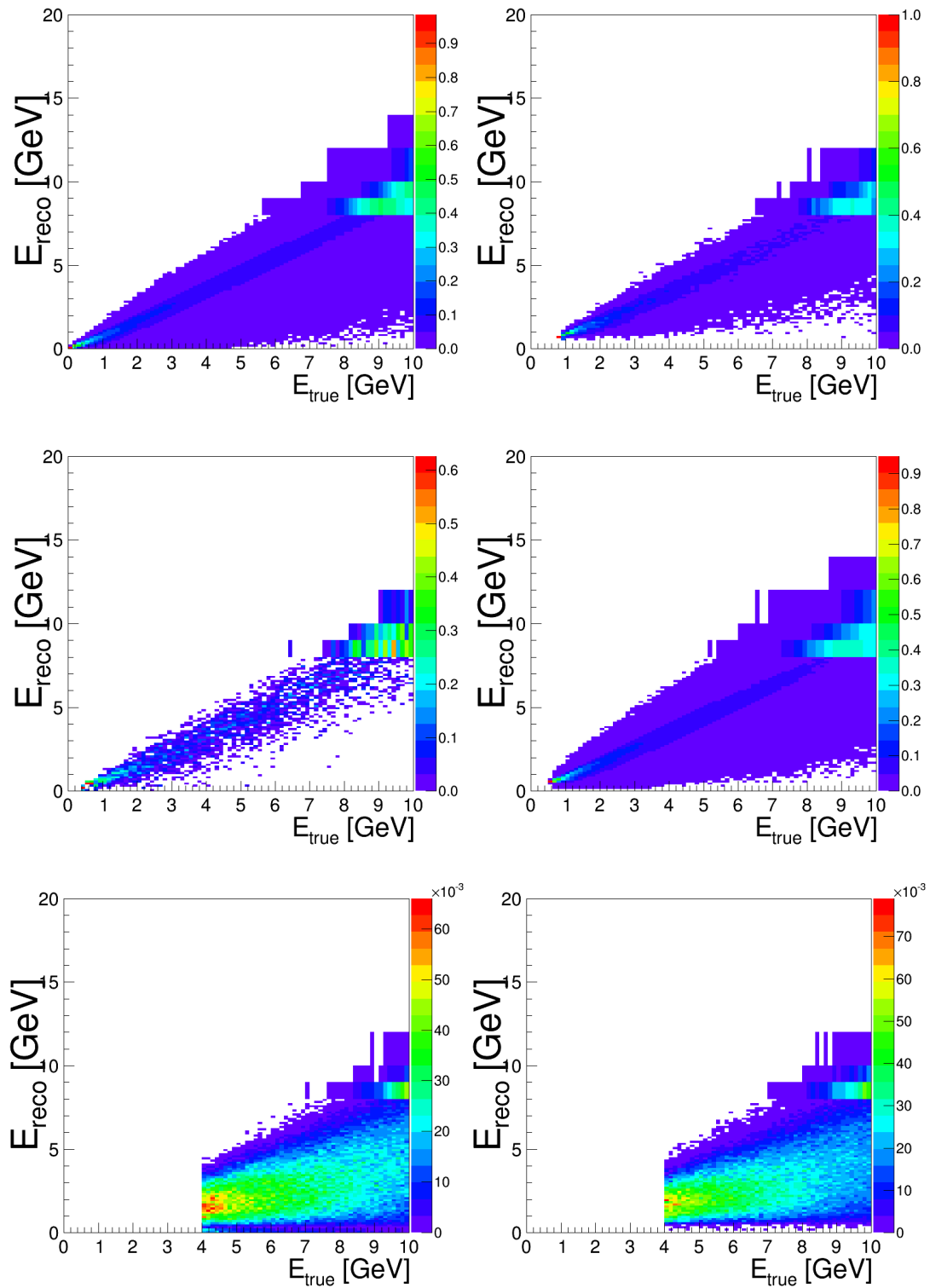
Figure 3.2: True-to-reconstructed energy smearing matrices for ν_e (top), ν_μ (center) and ν_τ (bottom) CC interactions extracted from the Fast MC and used as inputs to GLoBES. Left: Used in the ν_e appearance sample. Right: Used in the ν_μ disappearance samples
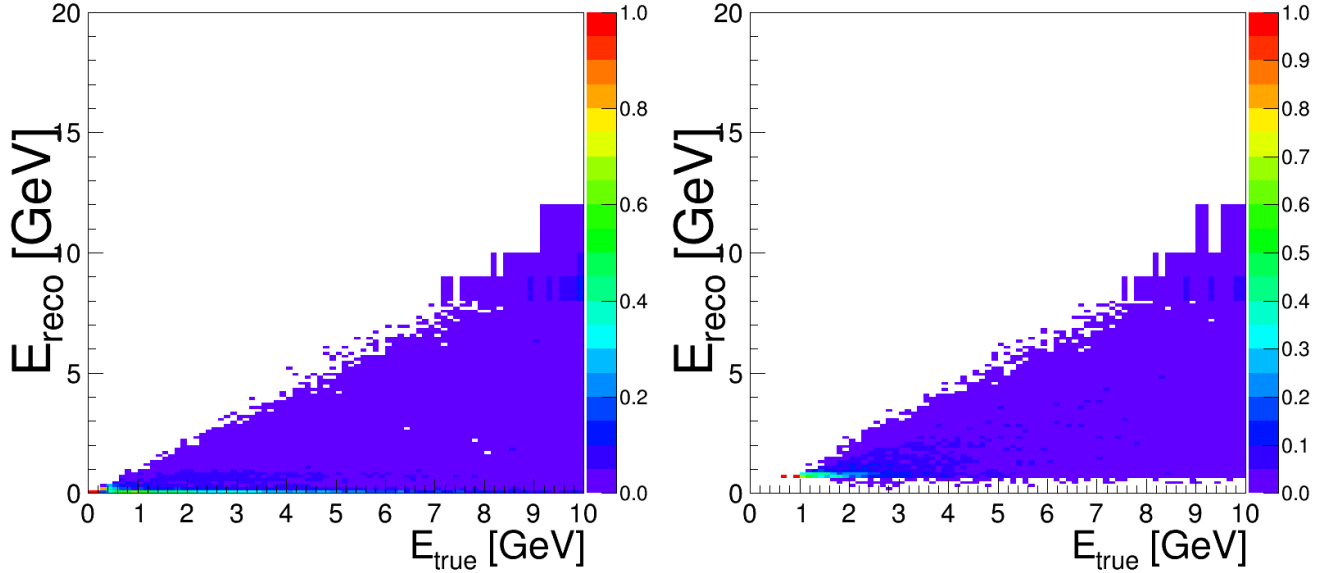
Figure 3.3: True-to-reconstructed energy smearing matrices for NC interactions extracted from the Fast MC and used as inputs to GLoBES. Left: Used in the ν_e appearance sample. Right: Used in the ν_μ disappearance sample.

Table 3.4: Central value and relative uncertainty of neutrino oscillation parameters from a global fit [4] to neutrino oscillation data. Because the probability distributions are somewhat non-Gaussian (particularly for θ_{23}), the relative uncertainty is computed using $1/6$ of the 3σ allowed range from the fit, rather than the 1σ range. For θ_{23} and Δm^2_{31}, the best-fit values and uncertainties depend on whether normal mass hierarchy (NH) or inverted mass hierarchy (IH) is assumed.

Parameter	Central Value	Relative Uncertainty
θ_{12}	0.5843	2.3%
θ_{23} (NH)	0.738	5.9%
θ_{23} (IH)	0.864	4.9%
θ_{13}	0.148	2.5%
Δm^2_{21}	7.5×10^{-5} eV^2	2.4%
Δm^2_{31} (NH)	2.457×10^{-3} eV^2	2.0%
Δm^2_{31} (IH)	-2.449×10^{-3} eV^2	1.9%

Figure 3.4: Analysis sample detection $\times$ selection efficiencies for the various signal and background modes extracted from the Fast MC and used as inputs to GLoBES. Top: Used in the ν_e appearance sample. Bottom: Used in the ν_μ disappearance sample. Left: Neutrino beam mode. Right: Antineutrino beam mode. The NC backgrounds (and ν_μ CC backgrounds for the appearance mode) have been increased by a factor of 10 for visibility.
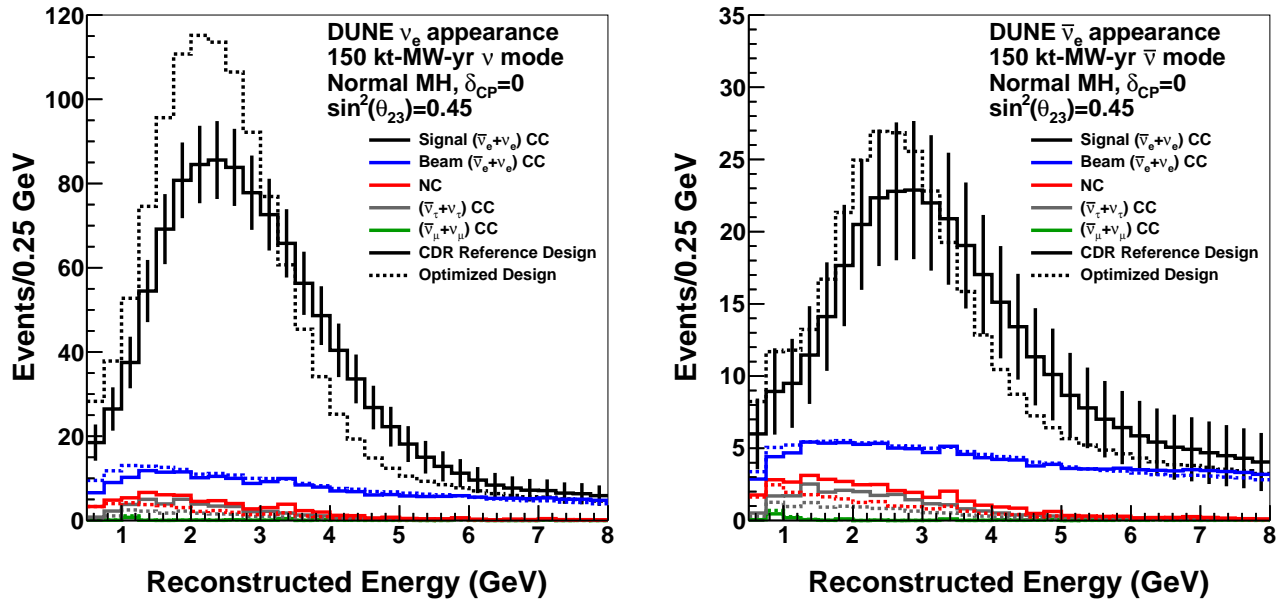
Figure 3.5: ν_e and $\bar{\nu}_e$ appearance spectra: Reconstructed energy distribution of selected ν_e CC-like events assuming a 150 kt · MW · year exposure in the neutrino-beam mode (left) and antineutrino-beam mode (right), for a total 300 kt · MW · year exposure. The plots assume normal mass hierarchy and $\delta_{CP} = 0$. The spectra are shown for both the CDR reference beam design and the optimized beam design as described in Section 3.9.1.
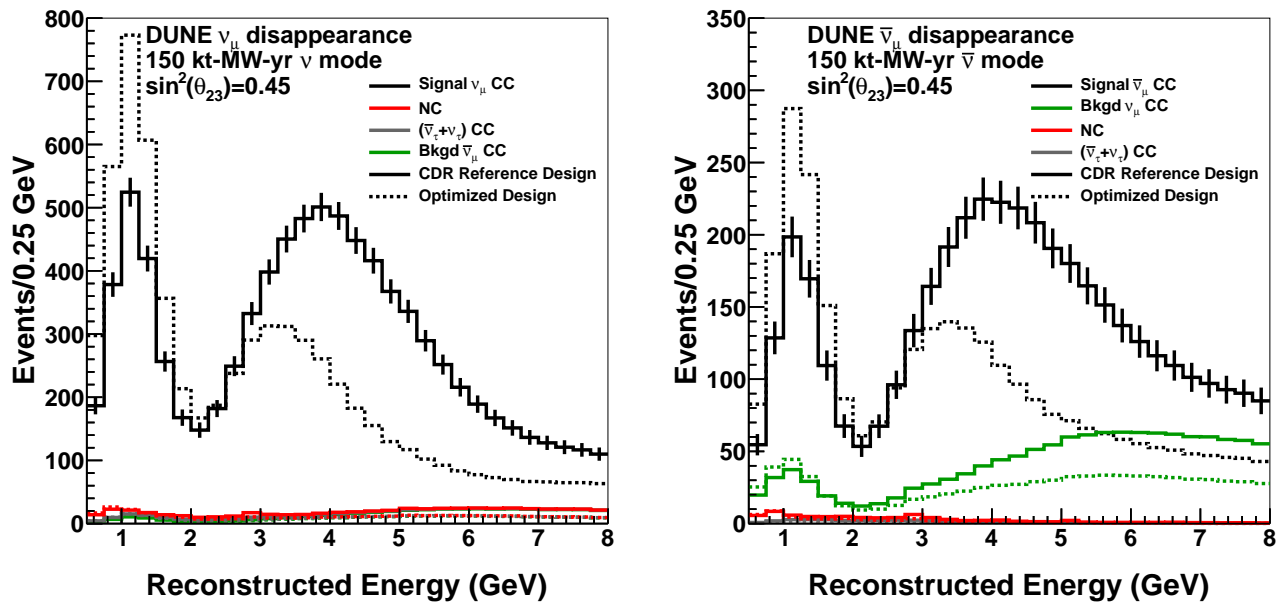
Figure 3.6: ν_μ and $\bar{\nu}_\mu$ disappearance spectra: Reconstructed energy distribution of selected ν_μ CC-like events assuming a 150 kt · MW · year exposure in the neutrino-beam mode (left) and antineutrino-beam mode (right), for a total 300 kt · MW · year exposure. The plots assume normal mass hierarchy and $\delta_{CP} = 0$. The spectra are shown for both the CDR reference beam design and the optimized beam design as described in Section 3.9.1.

Table 3.5: ν_e and $\bar{\nu}_e$ appearance rates: Integrated rate of selected ν_e CC-like events between 0.5 and 8.0 GeV assuming a 150 kt $\cdot$ MW $\cdot$ year exposure in the neutrino-beam mode and antineutrino-beam mode. The signal rates are shown for both normal mass hierarchy (NH) and inverted mass hierarchy (IH), and all the background rates assume normal mass hierarchy. All the rates assume $\delta_{\mathrm{CP}} = 0$, and the rates are shown for both the CDR reference beam design and the optimized beam as described in Section 3.9.1.

	CDR Reference Design	Optimized Design
ν mode (150 kt $\cdot$ MW $\cdot$ year)		
ν_e Signal NH (IH)	861 (495)	945 (521)
$\bar{\nu}_e$ Signal NH (IH)	13 (26)	10 (22)
Total Signal NH (IH)	874 (521)	955 (543)
Beam $\nu_e + \bar{\nu}_e$ CC Bkgd	159	204
NC Bkgd	22	17
$\nu_\tau + \bar{\nu}_\tau$ CC Bkgd	42	19
$\nu_\mu + \bar{\nu}_\mu$ CC Bkgd	3	3
Total Bkgd	226	243
$\bar{\nu}$ mode (150 kt $\cdot$ MW $\cdot$ year)		
ν_e Signal NH (IH)	61 (37)	47 (28)
$\bar{\nu}_e$ Signal NH (IH)	167 (378)	168 (436)
Total Signal NH (IH)	228 (415)	215 (464)
Beam $\nu_e + \bar{\nu}_e$ CC Bkgd	89	105
NC Bkgd	12	9
$\nu_\tau + \bar{\nu}_\tau$ CC Bkgd	23	11
$\nu_\mu + \bar{\nu}_\mu$ CC Bkgd	2	2
Total Bkgd	126	127

Table 3.6: ν_μ and $\bar{\nu}_\mu$ disappearance rates: Integrated rate of selected ν_μ CC-like events between 0.5 and 20.0 GeV assuming a 150 kt $\cdot$ MW $\cdot$ year exposure in the neutrino-beam mode and antineutrino-beam mode. The rates are shown for normal mass hierarchy and $\delta_{\mathrm{CP}} = 0$, and the rates are shown for both the CDR reference beam design and the optimized beam as described in Section 3.9.1.

	CDR Reference Design	Optimized Design
ν mode (150 kt $\cdot$ MW $\cdot$ year)		
ν_μ Signal	10842	7929
$\bar{\nu}_\mu$ CC Bkgd	958	511
NC Bkgd	88	76
$\nu_\tau + \bar{\nu}_\tau$ CC Bkgd	63	29
$\bar{\nu}$ mode (150 kt $\cdot$ MW $\cdot$ year)		
$\bar{\nu}_\mu$ Signal	3754	2639
ν_μ CC Bkgd	2598	1525
NC Bkgd	50	41
$\nu_\tau + \bar{\nu}_\tau$ CC Bkgd	39	18

Sensitivities to the neutrino mass hierarchy and the degree of CP violation are obtained by simultaneously fitting the $\nu_\mu \to \nu_\mu$, $\bar{\nu}_\mu \to \bar{\nu}_\mu$, $\nu_\mu \to \nu_e$, and $\bar{\nu}_\mu \to \bar{\nu}_e$ oscillated spectra. It is assumed that 50% of the total exposure comes in neutrino beam mode and 50% in antineutrino beam mode. A 50%/50% ratio of neutrino to antineutrino data has been shown to produce a nearly optimal sensitivity, and small deviations from this (e.g., 40%/60%, 60%/40%) produce negligible changes in the sensitivity.

The neutrino oscillation parameters are all allowed to vary, constrained by a Gaussian prior with 1σ width as given by the relative uncertainties shown in Table 3.4. The effect of systematic uncertainty is approximated using signal and background normalization uncertainties, which are treated as 100% uncorrelated among the four samples. The baseline systematic uncertainty estimates and the effect of considering larger signal and background normalization uncertainties, as well as some energy-scale uncertainties are discussed in Section 3.6.

In these fits, experimental sensitivity is quantified using a test statistic, $\Delta\chi^2$, which is calculated by comparing the predicted spectra for alternate hypotheses. These quantities are defined, differently for neutrino mass hierarchy and CP-violation sensitivity, to be:

$$\Delta\chi^2_{MH} = \chi^2_{IH} - \chi^2_{NH} \text{ (true normal hierarchy)}, \qquad (3.6)$$
$$\Delta\chi^2_{MH} = \chi^2_{NH} - \chi^2_{IH} \text{ (true inverted hierarchy)}, \qquad (3.7)$$
$$\Delta\chi^2_{CPV} = Min[\Delta\chi^2_{CP}(\delta^{test}_{CP} = 0), \Delta\chi^2_{CP}(\delta^{test}_{CP} = \pi)], \text{ where} \qquad (3.8)$$
$$\Delta\chi^2_{CP} = \chi^2_{\delta^{test}_{CP}} - \chi^2_{\delta^{true}_{CP}}. \qquad (3.9)$$

Since the true value of δ_{CP} is unknown, a scan is performed over all possible values of δ^{true}_{CP}. Both the neutrino mass hierarchy and the θ_{23} octant are also assumed to be unknown and are varied in the fits, with the lowest value of $\Delta\chi^2$ thus obtained used to estimate the sensitivities.

A "typical experiment" is defined as one with the most probable data given a set of input parameters, i.e., in which no statistical fluctuations have been applied. In this case, the predicted spectra and the true spectra are identical; for the example of CP violation, $\chi^2_{\delta^{true}_{CP}}$ is identically zero and the $\Delta\chi^2_{CP}$ value for a typical experiment is given by $\chi^2_{\delta^{test}_{CP}}$.

3.3 Mass Hierarchy

The $1300-$km baseline establishes one of DUNE's key strengths: sensitivity to the matter effect. This effect leads to a large asymmetry in the $\nu_\mu \to \nu_e$ versus $\bar{\nu}_\mu \to \bar{\nu}_e$ oscillation probabilities, the sign of which depends on the mass hierarchy (MH). At 1300 km this asymmetry is approximately $\pm 40\%$ in the region of the peak flux; this is larger than the maximal possible CP-violating asymmetry associated with δ_{CP}, meaning that both the MH and δ_{CP} can be determined unambiguously with high confidence within the same experiment using the beam neutrinos. DUNE's goal is to determine the MH with a significance of at least $\sqrt{\Delta\chi^2} = 5$ for all δ_{CP} values using beam neutrinos. Concurrent analysis of the corresponding atmospheric-neutrino samples will improve the precision with which the MH is resolved.

Figure 3.7 shows the significance with which the MH can be determined as a function of the value of δ_{CP}, for an exposure of 300 kt · MW · year, which corresponds to seven years of data (3.5 years in neutrino mode plus 3.5 years in antineutrino mode) with a 40-kt detector and a 1.07-MW 80-GeV beam. For this exposure, the MH is determined with a minimum significance of $\sqrt{\Delta\chi^2} = 5$ for 100% of the δ_{CP} values for the optimized beam design and nearly 100% of δ_{CP} values for the CDR reference beam design. Figure 3.8 shows the significance with which the MH can be determined for 0% (most optimistic), 50% and 100% of δ_{CP} values as a function of exposure. Minimum exposures of approximately 400 kt · MW · year and 230 kt · MW · year are required to determine the MH with a significance of $\sqrt{\Delta\chi^2} = 5$ for 100% of δ_{CP} values for the CDR reference beam design and the optimized beam design, respectively.

Figure 3.7: The significance with which the mass hierarchy can be determined as a function of the value of δ_{CP} for an exposure of 300 kt · MW · year assuming normal MH (left) or inverted MH (right). The shaded region represents the range in sensitivity due to potential variations in the beam design.

Figures 3.9, 3.10, and 3.11 show the variation in the MH sensitivity due to different values of θ_{23}, θ_{13}, and Δm^2_{31} within the allowed ranges. The value of θ_{23} has the biggest impact on the sensitivity, and the least favorable scenario corresponds to a true value of δ_{CP} in which the MH asymmetry is maximally offset by the leptonic CP asymmetry, and where, independently, $\sin^2 \theta_{23}$ takes on a value at the low end of its experimentally allowed range.

Studies have indicated that special attention must be paid to the statistical interpretation of MH sensitivities [21, 22]. In general, if an experiment is repeated many times, a distribution of $\Delta\chi^2$ values will appear due to statistical fluctuations. It is usually assumed that the $\Delta\chi^2$ metric follows the expected chi-squared function for one degree of freedom, which has a mean of $\overline{\Delta\chi^2}$ and can be interpreted using a Gaussian distribution with a standard deviation of $\sqrt{|\overline{\Delta\chi^2}|}$. In assessing the MH sensitivity of future experiments, it is common practice to generate a simulated data set (for an assumed true MH) that does not include statistical fluctuations. In this typical case, $\overline{\Delta\chi^2}$ is reported as the expected sensitivity, where $\overline{\Delta\chi^2}$ is representative of the mean value of $\Delta\chi^2$ that
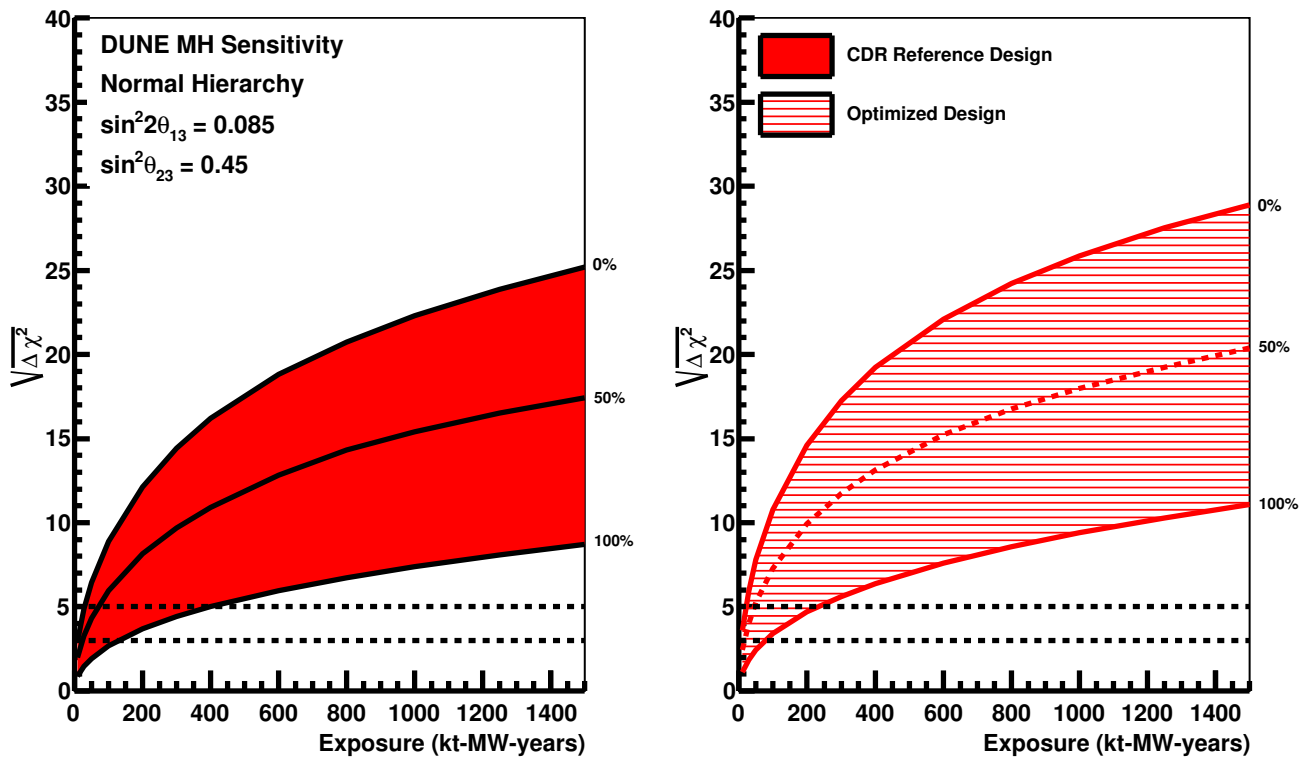
Figure 3.8: The minimum significance with which the mass hierarchy can be determined for all values of δ_{CP} (100%), 50% and in the most optimistic scenario (0%) as a function of exposure. The two different shaded bands represent the different sensitivities due to variations in the beam design. This plot assumes normal mass hierarchy. (The inverted hierarchy case is very similar.)

Figure 3.9: The variation in the MH sensitivity due to different values of θ_{23} within the allowed range. In this figure, the nominal value of $\sin^2 \theta_{23} = 0.45$ provides a significance of at least $\sqrt{\Delta\chi^2} = 5$ for all values of δ_{CP}. (See Figure 3.8 for the possible range of exposures to achieve this level of significance.) The significance decreases for all values of δ_{CP} as $\sin^2 \theta_{23}$ gets smaller.

Figure 3.10: The variation in the MH sensitivity due to different values of θ_{13} within the allowed range. In this figure, he nominal value of $\sin^2 2\theta_{13} = 0.085$ provides a significance of at least $\sqrt{\Delta\chi^2} = 5$ for all values of δ_{CP}. (See Figure 3.8 for the possible range of exposures to achieve this level of significance.)

Figure 3.11: The variation in the MH sensitivity due to different values of Δm_{31}^2 within the allowed range. In this figure, the nominal value of $\Delta m_{31}^2 = 2.46 \times 10^{-3}$ eV^2 provides a significance of at least $\sqrt{\Delta\chi^2} = 5$ for all values of δ_{CP}. (See Figure 3.8 for the possible range of exposures to achieve this level of significance.)

would be obtained in an ensemble of experiments for a particular true MH. With the exception of Figure 3.12, the sensitivity plots in this document have been generated using this method. However, studies in [21, 22] show that, in the case of the mass hierarchy determination, the $\Delta\chi^2$ metric *does not* follow the expected chi-squared function for one degree of freedom. Rather, these studies show that when the observed counts in the experiment are large enough, the distribution of $\Delta\chi^2$ used here approximately follows a Gaussian distribution with a mean and standard deviation of $\overline{\Delta\chi^2}$ and $2\sqrt{|\overline{\Delta\chi^2}|}$, respectively. Because the distribution is atypical, the interpretation of test statistic values in terms of confidence intervals is different than in the standard case.

The effect of statistical fluctuations in the MH measurement is shown in Figure 3.12. The colored bands show the possible range in the significance of a MH determination when statistical fluctuations are included for a measurement that would yield a significance of $\sqrt{\Delta\chi^2} = 5$ for 100% of δ_{CP} values in our standard treatment (the solid blue line). Also shown in Figure 3.12 are horizontal lines that specify the confidence level of an experiment that measures a particular value of $\sqrt{\Delta\chi^2}$, following the convention in [21]. An experiment that measures $\sqrt{\Delta\chi^2} = 5$ (black dashed line) has a 1-3.7 $\times$ 10^{-6} probability of determining the correct MH, while an experiment that measures $\sqrt{\Delta\chi^2} = 3$ (blue dashed line) has a 98.9% probability of determining the correct MH. An experiment that measures $\sqrt{\Delta\chi^2} = 0$ (cyan dashed line) has a 50% probability of determining the correct MH. In this case, both hypotheses (normal or inverted hierarchy) fit the data equally well, and the probability of guessing correctly is 50%.

3.4   CP-Symmetry Violation

In the particular parameterization of the PMNS matrix shown in Equation 3.2, the middle factor labeled "II" describes the mixing between the ν_1 and ν_3 mass states, and depends on the CP-violating phase δ_{CP}. With the recent measurement of θ_{13}, it is now known that the minimal conditions required for measuring δ_{CP} in the three-flavor framework have been met; all three mixing angles are nonzero, and there are two distinct mass splittings. In the approximation for the electron neutrino appearance probability given in Equation 3.6, expanding the middle term results in the presence of CP-odd terms (dependent on $\sin\delta_{\mathrm{CP}}$) that have opposite signs in $\nu_\mu \to \nu_e$ and $\bar{\nu}_\mu \to \bar{\nu}_e$ oscillations. For $\delta_{\mathrm{CP}} \neq 0$ or π, these terms introduce an asymmetry in neutrino versus antineutrino oscillations. The magnitude of the CP-violating terms in the oscillation depends most directly on the size of the Jarlskog Invariant [23], a function that was introduced to provide a measure of CP violation independent of the mixing-matrix parameterization. In terms of the parameterization presented in Equation 3.2, the Jarlskog Invariant is:

$$J_{CP}^{\mathrm{PMNS}} \equiv \frac{1}{8}\sin 2\theta_{12}\sin 2\theta_{13}\sin 2\theta_{23}\cos\theta_{13}\sin\delta_{\mathrm{CP}}. \qquad (3.10)$$

The relatively large values of the mixing angles in the lepton sector imply that leptonic CP-violation effects may be quite large — depending on the value of the phase δ_{CP}, which is currently unknown. Experimentally, it is unconstrained at the 3σ level by the global fit [4]. Given the current best-fit values of the mixing angles [4] and assuming normal hierarchy,

$$J_{CP}^{\mathrm{PMNS}} \approx 0.03\sin\delta_{\mathrm{CP}}. \qquad (3.11)$$
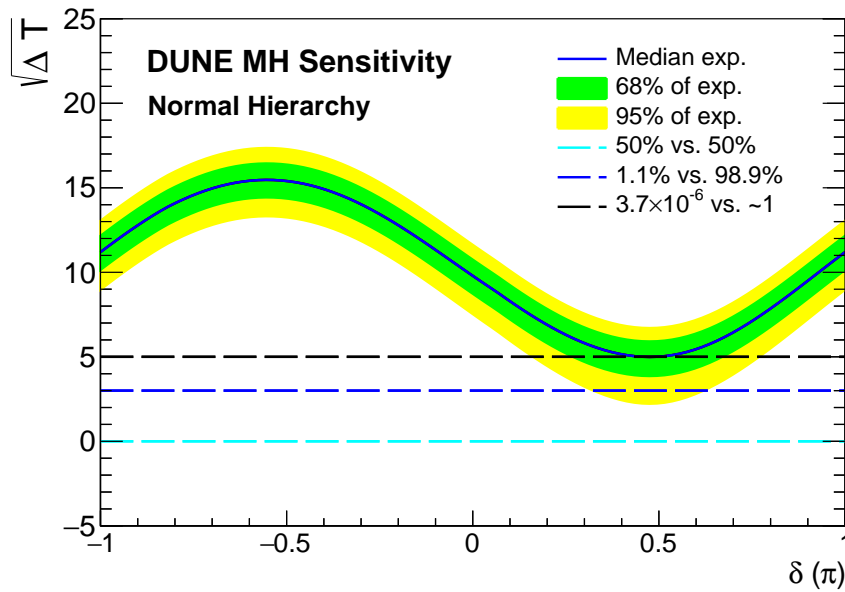
Figure 3.12:   The sensitivity, given by $\sqrt{\Delta T} = \sqrt{\Delta\chi^2}$ for a typical experiment (solid blue line), is compared to the bands within which 68% (green) and 95% (yellow) of experiments are expected to fall due to statistical fluctuations. The solid blue line (representing a minimum significance of $\sqrt{\Delta T} = 5$ for 100% of δ_{CP} values) is the expected sensitivity in our standard treatment. (See Figure 3.8 for the possible range of exposures to achieve this level of significance.) The dashed lines show the values of the $\sqrt{\Delta T}$ metric an experiment must measure for the probability of determining the correct neutrino MH to be 50% (cyan), 98.9% (blue), or 1 to 3.7×10^{-6} (black), following the convention in [21]. In the legend, the numbers corresponding to the dashed lines indicate [probability of determining MH *incorrectly*] vs. [probability of determining the MH *correctly*].

This is in sharp contrast to the very small mixing in the quark sector, which leads to a very small value of the corresponding quark-sector Jarlskog Invariant [24],

$$J_{CP}^{\mathrm{CKM}} \approx 3 \times 10^{-5}, \tag{3.12}$$

despite the large value of $\delta_{CP}^{\mathrm{CKM}} \approx 70°$.

The variation in the $\nu_\mu \to \nu_e$ oscillation probability (Equation 3.6) with the value of δ_{CP} indicates that it is experimentally possible to measure the value of δ_{CP} at a fixed baseline using only the observed shape of the $\nu_\mu \to \nu_e$ *or* the $\bar\nu_\mu \to \bar\nu_e$ appearance signal measured over an energy range that encompasses at least one full oscillation interval. A measurement of the value of $\delta_{\mathrm{CP}} \neq 0$ or π, assuming that neutrino mixing follows the three-flavor model, would imply CP violation.

The CP asymmetry, $\mathcal{A}_{CP}$, is defined as

$$\mathcal{A}_{CP} = \frac{P(\nu_\mu \to \nu_e) - P(\bar\nu_\mu \to \bar\nu_e)}{P(\nu_\mu \to \nu_e) + P(\bar\nu_\mu \to \bar\nu_e)}. \tag{3.13}$$

In the three-flavor model the asymmetry can be approximated to leading order in Δm_{21}^2 as [25]:

$$\mathcal{A}_{CP} \sim \frac{\cos\theta_{23} \sin 2\theta_{12} \sin\delta_{\mathrm{CP}}}{\sin\theta_{23} \sin\theta_{13}} \left(\frac{\Delta m_{21}^2 L}{4 E_\nu} \right) + \text{matter effects} \tag{3.14}$$

Regardless of the measured value obtained for δ_{CP}, the explicit observation of the asymmetry $\mathcal{A}_{CP}$ in $\nu_\mu \to \nu_e$ and $\bar\nu_\mu \to \bar\nu_e$ oscillations is sought to directly demonstrate the leptonic CP-violation effect. A measurement of δ_{CP} that is inconsistent with the measurement of $\mathcal{A}_{CP}$ according to Equation 3.14 could be evidence of physics beyond the standard three-flavor model. Furthermore, for long-baseline experiments such as DUNE where the neutrino beam propagates through the Earth's mantle, the leptonic CP-violation effects must be disentangled from the matter effects, discussed in Section 3.3.

Figure 3.13 shows the significance with which the CP violation ($\delta_{\mathrm{CP}} \neq 0$ or π) can be determined as a function of the value of δ_{CP} for an exposure of 300 kt · MW · year, which corresponds to seven years of data (3.5 years in neutrino mode plus 3.5 years in antineutrino mode) with a 40-kt detector and a 1.07-MW 80-GeV beam. Figure 3.14 shows the significance with which CP violation can be determined for 25%, 50% or 75% of δ_{CP} values as a function of exposure. Table 3.7 lists the minimum exposure required to determine CP violation with a significance of 5σ for 50% of δ_{CP} values or 3σ for 75% of δ_{CP} values for both the CDR reference beam design and the optimized beam design. The CP-violation sensitivity as a function of δ_{CP} as shown in Figure 3.13 has a characteristic double peak structure because the significance of a CP-violation measurement necessarily drops to zero where there is no CP violation: at the CP-conserving values of $-\pi$, 0, and π. Therefore, unlike the MH determination, it's not possible for any experiment to provide 100% coverage in δ_{CP} for a CP-violation measurement because CP-violation effects vanish at certain values of δ_{CP}.

Figures 3.15, 3.16, and 3.17 show the variation in the CP sensitivity due to different values of θ_{23}, θ_{13}, and Δm_{31}^2 within the allowed ranges. The value of θ_{23} has the biggest impact on the sensitivity, and the least favorable scenario corresponds to a value of $\sin^2\theta_{23}$ at the high end of its experimentally allowed range.
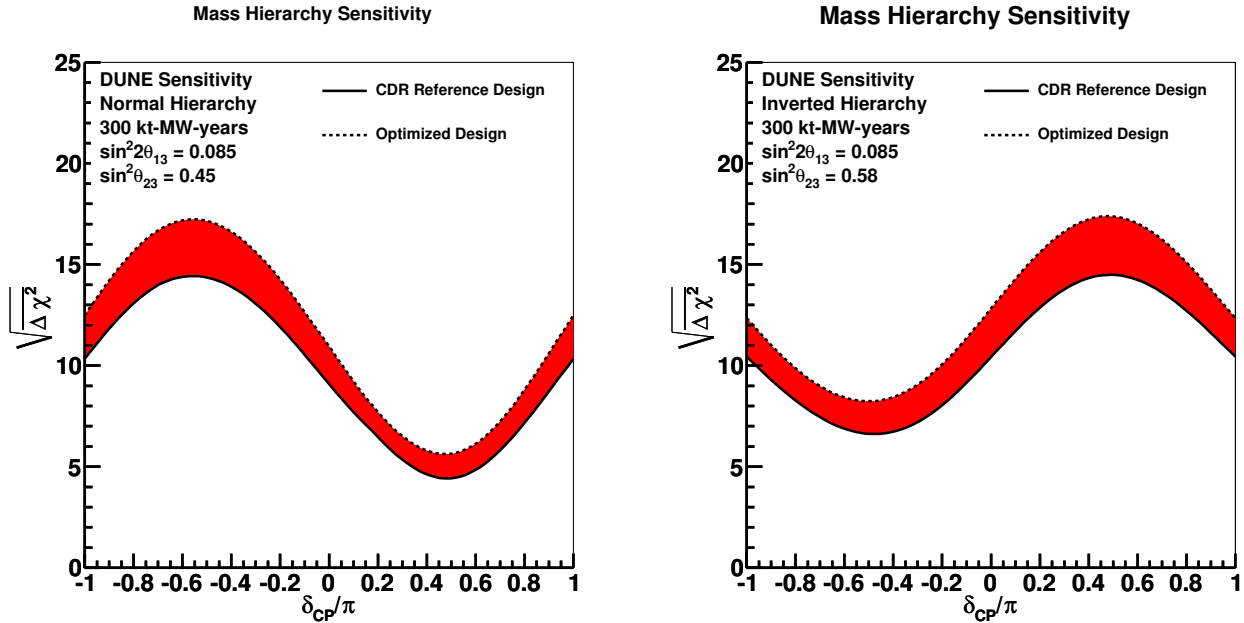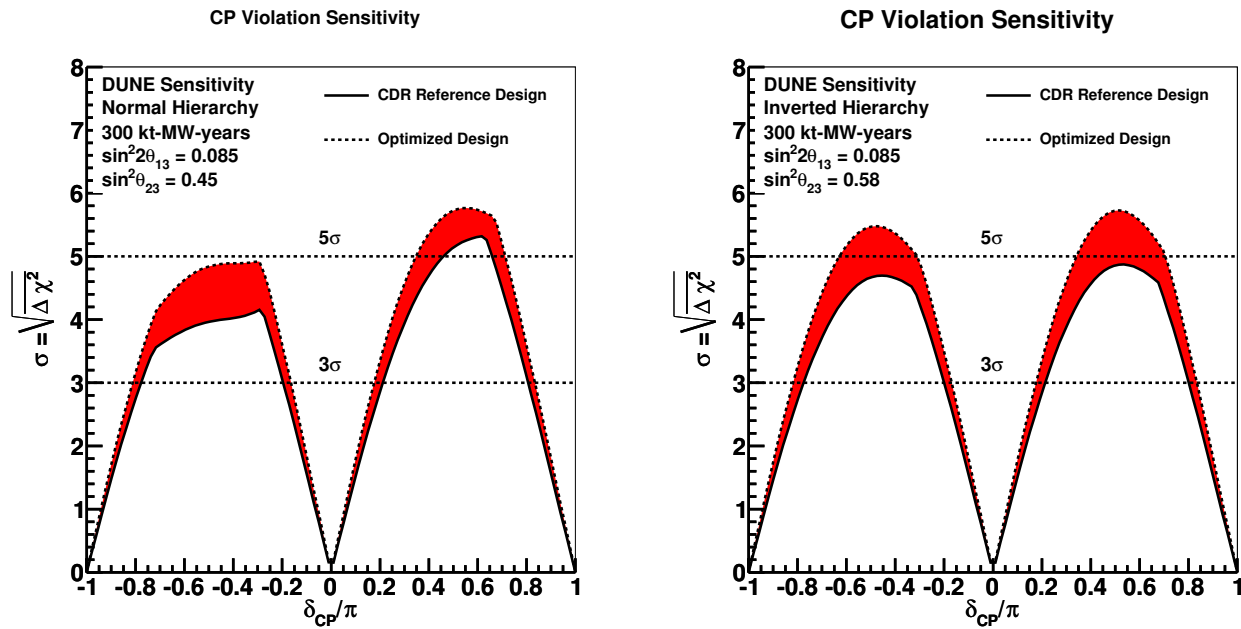
Figure 3.13: The significance with which the CP violation can be determined as a function of the value of δ_{CP} for an exposure of 300 kt · MW · year assuming normal MH (left) or inverted MH (right). The shaded region represents the range in sensitivity due to potential variations in the beam design.

Table 3.7: The minimum exposure required to determine CP violation with a significance of 3σ for 75% of δ_{CP} values or 5σ for 50% of δ_{CP} values for the CDR reference beam design and the optimized beam design.

Significance	CDR Reference Design	Optimized Design
3σ for 75% of δ_{CP} values	1320 kt · MW · year	850 kt · MW · year
5σ for 50% of δ_{CP} values	810 kt · MW · year	550 kt · MW · year
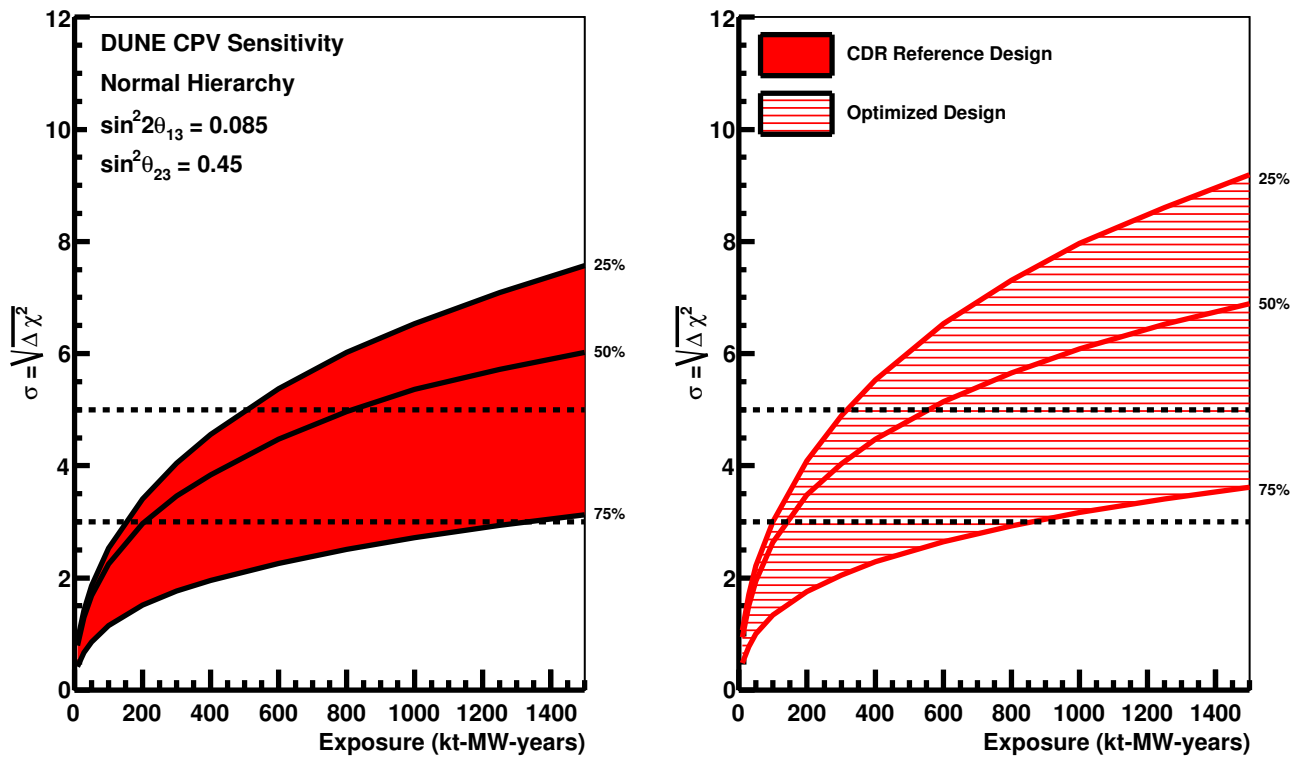
Figure 3.14: The minimum significance with which CP violation can be determined for 25%, 50% and 75% of δ_{CP} values as a function of exposure. The two different shaded bands represents the different sensitivities due to potential variations in the beam design. This plot assumes normal mass hierarchy.
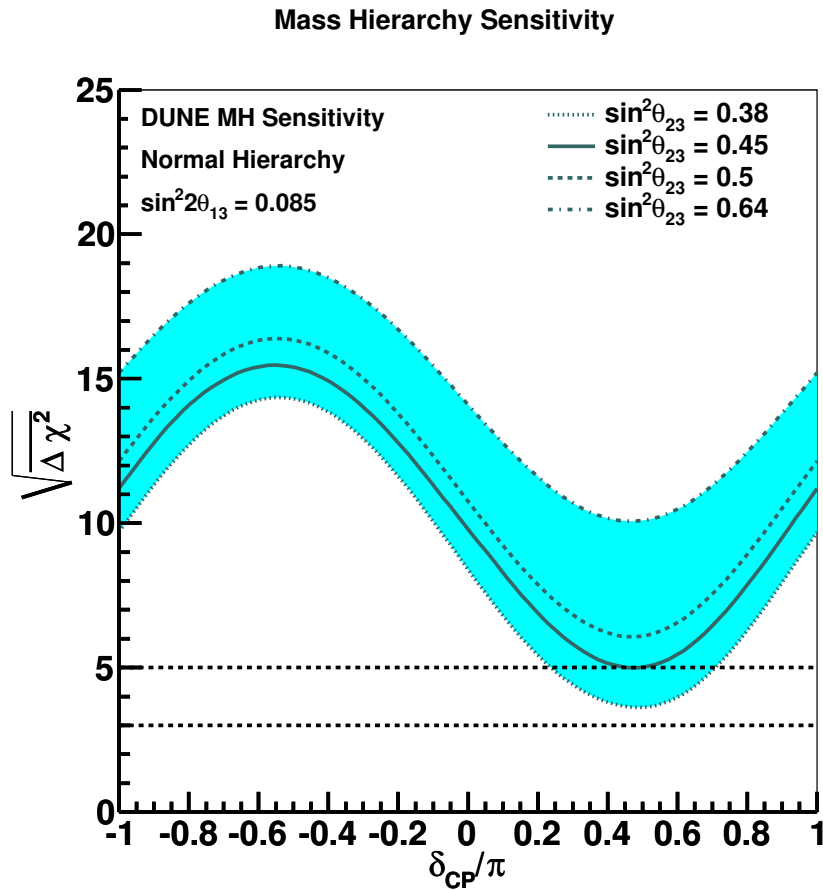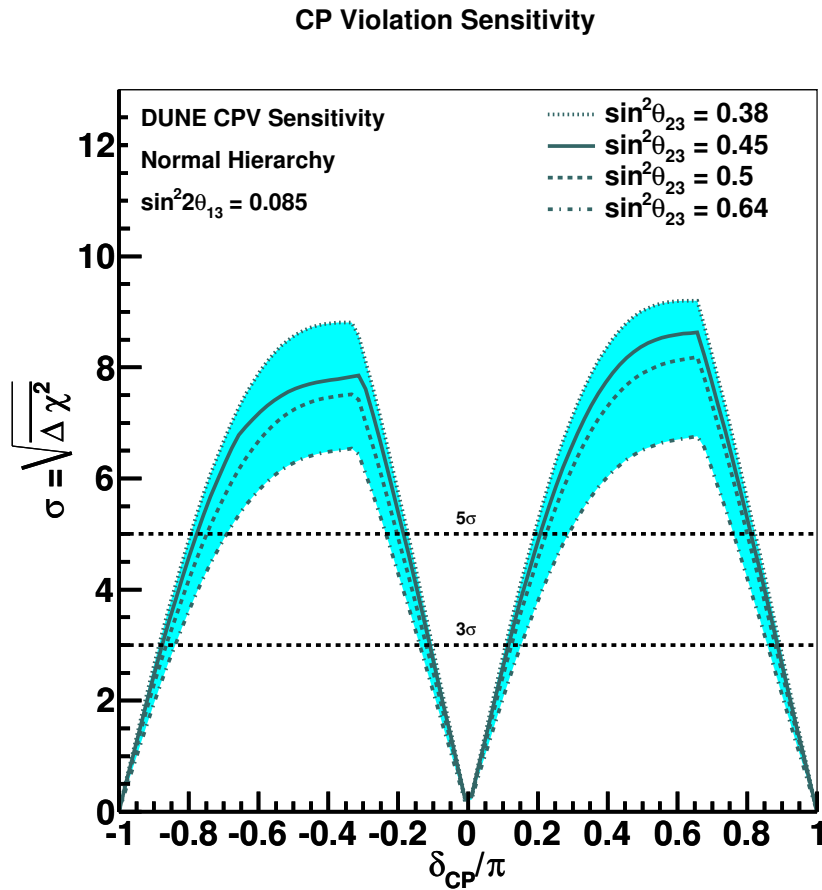
Figure 3.15: The variation in the CP sensitivity due to different values of θ_{23} within the allowed range. In this figure, the nominal value of $\sin^2 \theta_{23} = 0.45$ provides a significance of at least 3σ for 75% of δ_{CP} values. (See Figure 3.14 for the possible range of exposures to achieve this level of significance.) The significance decreases for all values of δ_{CP} as $\sin^2 \theta_{23}$ gets larger.
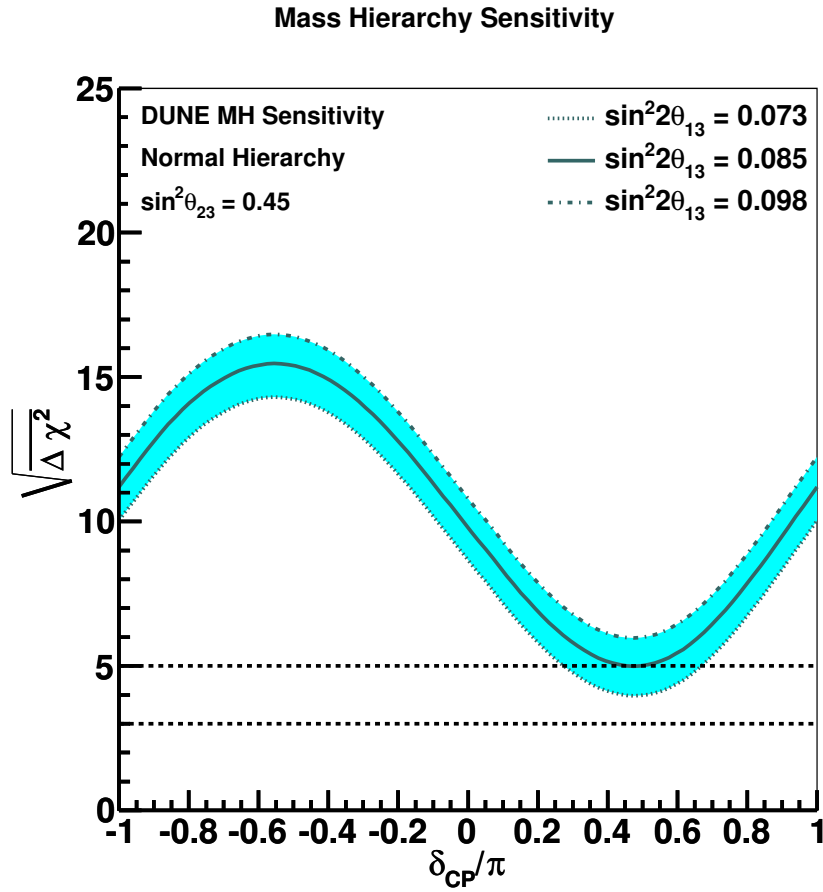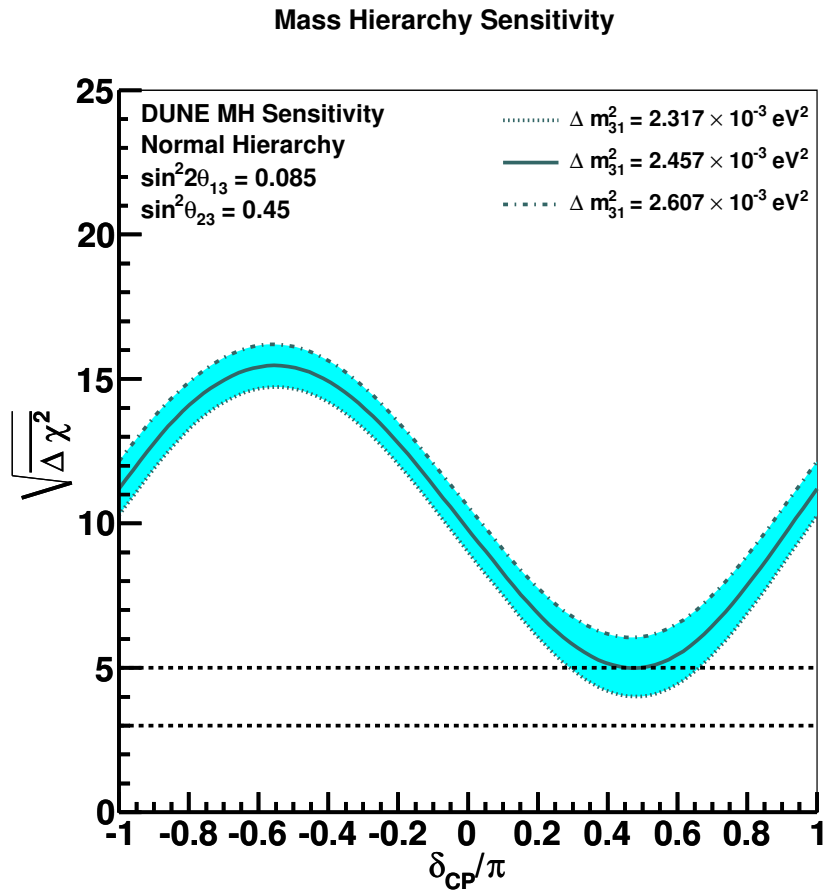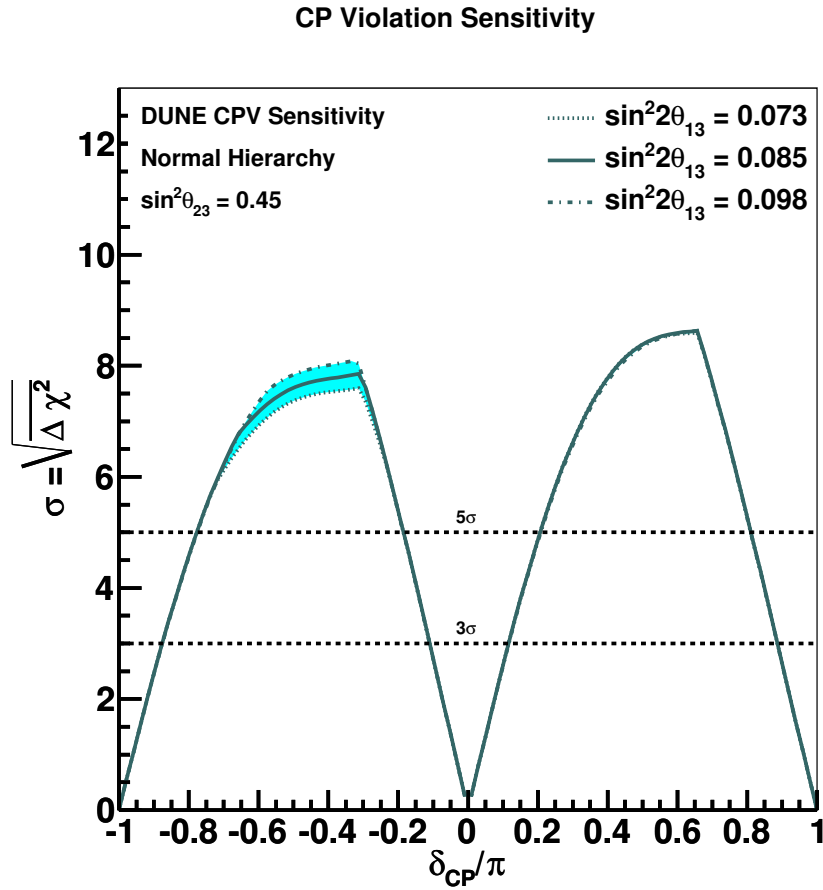
Figure 3.16: The variation in the CP sensitivity due to different values of θ_{13} within the allowed range. In this figure, the nominal value of $\sin^2 2\theta_{13} = 0.085$ provides a significance of at least 3σ for 75% of δ_{CP} values. (See Figure 3.14 for the possible range of exposures to achieve this level of significance.)
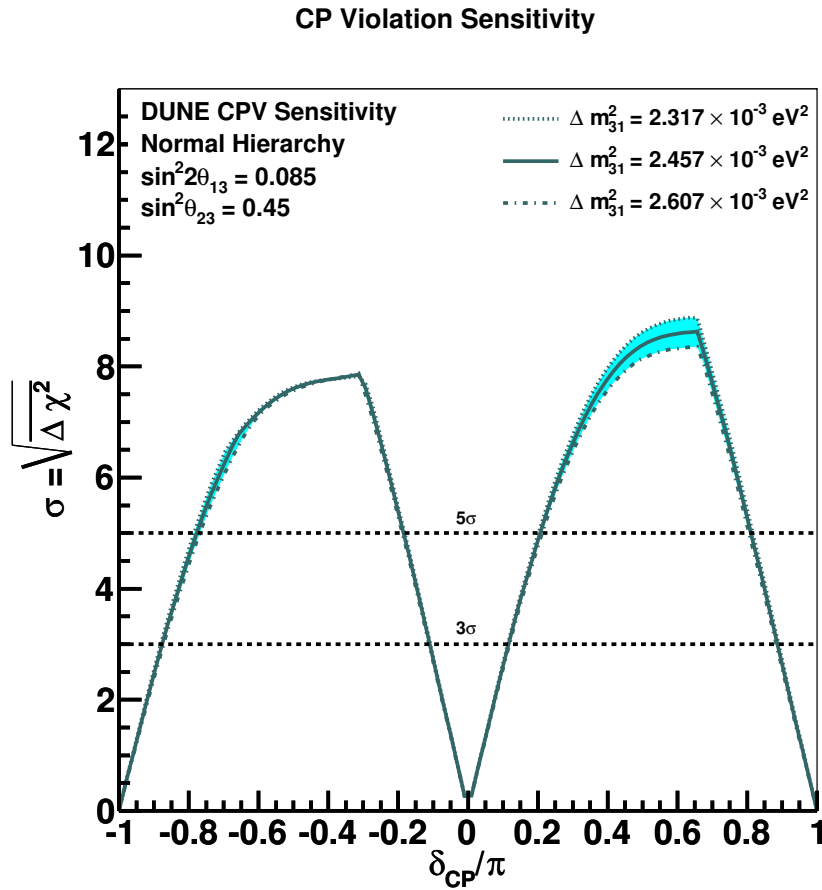
Figure 3.17: The variation in the CP sensitivity due to different values of Δm^2_{31} within the allowed range. In this figure, the nominal value of $\Delta m^2_{31} = 2.46 \times 10^{-3}$ eV^2 provides a significance of at least 3σ for 75% of δ_{CP} values. (See Figure 3.14 for the possible range of exposures to achieve this level of significance.)

3.5   Precision Oscillation Parameter Measurements

In addition to the discovery potential for neutrino mass hierarchy and CP-violation, DUNE will improve the precision on key parameters that govern neutrino oscillations, including:

- $\sin^2\theta_{23}$ and the octant of θ_{23}

- δ_{CP}

- $\sin^2 2\theta_{13}$

- Δm^2_{31}

Higher-precision measurements of the known oscillation parameters improves sensitivity to physics beyond the three-flavor oscillation model, particularly when compared to independent measurements by other experiments, including reactor measurements of θ_{13} and measurements with atmospheric neutrinos.

The most precise measurement of $\sin^2\theta_{23}$ to date comes from T2K, $\sin^2\theta_{23} = 0.514^{+0.055}_{-0.056}$ (normal hierarchy) and $\sin^2\theta_{23} = 0.511 \pm 0.055$ (inverted hierarchy) [26]. This corresponds to a value of θ_{23} near 45°, but leaves an ambiguity as to whether the value of θ_{23} is in the lower octant (less than 45°), the upper octant (greater than 45°), or exactly 45°. The value of $\sin^2\theta_{23}$ from the global fit reported by [4] is $\sin^2\theta_{23} = 0.452^{+0.052}_{-0.028}(1\sigma)$ for normal hierarchy (NH), but the distribution of the χ^2 from the global fit has another local minimum – particularly if the MH is inverted – at $\sin^2\theta_{23} = 0.579^{+0.025}_{-0.037}(1\sigma)$. A *maximal* mixing value of $\sin^2\theta_{23} = 0.5$ is therefore still allowed by the data and the octant is still largely undetermined. A value of θ_{23} exactly equal to 45° would indicate that ν_μ and ν_τ have equal contributions from ν_3, which could be evidence for a previously unknown symmetry. It is therefore important experimentally to determine the value of $\sin^2\theta_{23}$ with sufficient precision to determine the octant of θ_{23}. The measurement of $\nu_\mu \to \nu_\mu$ oscillations is sensitive to $\sin^2 2\theta_{23}$, whereas the measurement of $\nu_\mu \to \nu_e$ oscillations is sensitive to $\sin^2\theta_{23}$. A combination of both ν_e appearance and ν_μ disappearance measurements can probe both maximal mixing and the θ_{23} octant. The $\Delta\chi^2$ metric is defined as:

$$\Delta\chi^2_{octant} \;=\; |\chi^2_{\theta^{test}_{23}>45°} - \chi^2_{\theta^{test}_{23}<45°}|, \tag{3.15}$$

where the value of θ_{23} in the *wrong* octant is constrained only to have a value within the *wrong* octant (i.e., it is not required to have the same value of $\sin^2 2\theta_{23}$ as the true value). Figure 3.18 shows the sensitivity to determining the octant as a function of θ_{23}. Figure 3.19 shows the resolution of $\sin^2\theta_{23}$ as a function of exposure, assuming the true value is $\sin^2\theta_{23} = 0.45$ from the current global fit.

As mentioned in Section 3.4, DUNE will seek not only to demonstrate explicit CP violation by observing a difference in the neutrino and antineutrino oscillation probabilities, but also to measure the value of the parameter δ_{CP}. Figure 3.20 shows the resolution of δ_{CP} as a function of exposure for a CP-conserving value ($\delta_{CP} = 0$) and the value that gives the maximum CP violation for normal MH ($\delta_{CP} = 90°$). Minimum exposures of approximately 450 kt · MW · year and 290 kt · MW · year

Octant Sensitivity
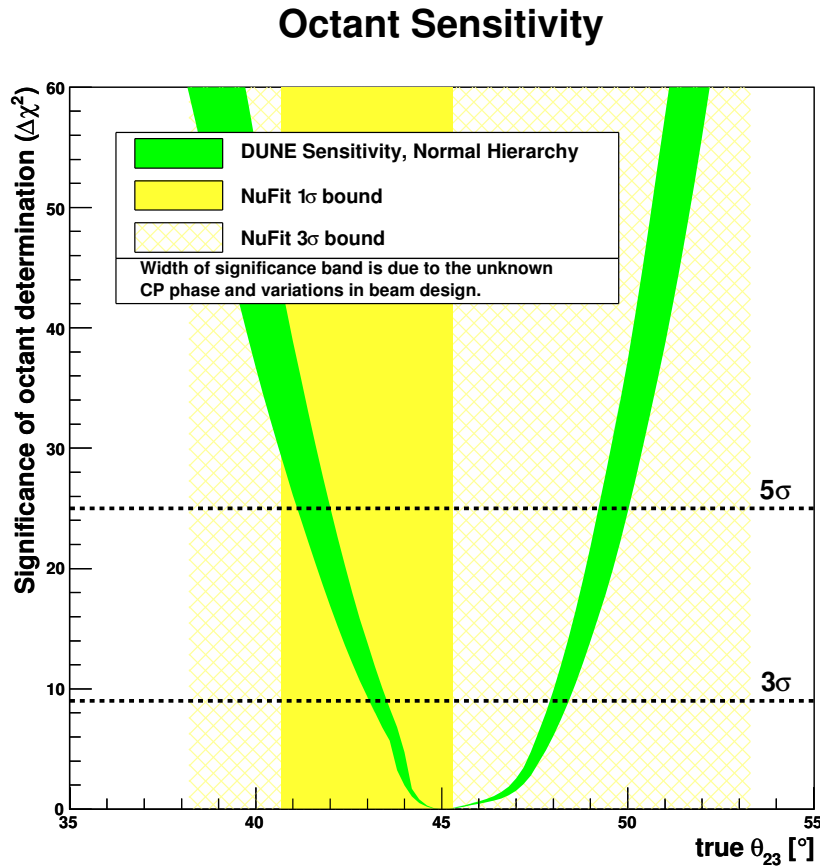
Figure 3.18: The significance with which DUNE can resolve the θ_{23} octant as a function of the true value of θ_{23}. The green shaded band around the curve represents the range in sensitivity due to potential variations in the beam design and in the true value of δ_{CP}. The yellow shaded regions indicate the current 1σ and 3σ bounds on the value of θ_{23} from a global fit. The same exposure that gives a 3σ measurement of CP violation for 75% of the values of δ_{CP} is assumed. See Figure 3.14 for the possible range of exposure to achieve this significance.
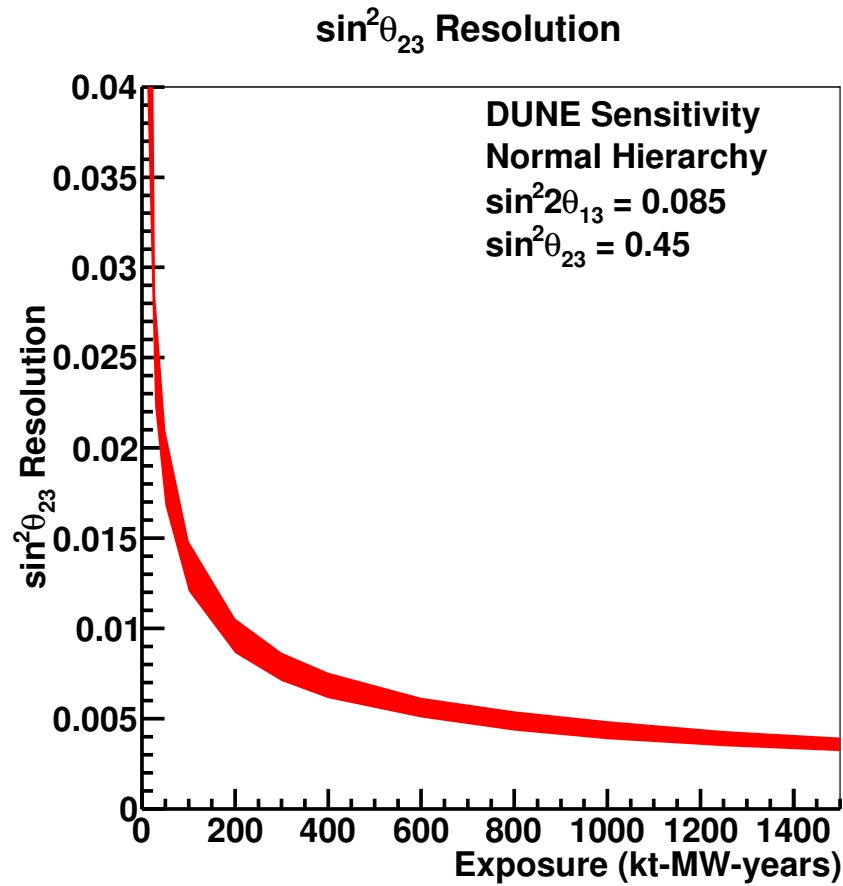
Figure 3.19: The resolution of a measurement of $\sin^2\theta_{23}$ as a function of exposure assuming normal MH and $\sin^2\theta_{23} = 0.45$ from the current global fit. The shaded region represents the range in sensitivity due to potential variations in the beam design.

are required to measure δ_{CP} with a resolution of $10°$ for the CDR reference beam design and the optimized beam design, respectively, for a true value $\delta_{CP} = 0$.
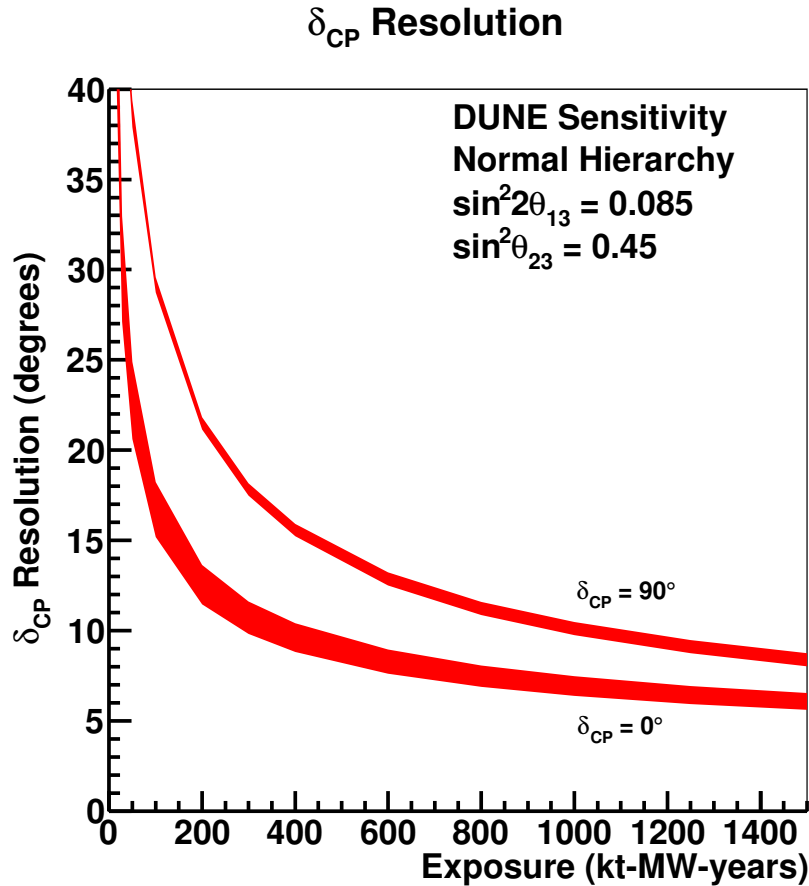
δ_{CP} Resolution

Figure 3.20: The resolution of a measurement of δ_{CP} as a function of exposure assuming normal MH. The resolution is shown for a CP-conserving value ($\delta_{CP} = 0$) and the value that gives the maximum CP violation for normal MH ($\delta_{CP} = 90°$). The shaded region represents the range in sensitivity due to potential variations in the beam design.

The rich oscillation structure that can be observed by DUNE and the excellent particle identification capability of the detector will enable precision measurement in a single experiment of all the mixing parameters governing ν_1-ν_3 and ν_2-ν_3 mixing. Theoretical models probing quark-lepton universality predict specific values of the mixing angles and the relations between them. The mixing angle θ_{13} is expected to be measured accurately in reactor experiments by the end of the decade with a precision that will be limited by systematics. The combined statistical and systematic uncertainty on the value of $\sin^2 2\theta_{23}$ from the Daya Bay reactor neutrino experiment, which has the lowest systematics, is currently $\sim 6\%$ ($\sin^2 2\theta_{13} = 0.084 \pm 0.005$), with a projected uncertainty of $\sim 3\%$ by 2017 [27]. While the constraint on θ_{13} from the reactor experiments will be important in the early stages of DUNE for determining CP violation, measuring δ_{CP} and determining the θ_{23} octant, DUNE itself will eventually be able to measure θ_{13} independently with a similar precision to that expected from the reactor experiments. Whereas the reactor experiments measure θ_{13} using $\bar{\nu}_e$ disappearance, DUNE will measure it through ν_e and $\bar{\nu}_e$ appearance, thus providing an independent constraint on the three-flavor mixing matrix. Figure 3.21 shows the resolution of $\sin^2 2\theta_{13}$ as a function of exposure, assuming the true value is $\sin^2 2\theta_{13} = 0.085$ from the current
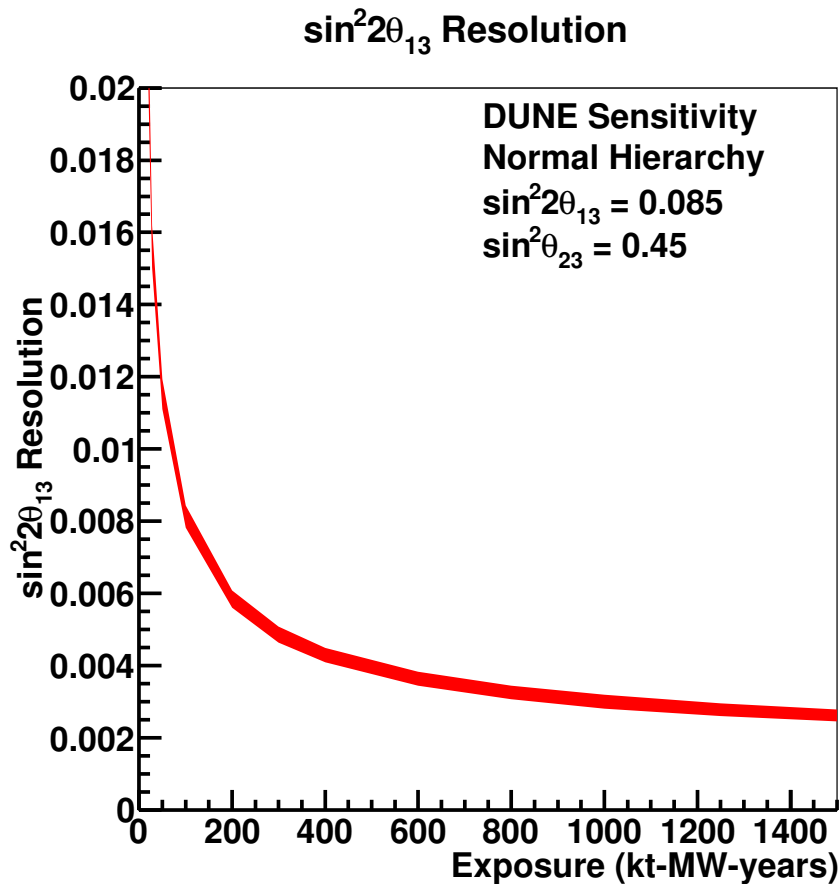
global fit.

Figure 3.21: The resolution of a measurement of $\sin^2 2\theta_{13}$ as a function of exposure assuming normal MH and $\sin^2 2\theta_{13} = 0.085$ from the current global fit. The shaded region represents the range in sensitivity due to potential variations in the beam design.

DUNE can also significantly improve the resolution on the larger mass splitting beyond the precision of current experiments. The current best-fit value for Δm^2_{32} from MINOS is $|\Delta m^2_{32}| = (2.34 \pm 0.09) \times 10^{-3}$ eV^2 (normal hierarchy) and $|\Delta m^2_{32}| = (2.37^{+0.11}_{-0.07}) \times 10^{-3}$ eV^2 (inverted hierarchy) [28], with comparable precision achieved by both Daya Bay and T2K. The precision on Δm^2_{31} will ultimately depend on tight control of energy-scale systematics. Figure 3.22 shows the expected resolution of Δm^2_{31} as a function of exposure, assuming the true value is $\Delta m^2_{31} = 2.457 \times 10^{-3}$ eV^2 from the current global fit.

3.6   Effect of Systematic Uncertainties

Sensitivity studies presented in Section 3.2 test the ability to distinguish the expected number of ν_e appearance and ν_μ disappearance events given a set of oscillation parameters from the expectations given an alternate set of parameters. For example, the CP-violation and MH-sensitivity studies test the spectral differences induced by shifting δ_{CP} away from 0.0 and π and by changing the
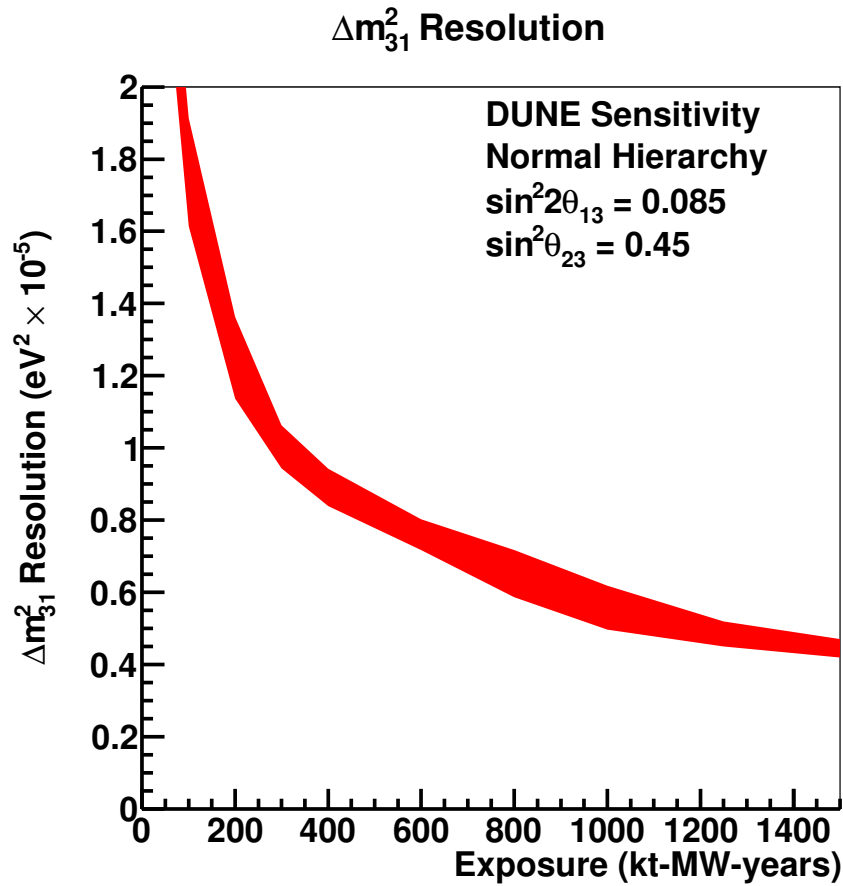
Figure 3.22: The resolution of a measurement of Δm^2_{31} as a function of exposure assuming the true value is $\Delta m^2_{31} = 2.457 \times 10^{-3}$ eV^2 from the current global fit. The shaded region represents the range in sensitivity due to potential variations in the beam design.

mass hierarchy. These differences are quantified with a test statistic (see Equation 3.6 - 3.9) which accounts for statistical and systematic uncertainties.

The effect of systematic uncertainty in the models used to predict these spectra is included by allowing the parameters to vary within Gaussian ranges. In the fits, these systematic nuisance parameters are profiled, i.e., the set of nuisance parameters that produces the minimum value of the test statistic is chosen. The central values of the oscillation parameters and their relative uncertainties are taken from the Nu-Fit [4] global fit to neutrino data; these values are given in Table 3.4. Uncertainty in non-oscillation parameters is approximated using normalization uncertainties on each constituent interaction mode that comprise the signal and background in each sample. The values for these normalization uncertainties are chosen based on current constraints on underlying model parameters, the ability of previous experiments to constrain these quantities, and the expected capability of the DUNE near detector (ND) as outlined in the Near Detector Reference Design chapter of Volume 4: *The DUNE Detectors at LBNF*. Consideration is also given to the sources of uncertainty that go into each of the effective normalization parameters and how they may be correlated among the different far detector (FD) analysis samples that will be fit in combination.

In the following sections, a justification is presented for the chosen values of the signal and background normalization uncertainties and their respective correlations. Studies that consider the effect of varying the size of the residual normalization uncertainties on the ν_e and $\bar{\nu}_e$ samples are also presented. Finally the ongoing effort to characterize and evaluate the effect of individual sources of uncertainty when propagated to oscillation parameter measurements in the DUNE experiment is described.

3.6.1   Far Detector Samples

Uncertainties in DUNE will be constrained by external data, near detector data, and a combined fit to the four (ν_e appearance, $\bar{\nu}_e$ appearance, ν_μ disappearance, $\bar{\nu}_\mu$ disappearance) far detector samples. This four-sample fit is alternatively referred to as a three-flavor analysis, because the constraints depend upon the validity of the three-flavor model of neutrino oscillation.

The ν_μ disappearance analysis sample is composed of ν_μ CC interactions with backgrounds from NC interactions in which a charged pion is misidentified as a muon and ν_τ CC interactions in which the resulting tau decays to a muon and two neutrinos. The unoscillated ν_μ rate and spectrum are expected to be well constrained by the near detector. The uncertainty on the neutral current (NC) background comes primarily from uncertainty in pion production rates for the coherent, resonance, and DIS channels, as well as modeling of pion topological signatures that determine the likelihood of it being misidentified as a muon. Uncertainties in the ν_τ CC background level arise from the uncertainty in the ν_τ/ν_μ cross section ratio, which cannot be directly constrained by ND measurements.

The ν_e appearance sample is composed of ν_e CC interactions resulting from $\nu_\mu \rightarrow \nu_e$ oscillation and background from intrinsic beam ν_e interactions, NC and ν_μ CC interactions in which a photon from a final-state neutral pion is misidentified as an electron, and ν_τ interactions in which the

resulting τ decays to an electron and two neutrinos. Since the ν_μ disappearance signal and the ν_e appearance signal are produced by the same flux, the ν_e appearance signal is constrained relative to the ν_μ signal. The residual uncorrelated uncertainty on the ν_e signal results from the statistical limitations of the ν_μ constraint, differences in energy scale and selection efficiency between the samples, and theoretical uncertainties on the ν_e/ν_μ cross section ratio. The uncertainty on the intrinsic beam ν_e background is dominated by flux uncertainties which are constrained by the near detector and the observed ν_μ events. Predictions for NC and ν_μ CC background rates are limited by the uncertainties on pion production rates, the $\pi^0/\pi^\pm$ production ratio, and differences in selection efficiencies. Again, the ν_τ background uncertainties are related to cross section ratio uncertainties which are treated as 100% correlated among samples.

The far detector samples for the antineutrino beam mirror those described above for the neutrino beam samples. Additional constraints are expected to occur in a fit to both neutrino and antineutrino beam samples; variations in δ_{CP} induce opposite effects (in both shape and rate) in the ν_e and $\bar{\nu}_e$ samples, while most systematic uncertainties have a positively correlated effect. In the neutrino and antineutrino samples, NC background to the ν_μ and $\bar{\nu}_\mu$ samples is treated as correlated, as is NC and ν_μ CC background to the ν_e and $\bar{\nu}_e$ samples, because the dominant source of uncertainty is expected to be modeling of pion production. Signal and beam ν_e background normalization is treated as uncorrelated. The normalization for ν_τ CC background is treated as 100% correlated among all samples.

Energy-scale uncertainties in these samples, which can affect the shape of the reconstructed energy spectra, result from inaccurate models of detector response, missing energy in the hadronic systems (primarily from neutron production), and from final-state interactions (FSI). The dominant source of uncertainty is the hadronic energy scale, which is the same for both ν_e and ν_μ samples, so relative energy-scale uncertainties are limited to differences in kinematics between ν_μ and ν_e interactions and differences in detector response for muons and electrons, which will be highly constrained by test beam experiments. Systematic uncertainties stemming from the FSI model are different between the ν and $\bar{\nu}$ samples, which provides enough freedom in the three-flavor fit to potentially mimic the effect of a CP violation signal, thus degrading experimental sensitivity. However, the effect will be the same in the ν_e ($\bar{\nu}_e$) and ν_μ ($\bar{\nu}_\mu$) samples, allowing the relative ν_e to ν_μ ($\bar{\nu}_e$ to $\bar{\nu}_\mu$) energy scales to be fixed by comparing the energies of the appearance peak and the disappearance trough. Additional constraints on the FSI model will be required from ND analyses and external data.

3.6.2 Anticipating Uncertainties Based on Previous Experience

Table 3.8 shows the uncertainties in analyses of the ν_e appearance rate achieved by MINOS [29] and T2K [26] compared to the uncertainties anticipated in a similar DUNE analysis. The goals for normalization uncertainties represent the total expected uncertainty on an analysis of ν_e appearance rate in DUNE; the actual DUNE analysis will be based on a three-flavor spectral fit to all four far detector samples, so that the portions of these uncertainties that are correlated among far detector samples is expected to largely cancel. The portions of these uncertainties that are not correlated among samples and the effect of energy reconstruction on this analysis must be well understood. The goals for each source of systematic uncertainty are chosen by determining which of

the existing experiments is more representative of DUNE for that source of uncertainty and, based on that comparison, setting a reasonable goal for a next-generation experiment. The goals are based on expected capabilities of the high-resolution LArTPC far detector, precise measurements expected from a highly capable near detector, and well-understood analysis techniques developed in the existing generation of experiments. Explanations of the choices in Table 3.8 follow.

Table 3.8: Systematic uncertainties on the ν_e appearance signal rate prediction in MINOS and T2K and a projection of the anticipated uncertainties in DUNE. In each case, the quoted uncertainty is the effect on the ν_e appearance signal rate only. These uncertainties are the *total* expected uncertainties on the ν_e appearance signal rate; this includes both those uncertainties that are correlated and those that are uncorrelated in the three-flavor fit. For reference, the uncertainties assumed in the nominal DUNE sensitivity calculations are also provided.

Source of Uncertainty	MINOS ν_e	T2K ν_e	DUNE ν_e	Comments
Beam Flux after N/F extrapolation	0.3%	3.2%	2%	See "Flux Uncertainties" in Section 3.6.2
Interaction Model	2.7%	5.3%	$\sim 2\%$	See "Interaction Model Uncertainties" in Section 3.6.2
Energy scale (ν_μ)	3.5%	included above	(2%)	Included in 5% ν_μ sample normalization uncertainty in DUNE 3-flavor fit.
Energy scale (ν_e)	2.7%	2.5% includes all FD effects	2%	See "ν_e Energy-Scale Uncertainties" in Section 3.6.2
Fiducial volume	2.4%	1%	1%	Larger detectors = smaller uncertainty.
Total	5.7%	6.8%	3.6 %	
Used in DUNE Sensitivity Calculations			$5\% \oplus 2\%$	Residual ν_e uncertainty: 2%

Flux Uncertainties

DUNE plans to take advantage of spectral analysis, meaning that absolute and relative flux normalization is required. Since the MINOS ν_e appearance analysis is based on normalization only, in terms of the ν_e appearance analysis, DUNE will be more like T2K, which has achieved 3.2% normalization uncertainty on its ν_e sample from uncertainties in the flux. Additionally, the inclusive neutrino charged-current cross section measurement from the MINOS near detector reported in [30] has achieved a normalization uncertainty of $\sim 2\%$ in the range $3 < E_\nu < 9$ GeV and the near-to-far ν_μ unoscillated-spectrum extrapolation errors in MINOS are <3% without any independent constraints on hadron production or muon-flux measurements at the near site. Therefore, as DUNE is planned to have a highly capable near detector, beamline muon detectors, dedicated

hadronization measurements, and improved simulation of beam flux based on MINERνA [31] measurements in the NuMI beam, a goal uncertainty of 2% has been set on ν_e signal normalization from uncertainties in the flux determination. As described in Chapter 6 and summarized in Section 3.6.4, preliminary simulations of the fine-grained tracker ND suggest this is an appropriate goal, predicting a 2.5% uncertainty on the absolute flux and a 1–2% uncertainty on the flux shape from ND analyses.

Interaction Model Uncertainties

Interaction model uncertainties result from uncertainties in modeling neutrino interactions with the target nuclei in the near and far detectors. These uncertainties include ν_e and ν_μ cross section uncertainties, uncertainties from modeling the structure of the target nucleus, and the impact of hadronization model uncertainties in simulating the break up of the target nucleus in higher-energy inelastic interactions. DUNE will employ argon nuclear targets in both the near and far detectors, allowing for a larger cancellation of interaction model uncertainties than in T2K, in which the target nuclei in the near detector are carbon while those in the far detector are oxygen. Additionally, the angular resolution, vertex resolution, and particle identification capability of the DUNE near detector are expected to increase its ability to constrain those cross section uncertainties that are common between near and far detectors, but for which the T2K near detector could not provide significant constraint. DUNE's high-resolution near detector is expected to enable further constraints on hadronization uncertainties, relative to MINOS, by resolving many of the individual particles produced in the resonance and deep-inelastic scattering interactions, which represent the majority of the DUNE data sample. Finally, significant improvements to neutrino interaction models are anticipated as a result of the intermediate neutrino program [32], in which measurements will be made across a range of different nuclei and the resulting models will be tested on argon in LArTPCs. Therefore, 2% is taken as a goal for the effect of interaction model uncertainties on the DUNE ν_e signal normalization. It is important to note that this level of uncertainty depends upon the ability to isolate neutrino-argon interactions in the near detector to facilitate cancellation of near-far uncertainties; this is a requirement of the ND design.

Additionally, in considering the effect of the three-flavor analysis on the final uncertainty, the neutrino beams in DUNE and MINOS have energy spectra that peak around 2.5–3.0 GeV, compared to 600 MeV in T2K. The theoretical uncertainty on the ν_e/ν_μ cross section ratio is less than 1% above neutrino energies of 1.0–1.5 GeV [33], a factor of about three smaller than at T2K's median energy, so the uncertainty on the ν_e normalization with respect to the ν_μ spectrum in DUNE will be significantly improved compared to T2K. Uncertainty in the $\nu/\bar{\nu}$ cross section ratio is somewhat more difficult to quantify given the existing discrepancies between data and currently implemented models, though this is expected to improve as more complete models are introduced. As described in Section 3.6.4, preliminary studies with a Fast MC demonstrate the potential for significant cancellation of cross section uncertainties in the DUNE three-flavor analysis, even when uncertainties in the ν_e/ν_μ and $\nu/\bar{\nu}$ cross section ratios are as large as 20%.

Uncertainty from ν_e Energy Scale

MINOS and T2K have achieved uncertainty in the ν_e signal normalization from ν_e energy scale of 2.7% and 2.5% respectively, where the 2.5% from T2K actually includes most far detector effects. DUNE's LArTPC far detector is expected to outperform both the MINOS sampling calorimeter and the T2K water Cerenkov detector in reconstruction of ν_e interactions. Purity of the quasielastic-like event selection should be improved relative to T2K's by the capability of the LArTPC to detect hadronic showers that would be below threshold in SuperK, as described in [34]. For non-quasielastic-like events, the low thresholds and high resolution of the DUNE LArTPC will significantly improve calorimetric reconstruction over the MINOS sampling calorimeter. Significant experience with simulation, reconstruction, and calibration of neutrino interactions in LArTPCs is expected from the Intermediate Neutrino Program, particularly Fermilab's SBN program [35], which will include three LArTPCs: SBND [36], μBooNE [37], and ICARUS-T600 [38]. An active program of prototypes and test-beam measurements is planned to study the reconstruction of charged and neutral particles in LArTPCs; this suite of experiments includes the DUNE 35-t prototype LArIAT [39], CAPTAIN [40], and the CERN neutrino platform single phase prototypes. (The 35-t and CERN prototypes are discussed in the Prototyping Strategy chapter of Volume 4: *The DUNE Detectors at LBNF*.) Finally, an improved model of neutrino interactions will reduce the impact of imperfect reconstruction of energy from neutrons and low-momentum protons on the DUNE analysis. Therefore, a goal has been set of using the superior detector performance and the improvements in understanding of LArTPC energy response and neutrino interactions expected in the next five to ten years to reduce the normalization uncertainty from the ν_e energy scale to 2%.

In considering the effect of the three-flavor analysis on the final uncertainty, hadronic energy is expected to contribute more than half of the total energy deposit for many ν_e and ν_μ interactions in the DUNE far detector. Since the hadronic energy scale does not depend on neutrino flavor, the uncertainties on this portion of the LArTPC energy response are expected to largely cancel in the DUNE three-flavor analysis, up to kinematic differences in the ν_e and ν_μ samples. However, uncertainty in the ν_e and ν_μ energy scales will also reduce the sensitivity of the fit to spectral shape. The effect of one such uncertainty on experimental sensitivity is shown in Section 3.6.3, but the full impact of energy-scale uncertainty has not yet been explored. The fraction of the total energy carried by neutrons will be different between the ν and $\bar\nu$ samples both because of the different probabilities for neutrinos and antineutrinos to interact with protons and neutrons and because of differing kinematics. The contribution from neutrons will also be different between the ν_e and ν_μ samples because these samples peak at different energies due to oscillation effects. For this reason, understanding of both neutron production and detector response to neutrons will be important for constraining uncertainty in the three-sample fit. Deployment of the CAPTAIN detector in a neutron beam at LANL is planned to determine the response of a LArTPC to neutrons. With the neutron response well understood, measurements by CAPTAIN and other detectors in the intermediate neutrino program will be able to determine average neutron production rates, which will allow for appropriate corrections to the energy-scale bias at a statistical level.

Total Uncertainties Assigned to the Normalization Parameters

Based on the preceding considerations, the DUNE signal normalization uncertainty is taken to be $5\% \oplus 2\%$ in both neutrino and antineutrino mode, where 5% is the normalization uncertainty on the FD ν_μ sample and 2% is the effective uncorrelated uncertainty on the FD ν_e sample after fits to both near and far detector data and all external constraints. These signal normalization parameters are treated as 100% uncorrelated between neutrinos and antineutrinos. The normalization uncertainties on background to these samples and their respective correlations are given in Table 3.9. These assumptions for the non-oscillation systematic uncertainties are used to calculate the sensitivities presented in Section 3.2. The goal for the *total* uncertainty on the ν_e sample in DUNE is less than 4%, so the $5\% \oplus 2\%$ signal normalization uncertainty used for sensitivity calculations is appropriately conservative. Additionally, cancellation of the correlated portion of the uncertainty is expected in the four-sample fit, so the residual uncorrelated normalization uncertainty on the ν_e sample is expected to be reduced to the 1–2% level, such that the 2% residual normalization uncertainty used in the sensitivity calculations is also well-justified. Variations on these assumptions are explored in Section 3.6.3.

Table 3.9: Normalization uncertainties and correlations for background to the ν_e, $\bar{\nu}_e$, ν_μ, and $\bar{\nu}_\mu$ data samples

Background	Normalization Uncertainty	Correlations
For $\nu_e/\bar{\nu}_e$ appearance:		
Beam ν_e	5%	Uncorrelated in ν_e and $\bar{\nu}_e$ samples
NC	5%	Correlated in ν_e and $\bar{\nu}_e$ samples
ν_μ CC	5%	Correlated to NC
ν_τ CC	20%	Correlated in ν_e and $\bar{\nu}_e$ samples
For $\nu_\mu/\bar{\nu}_\mu$ disappearance:		
NC	5%	Uncorrelated to $\nu_e/\bar{\nu}_e$ NC background
ν_τ	20%	Correlated to $\nu_e/\bar{\nu}_e$ ν_τ background

3.6.3   Effect of Variation in Uncertainty

Figure 3.23 shows DUNE sensitivity to determination of neutrino mass hierarchy and discovery of CP violation as a function of exposure for several levels of signal normalization uncertainty. As seen in Figure 3.23, for early phases of DUNE with exposures less than $100 \text{ kt} \cdot \text{MW} \cdot \text{year}$, the experiment will be statistically limited. The impact of systematic uncertainty on the CP-violation sensitivity for large exposure is obvious in Figure 3.23; the ν_e signal normalization uncertainty must be understood at the level of $5\% \oplus 2\%$ in order to reach 5σ sensitivity for 75% of δ_{CP} values with exposures less than $\sim900 \text{ kt} \cdot \text{MW} \cdot \text{year}$ in the case of the Optimized Design. Specifically, the absolute normalization of the ν_μ sample must be known to $\sim5\%$ and the normalization of the ν_e sample, relative to the $\bar{\nu}_e$, ν_μ, and $\bar{\nu}_\mu$ samples after all constraints from external, near detector, and far detector data have been applied, must be determined at the few-percent level. This level of systematic uncertainty sets the capability and design requirements for all components of the experiment, including the beam design and the near and far detectors.
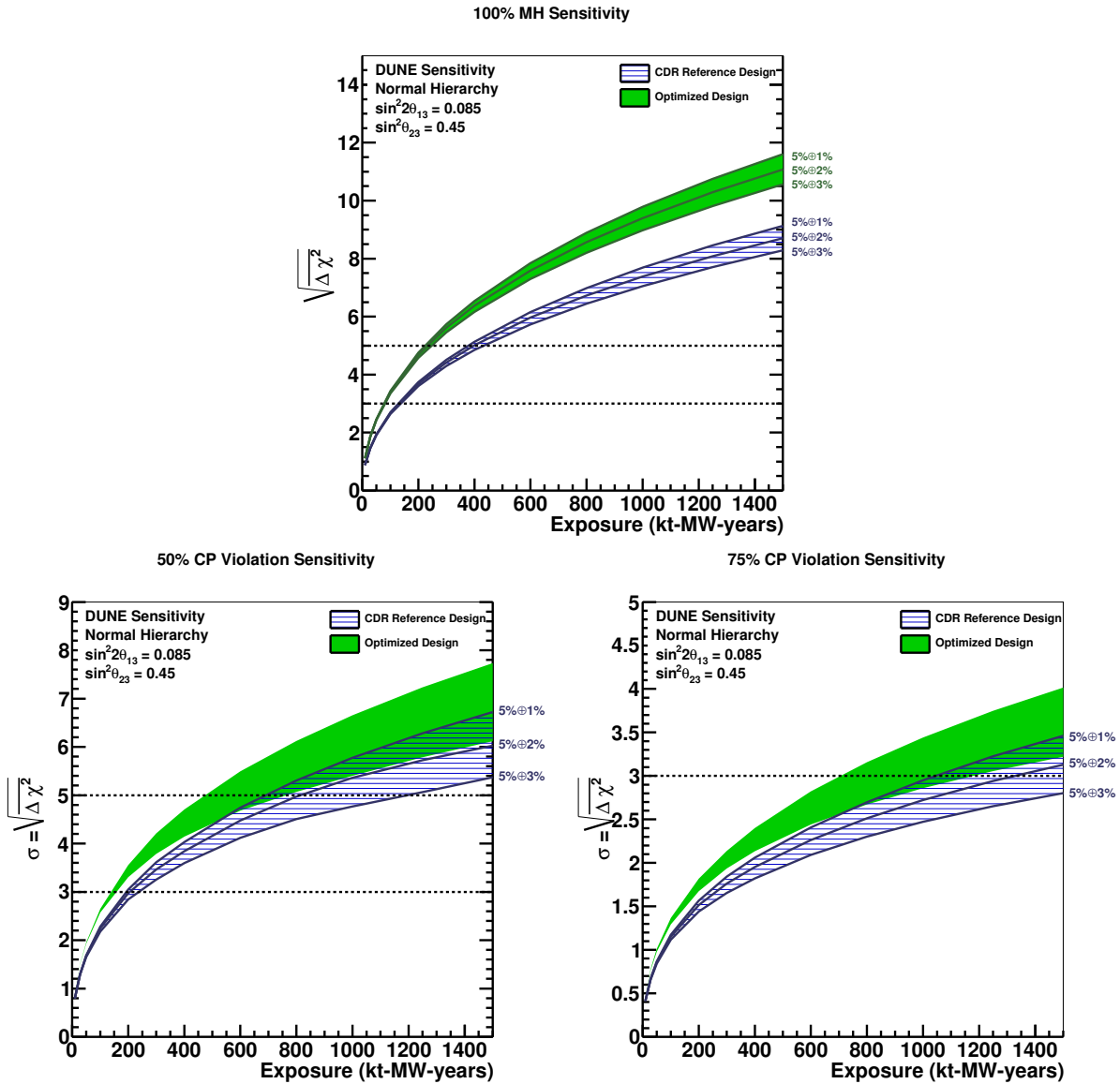
Figure 3.23: Expected sensitivity of DUNE to determination of the neutrino mass hierarchy (top) and discovery of CP violation, i.e., $\delta_{CP} \neq 0$ or π, (bottom) as a function of exposure in $kt \cdot MW \cdot year$, assuming equal running in neutrino and antineutrino mode, for a range of values for the ν_e and $\bar{\nu}_e$ signal normalization uncertainties from $5\% \oplus 3\%$ to $5\% \oplus 1\%$. The sensitivities quoted are the minimum sensitivity for 100% of δ_{CP} values in the case of mass hierarchy and 50% (bottom left) or 75% (bottom right) of δ_{CP} values in the case of CP violation. The two bands on each plot represent a range of potential beam designs: the blue hashed band is for the CDR Reference Design and the solid green band is for the Optimized Design. Sensitivities are for true normal hierarchy; neutrino mass hierarchy and θ_{23} octant are assumed to be unknown.

Signal and background normalization uncertainties remain relatively unimportant for the mass hierarchy measurement, even at large exposure, when considering minimum sensitivity for 100% of δ_{CP} values. This is because the minimum sensitivity occurs in the near-degenerate region where it is difficult to determine whether one is observing $\delta_{CP} = +\pi/2$ in the normal hierarchy or $\delta_{CP} = -\pi/2$ in the inverted hierarchy. Spectral analysis will help resolve this near-degeneracy, but is dependent on as-yet unexplored uncertainties in the spectral shape, which are expected to be dominated by energy-scale uncertainty. Figure 3.24 shows the impact on MH and CP-violation sensitivity of one possible energy-scale variation, in which energy bins are adjusted by N[E]→N[(1+a)E], while keeping the total number of events fixed. This is only one possible type of energy-scale uncertainty; more comprehensive study of energy-scale uncertainty is in progress and will be included in future analyses of experimental sensitivity.
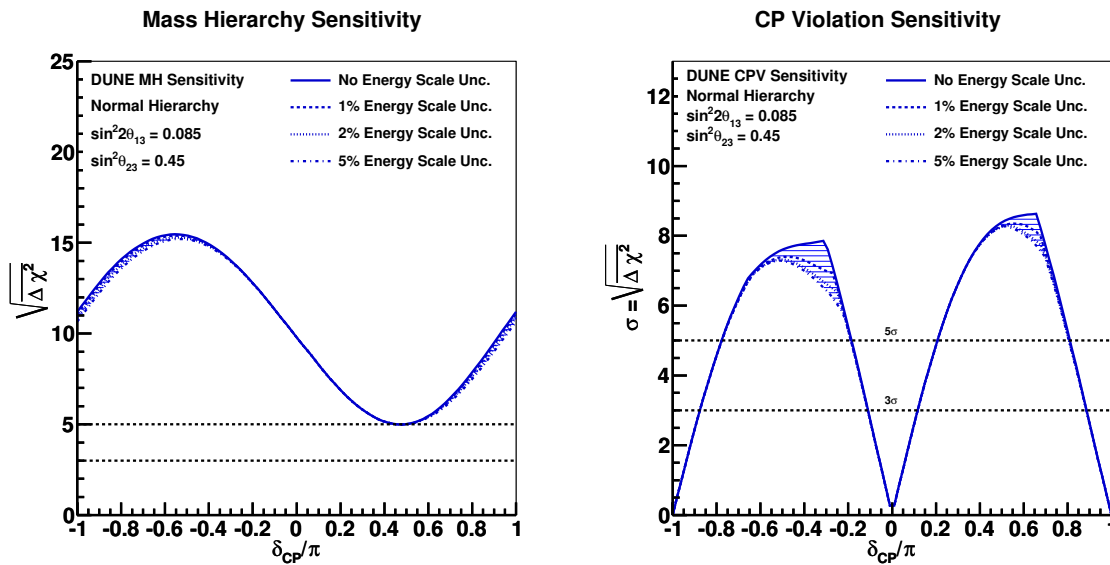
Figure 3.24: Expected sensitivity of DUNE to determination of the neutrino mass hierarchy (left) and discovery of CP violation, i.e. $\delta_{CP} \neq 0$ or π, (right) as a function of the true value of δ_{CP}, assuming equal running in neutrino and antineutrino mode, for a range of values assigned to the "a" parameter in the energy-scale variation described in the text. In the MH figure, the case with no energy-scale systematic provides a significance of at least $\sqrt{\Delta\chi^2} = 5$ for all values of δ_{CP}. In the CPV figure, the case with no energy-scale systematic provides a significance of at least 3σ for 75% of δ_{CP} values. (See Figures 3.8 and 3.14 for the possible range of exposures to achieve this level of significance.) Sensitivities are for true normal hierarchy; neutrino mass hierarchy and θ_{23} octant are assumed to be unknown.

3.6.4 Ongoing and Planned Studies of Systematic Uncertainty

Detailed evaluation of systematic uncertainties for DUNE is ongoing. In many cases plans for studies have been developed but have not yet been executed. In general, each systematic will be studied both by propagating its uncertainty to oscillation analyses to evaluate the resultant degradation of the sensitivity and by ensuring the considered variations give proper coverage, i.e., truly encapsulating the lack of knowledge of the processes/effects in question. Estimates of systematic uncertainty for the propagation studies will be varied between the constraints available

from current external knowledge and a range of projections for ND performance. In cases where systematic uncertainty is shown to degrade the oscillation parameter measurement sensitivities, the required constraints will become detector performance requirements. The details of these studies are beyond the scope of this document; however, conclusions from some initial studies and an overview of each source of systematic uncertainty is laid out in the remainder of this section.

Initial studies using a Near Detector Fast Monte Carlo with a parameterized detector response predict 3% statistical uncertainties on the absolute flux using fully leptonic neutrino interactions for which high-precision cross section predictions exist. Specifically, the statistical uncertainty is expected to be $\sim$3% for neutrino-electron scattering ($E_\nu < 5$ GeV) and inverse muon decay ($E_\nu > 11$ GeV). Relative normalization using the low-ν_0 method is expected to constrain the flux shape to 1–2%; this level of precision in the ν_μ flux was achieved by NOMAD[41, 42], enabled by its 0.2% uncertainty in the muon energy scale. This flux shape measurement will be made for both ν_e and ν_μ, therefore, in combination with measurements from hadron production experiments, it can determine the distribution of the parent mesons which will constrain the near/far flux ratio. Detailed discussion of the planned program of ND measurements is in Chapter 6 and [43, 19]. Studies using a multi-sample fit to constrain the flux with simulated DUNE near detector event samples show significant constraints on all flux uncertainties; the post-fit uncertainty in most flux bins for this preliminary fit is less than 5%, which is the uncorrelated ν_μ signal normalization uncertainty assumed by the sensitivity calculations.

The two main sources of uncertainty in the beam simulation come from variations in the beam optics, $\mathcal{O}(1\%)$, and uncertainties in the hadron production models, $\mathcal{O}(10\%)$. Beam optics variations have been studied in detail and are found to be easily constrained by the ND. Software tools that allow re-weighting of neutrinos based on their parent hadrons have been developed by MINERνA; work is progressing with them to implement these tools in the DUNE simulation to evaluate the impact of uncertainty in hadron production models. In the meantime, MINERνA has agreed to provide its flux covariance matrix that details the flux rate and shape uncertainties prior to ND constraints. This will be combined with DUNE simulations to project reasonable hadron-production uncertainties to ND and FD analyses. Ultimately these uncertainties will be constrained by near detector measurements and dedicated hadron-production measurements such as those at NA61/SHINE [44] will provide additional external constraints.

Primary interaction uncertainties are specific to each model, and each of the three major cross section components (quasi-elastic processes, resonance production, and deep inelastic scattering) contribute roughly equally to the ν_e and $\bar{\nu}_e$ appearance signal. In most cases, uncertainty in modeling primary interactions comes from the hadronic interaction part of the calculation, which includes form factors in the hadron tensor, the nuclear initial state, and FSI.

Coherent scattering: Coherent models built upon partially conserved axial current theory relate the neutrino scattering cross section to pion-nucleon or pion-nucleus scattering data [45][46]. The choice and characterization of that data can have large effects on the calculated cross section. Alternate "microscopic model" formulations are valid only over limited kinematic ranges and are not adequate to describe this process for DUNE [47][48]. Both types of model suffer from limited data constraints over a range of neutrino energy and nuclear targets. However, the low hadron thresholds and good angular resolution of the DUNE ND should be able to produce world-leading measurements and provide adequate constraints for this interaction channel and its relatively small

contribution to the overall cross section. Data from MINERνA [49], T2K, and upcoming LArTPC experiments will provide constraints for a variety of target nuclei over the relevant energy ranges required to constrain this sub-dominant process.

Quasi-elastic processes (QE): Models for this type of interaction require that the target nucleon is neither excited nor fragmented because the 4-momentum transfer to the hadronic system (Q^2) is low. For these low-Q^2 interactions, details of the nuclear initial state are important. However, current implementations of nuclear initial state models are inadequate, therefore the uncertainty in the only free parameter in the free-nucleon cross section model, M_A^{QE}, has been expanded to absorb the differences between simulations and ν-nucleus scattering data. Better models of the nuclear initial state have been developed and are currently being implemented in GENIE and other generators. These new models will be compared with current and future data from MINERνA, T2K and upcoming LArTPC experiments, and the effect of variations in M_A^{QE} on FD spectra will be compared to the effect of introducing the new models. Eventually the set of models that best agrees with data will be adopted in the DUNE simulations and the uncertainties assigned to these models will reflect the level of agreement with data.

Resonance production: There are two important sources of uncertainty in this model. The first is the uncertainty on the free-nucleon cross section due to unconstrained form factors and their use as effective parameters to absorb nuclear modeling effects. The second is the disagreement in outgoing pion kinematics between simulations and data. Data from T2K, MINERνA [50][51], upcoming LArTPC experiments, and the DUNE ND should provide good constraints for DUNE oscillation analyses, but model improvements will be required to help propagate these constraints to the FD signal and background predictions. Model improvements are needed for the principal interaction model, so-called "background" interactions where the pion is produced at the interaction vertex rather than through an intermediate Δ (or higher resonance), the interference between the two models, and the contributions to single-pion production from low-multiplicity DIS. Improved nuclear models are also required in order to estimate the impact of processes like pion-less delta decay and FSI. New models, which are available for some relevant regions of phase space, must be incorporated into generators and compared with data [52].

Deep inelastic scattering (DIS): The inclusive DIS cross section on iron has been very well constrained by data but individual final states have not. The primary source of uncertainty is in modeling the content and kinematics of the hadronic system as a function of its invariant mass. The resulting uncertainty on the DIS contribution to signal samples is relatively small, but it is nonetheless important to better constrain these models because the DIS contribution to background via pion production is significant. Data from MINERνA and upcoming LArTPC experiments should help to constrain the exclusive cross sections, as well as nuclear effects on the inclusive cross section [53]. Current studies are focused on building parameterized re-weighting functions for the hadronization model based on GENIE samples generated with 1σ changes to each relevant model parameter.

Nuclear models enter into the simulation of neutrino interactions both through modeling of initial-state interactions, i.e., interactions between the neutrino and the initial state of the nucleons and virtual particles within the nucleus, and modeling of final-state interactions (FSI), i.e., interactions of the particles exiting the primary interaction vertex with the nuclear medium.

Nuclear initial state: Uncertainties in initial-state interactions due to naive modeling of the environment of the nucleus have thus far been taken into account through inflation of the uncertainties on the free nucleon or quark interaction model. New models [54] are being added to generators and will soon be incorporated into the Fast MC to study how the impact on sensitivity of these models compares with uncertainties in the current nominal model. Data from upcoming LArTPC neutrino experiments will provide detailed information on nucleon production rates and kinematics, which will help to distinguish which of the new models best describes the data.

Final-state interactions: FSI can alter event reconstruction in two distinct ways. The first is a smearing of the total energy available to be deposited in the detector. The second is the misidentification of event topologies used to classify the neutrino flavor and interaction mode. Uncertainties in selection efficiencies and event-sample migrations due to intranuclear rescattering can be studied with existing DUNE tools. The predictions and uncertainties on GENIE's "hA" model [55] of intranuclear interaction are being tested against the detailed FSI model in the GiBUU [56] event generator. Studies of correlations among the free model parameters and and how variations in those parameters propagate differently for ν and $\bar{\nu}$ are also needed. Electron-argon scattering data [57] and studies of hadron production in upcoming LArTPC experiments are expected to further constrain the effects of FSI in argon nuclei.

A fit to Fast MC simulation of all four far detector samples (ν_e, $\bar{\nu}_e$, ν_μ, $\bar{\nu}_\mu$) significantly constrains cross section systematic uncertainty even in the case where many cross section parameters are allowed to vary simultaneously within their GENIE uncertainties. As seen in the example shown in Figure 3.25, a fit in which both $M_A^{QE,CC}$ and $M_A^{RES,CC}$ are allowed to vary within their GENIE uncertainties ($\pm 20\%$), which could significantly alter the energy distribution of the the selected events, results in a dramatic reduction in sensitivity if one considers only the ν_e appearance signal without constraint from the $\bar{\nu}_e$ and $\nu_\mu/\bar{\nu}_\mu$ samples. In contrast, for a four sample fit, this same parameter variation results in a smaller reduction in sensitivity to CP violation. This result includes a 10% uncertainty in the $\nu/\bar{\nu}$ cross section ratio and a 2.5% uncertainty in the ν_e/ν_μ cross section ratio; uncertainties in these ratios as large as 20% have been considered and did not produce dramatically different results. More details on this analysis are available in [58]. Preliminary studies also demonstrate significant constraint on cross section systematics from the near detector.

Uncertainty stemming from detector effects are somewhat more difficult to address with existing simulation efforts. Tools to evaluate the effect of uncertainty in single-particle resolutions, detection and particle-identification efficiencies, and energy scale are in development within the Fast MC framework. The results of these studies will provide performance requirements for the DUNE detectors, but more complete understanding of the expected size of these effects will require comparison between data and a full Monte Carlo. The status of efforts to develop reconstruction and analysis tools for a full Monte Carlo simulation of DUNE is described in the Software and Computing chapter of Volume 4: *The DUNE Detectors at LBNF*. At the same time, a number of test-beam and prototype experiments, including the DUNE 35-t prototype, LARIAT, CAPTAIN, and the CERN neutrino platform experiments, are being designed and built to reduce these uncertainties with experimental data. The status of some of these efforts is described in the Prototyping Strategy chapter of Volume 4: *The DUNE Detectors at LBNF*.

These ongoing studies to improve models of neutrino interactions in LArTPC detectors and to
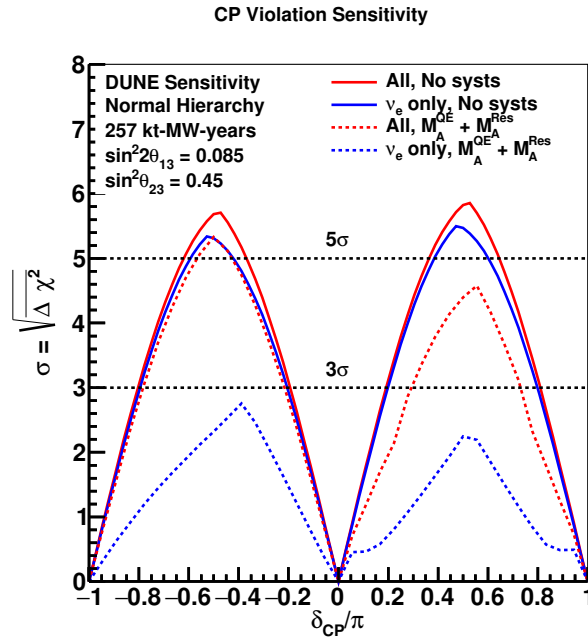
Figure 3.25:   An example CP violation sensitivity calculated using inputs from the FastMC in a fit to all four (ν_e, $\overline{\nu}_e$, ν_μ, $\overline{\nu}_\mu$) samples (red) and a fit to the ν_e appearance sample only (blue), for the case of no systematic uncertainty (solid) and the case in which both $M_A^{QE,CC}$ and $M_A^{RES,CC}$ are allowed to vary with a 1σ uncertainty of 20% (dashed). This example was taken from an earlier DUNE study, so the absolute sensitivity can not be compared with the DUNE sensitivities presented in this document.

evaluate the remaining uncertainties, by comparisons to data and alternate models, are considered high priority not only by the DUNE collaboration, but by the global neutrino community. It is reasonable to expect that model improvements and new data will provide DUNE with improved inputs and reduced uncertainties compared to current knowledge. Following the plan described in the preceding paragraphs, DUNE collaborators will actively participate in the global effort to improve understanding of neutrino interactions, will propagate what is learned in the intermediate neutrino program to DUNE analyses, and will evaluate the effect of remaining uncertainties on the DUNE analyses.

3.7   Optimization of the LBNF Beam Designs

The LBNF neutrino facility at Fermilab utilizes a conventional horn-focused neutrino beam produced from pion and kaon decay-in-flight. It will aim the neutrino beam toward the DUNE far detector located 1300 km away at the Sanford Underground Research Facility. The design of the LBNF neutrino beamline is a critical component for the success of DUNE. As demonstrated in earlier sections, the optimization of the beam design can have significant impact on the exposures needed to achieve the desired physics goals independent of additional improvements to the accelerator complex such as upgrades to 2.4 MW and improvements to uptime and efficiency, and reductions in systematic uncertainties. The reference beam design is described in detail in Volume 3: *The Long-Baseline Neutrino Facility for DUNE*. In this section a summary of the ongoing efforts

to optimize the beam focusing system and decay pipe geometry designs for the primary oscillation physics measurements is presented.

3.7.1 Reference Beam Design

The reference beam design is based on the designs of targets and focusing systems for NuMI. These designs are well understood and have proven track records of reliability and performance. The LBNF reference design includes a target similar to the one used for the low-energy tune of the NuMI beam [59], but with a larger thickness to accommodate the $1.2-$MW primary proton beam, and focusing horns essentially identical to those currently in operation in the NuMI beamline. The target consists of 47 graphite segments, for a total length of 95 cm including the space between segments, corresponding to two interaction lengths. The upstream face of the first segment is positioned 45 cm upstream of the first focusing horn to ensure sufficient clearance of the target's downstream end from the horn inner conductor. The separation of the upstream faces of the two horns has been decreased to 6.6 m, compared to the 10-m distance for the low-energy tune of the NuMI beam, to slightly enhance the neutrino flux at lower energies. A helium-filled decay pipe, 4 m in diameter and 204 m in length, provides the decay volume for the secondary pions to decay to muon neutrinos.

Neutrino fluxes for the reference beam are shown in Figure 3.26 for a $120-$GeV primary proton beam. Lowering the momentum of the primary proton beam increases right-sign neutrino flux at low energies and decreases wrong-sign contamination. Figure 3.27 shows current estimates of CP and mass hierarchy sensitivities versus proton momentum. It is estimated that these quantities improve very slightly as proton momentum decreases, until approximately 60 GeV, at which point the Main Injector cycle time becomes constant with proton momentum, causing beam power and physics sensitivities to drop sharply. Unless otherwise noted, results throughout this volume assume an $80-$GeV proton beam, corresponding to the optimal momentum whose technical feasibility has been thoroughly studied.

Another handle for tuning the neutrino energy spectrum of the reference beam is modification of the distance between the target and the first focusing horn. The expected fluxes for three different configurations are shown in Figure 3.28. The improvement in flux for each configuration with a longer decay pipe length of 250 m is also shown.

3.7.2 Improved Beam Options

There are several potential modifications to the reference beam design that would improve the experiment's sensitivity to the CP-violating phase and mass hierarchy. One option, which will be referred to as the *enhanced* reference beam, is based on the NuMI focusing horn design but uses a thinner and shorter cylindrical beryllium target positioned 25 cm upstream of the first focusing horn. We consider two decay pipe configurations for this enhanced reference beam, one 204 m long and 6 m in diameter and the other 250 m long and 4 m in diameter. The neutrino fluxes for these options, generated with an $80-$GeV primary proton beam, are shown in Figure 3.29.
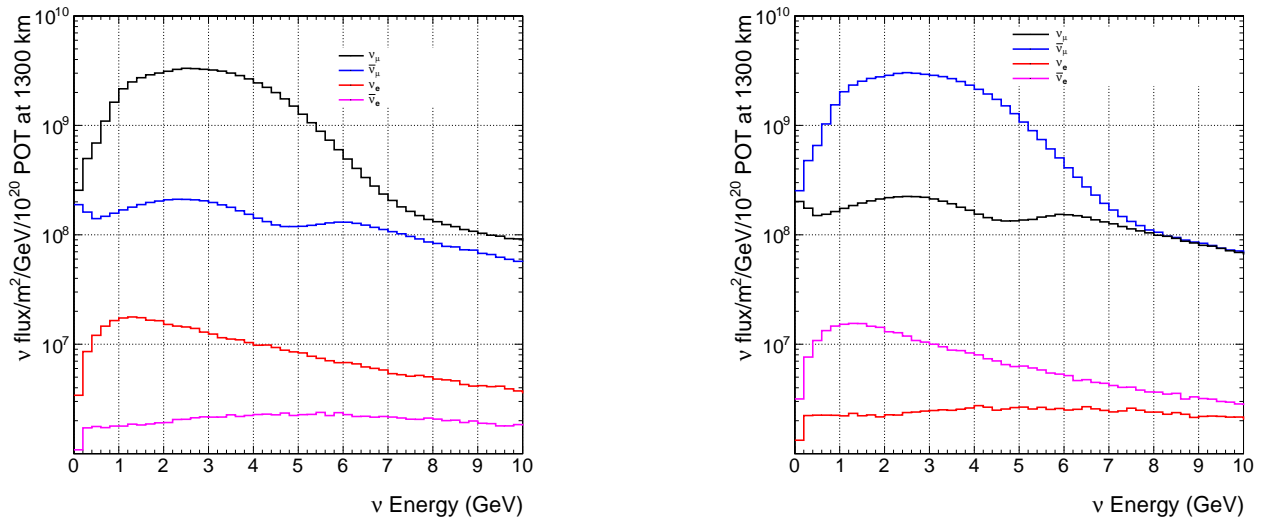
Figure 3.26: Neutrino fluxes for the reference focusing system operating in neutrino mode (left) and antineutrino mode (right), generated with a $120-$GeV primary proton beam.
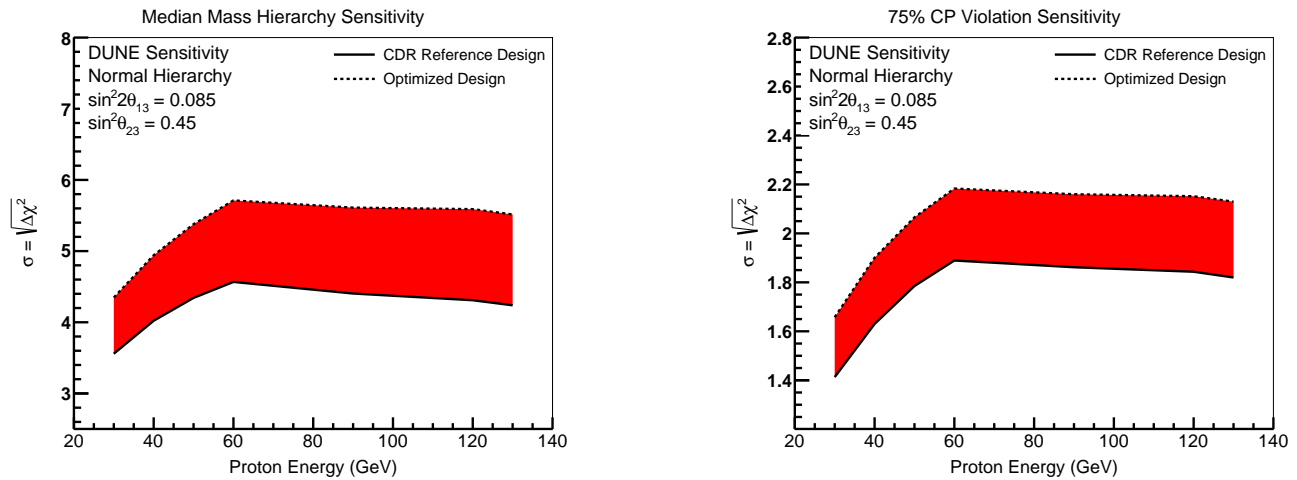
Figure 3.27: Minimum mass hierarchy sensitivity (left) and coverage of 75% of possible values of δ_{CP} (right) as a function of proton momentum assuming an exposure of 280 kt · year
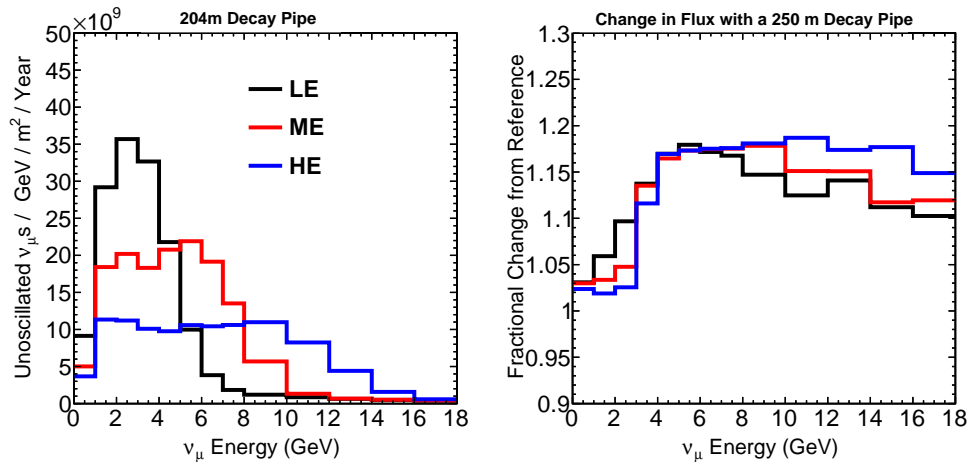
Figure 3.28: Neutrino fluxes for the reference beam design with 120−GeV protons, with the target starting 45 (LE), 135 (ME) and 250 (LE) cm upstream from the start of Horn 1 (left), and the fractional improvement in flux for the same beam configurations when the decay pipe is lengthened to 250 m (right).

The option offering the largest gains in sensitivity is a redesign of the focusing system, including target and horns, which would require a modification of the dimensions of the present target chase. To identify optimal designs, a genetic algorithm has been implemented to search for beam configurations that maximize sensitivity to CP violation. The procedure is inspired by a similar one developed by the LBNO collaboration [60], and considers 20 beamline parameters governing the primary proton momentum, target dimensions, and horn shapes, positions and current. Figure 3.30 shows the approximate shape and the 12 shape parameters (5 radial and 7 longitudinal dimensions) used for the optimization of the first focusing horn, while the second focusing horn is modeled as a NuMI-style horn, but allowed to rescale both in radial and longitudinal dimensions. The procedure yields horn size and shapes similar to those found by the LBNO collaboration. The first focusing horn is ∼5.5 m in length and ∼1.3 m in diameter. This optimized beam configuration includes a second focusing horn that is 32% longer and 7.8 m further downstream than that of the reference focusing design. This option would require an increase both in length, by ∼9 m, and in width, by ∼60 cm, of the target chase in the reference design. The increase in target chase length can be compensated by a reduction in decay pipe length, so that the total length of the combined chase and decay pipe remains the same as in the reference design. Figure 3.29 shows a comparison of fluxes for the reference, enhanced reference and optimized beam configurations. This optimized beam, with a decay pipe 195 m long and 4 m in diameter, produces a muon neutrino flux that is 20% greater than the nominal configuration at the first oscillation maximum (between 1.5 and 4 GeV), 53% greater at the second oscillation maximum (between 0.5 and 1.5 GeV), and reduces the antineutrino contamination of the beam. Sensitivity to δ_{CP} and the mass hierarchy as a function of the exposure for reference and alternative beam options are shown in Figure 3.31. The optimized beam leads to improvements in sensitivity to both mass hierarchy and CP violation. Refinement of the optimization procedure, including verification of the results with alternate hadron production models, and evaluation of the feasibility of the optimized designs are in progress.
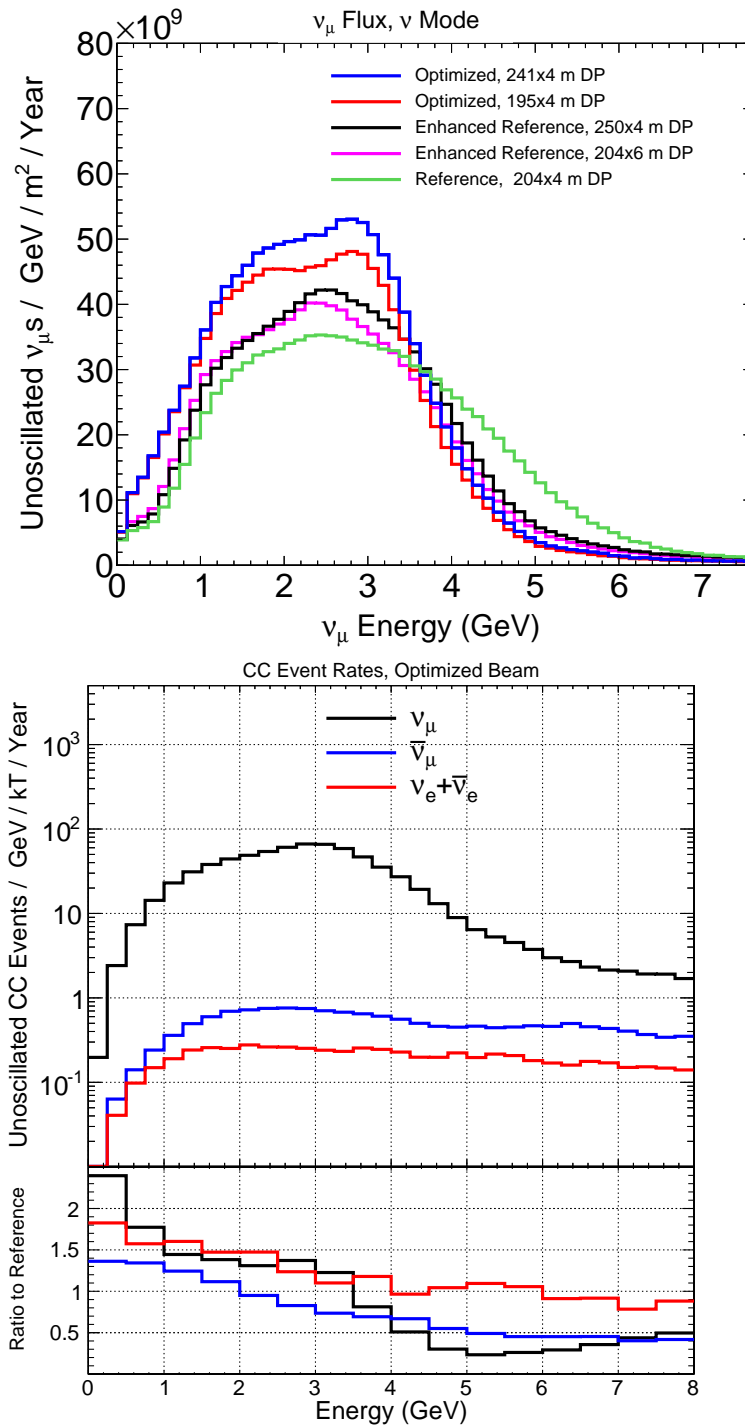
Figure 3.29: Neutrino mode muon neutrino fluxes for several beam designs, including the reference, the enhanced reference, and the optimized beam described in section 3.7.2 (top). The total CC interaction rate per year at 1300 km from the optimized focusing design with a 195−m decay pipe, and the ratio to the reference beam design (bottom). All beams use 80−GeV protons.
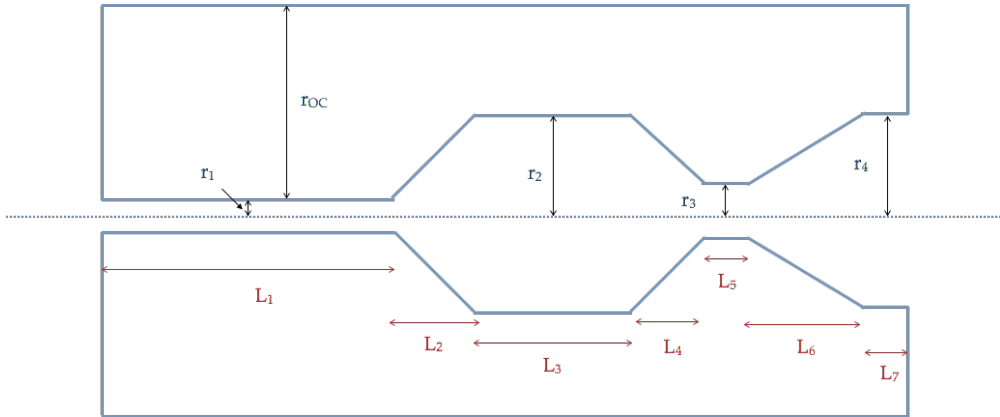
Figure 3.30: First focusing horn design considered in the alternative focusing optimization.
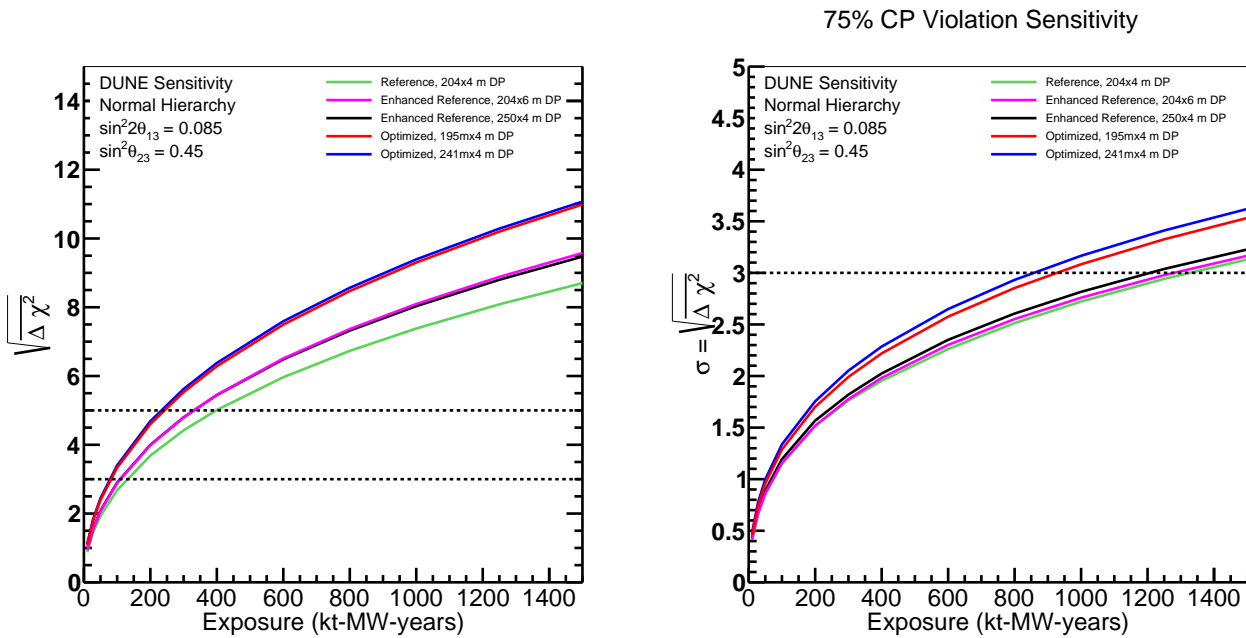
Figure 3.31: Sensitivity to the mass hierarchy (left) and δ_{CP} (right) as a function of exposure for the reference beam and the beam options discussed in Section 3.7.2. All beams use $80-$GeV protons.

3.8 Testing the Three-Flavor Paradigm and the Standard Model

Due to the very small masses and large mixing of neutrinos, their oscillations over a long distance act as an exquisitely precise interferometer with high sensitivity to very small perturbations caused by new physics phenomena, such as:

- nonstandard interactions in matter that manifest in long-baseline oscillations as deviations from the three-flavor mixing model

- new long-distance potentials arising from discrete symmetries that manifest as small perturbations on neutrino and antineutrino oscillations over a long baseline

- sterile neutrino states that mix with the three known active neutrino states

- large compactified extra dimensions from String Theory models that manifest through mixing between the Kaluza-Klein states and the three active neutrino states

- Lorentz and CPT violation due to an underlying Planck-scale theory that manifest through sidereal dependence on the neutrino oscillation probability

Full exploitation of DUNE's sensitivity to such new phenomena will require high-precision predictions of the unoscillated neutrino flux at the far detector and large exposures. Studies will be conducted to understand the limits that DUNE could impose relative to current limits and those expected from other experiments.

3.8.1 Search for Nonstandard Interactions

For $\nu_{\mu,e} \to \nu_{e,\mu}$ oscillations that occur as the neutrinos propagate through matter, the coherent forward scattering of ν_e's on electrons in matter modifies the energy and path-length dependence of the vacuum oscillation probability in a way that depends on the magnitude *and* sign of Δm_{31}^2. This is the Mikheyev-Smirnov-Wolfenstein (MSW) effect [61, 62]. NC nonstandard interactions (NSI) may be interpreted as nonstandard matter effects that are visible only in a far detector at a sufficiently long baseline. They can be parameterized as new contributions to the MSW matrix in the neutrino-propagation Hamiltonian [63, 64]:

$$H = U \begin{pmatrix} 0 & & \\ & \Delta m_{21}^2/2E & \\ & & \Delta m_{31}^2/2E \end{pmatrix} U^\dagger + \tilde{V}_{\text{MSW}} \,, \qquad (3.16)$$

with

$$\tilde{V}_{\text{MSW}} = \sqrt{2} G_F N_e \begin{pmatrix} 1 + \epsilon_{ee}^m & \epsilon_{e\mu}^m & \epsilon_{e\tau}^m \\ \epsilon_{e\mu}^{m*} & \epsilon_{\mu\mu}^m & \epsilon_{\mu\tau}^m \\ \epsilon_{e\tau}^{m*} & \epsilon_{\mu\tau}^{m*} & \epsilon_{\tau\tau}^m \end{pmatrix} \qquad (3.17)$$

Here, U is the leptonic mixing matrix, and the ϵ parameters give the magnitude of the NSI relative to standard weak interactions. For new physics scales of a few hundred GeV, a value of $|\epsilon| \leq 0.01$ is expected [65, 66, 67, 68, 69]. DUNE's $1300-$km baseline provides an advantage in the detection of NSI relative to existing beam-based experiments with shorter baselines. Only atmospheric-neutrino experiments have longer baselines, but the sensitivity of these experiments to NSI is limited by systematic effects. See [19] for potential sensitivities to these parameters at a $1300-$km baseline.

3.8.2 Search for Long-Range Interactions

The small scale of neutrino-mass differences implies that minute differences in the interactions of neutrinos and antineutrinos with currently unknown particles or forces may be detected through perturbations to the time evolution of the flavor eigenstates. The longer the experimental baseline, the higher the sensitivity to a new long-distance potential acting on neutrinos. For example, some of the models for such long-range interactions (LRI) as described in [70] could contain discrete symmetries that stabilize the proton and give rise to a dark-matter candidate particle, thus providing new connections between neutrino, proton decay and dark matter experiments. The longer baseline of DUNE improves the sensitivity to LRI beyond that possible with the current generation of long-baseline neutrino experiments. The sensitivity will be determined by the amount of $\nu_\mu/\bar{\nu}_\mu$-CC statistics accumulated and the accuracy with which the unoscillated and oscillated ν_μ spectra can be determined.

3.8.3 Search for Mixing between Active and Sterile Neutrinos

Several recent anomalous experimental results count among their possible interpretations phenomena that do not fit in the three-flavor mixing model [71, 72, 73, 74, 75], and searches for evidence of one or more sterile neutrino states are ongoing.

At DUNE, searches for active-sterile neutrino mixing can be conducted by examining the NC event rate at the far detector and comparing it to a precise estimate of the expected rate extrapolated from ν_μ flux measurements from the near detector and from beam and detector simulations. Observed deficits in the NC rate could be evidence for mixing between the active neutrino states and unknown sterile neutrino states. The most recent such search in a long-baseline experiment was conducted by the MINOS experiment [28, 76]. DUNE will provide a unique opportunity to revisit this search over a large range of neutrino energies and a longer baseline. The large detector mass and high beam power will allow a high-statistics sample of NC interactions to be collected. The high-resolution LArTPC far detector will enable a coarse measurement of the incoming neutrino energy in a NC interaction by using the event topology and correcting for the missing energy of the invisible neutrino. Both the energy spectrum and the rate of NC interactions will be measured with high precision at both near and far detectors.

Long-baseline experiments are sensitive to sterile neutrinos not only through NC measurements but also via appearance searches. In particular, as recently shown in [77], long-baseline appearance searches are the sole ones that are sensitive to the additional CP-violating phases that appear in

a framework with more than three neutrinos. In the event of a discovery of sterile neutrino states, long-baseline experiments — and DUNE in particular — will have a unique role in completing the picture of the new enlarged framework, because short-baseline experiments have almost no sensitivity to these additional CP-violating phases. It has been shown that T2K already provides some information on one such phase [77], and the sensitivity has been studied for LBNE [78].

3.8.4 Search for Large Extra Dimensions

Several theoretical models propose that right-handed neutrinos propagate in large compactified extra dimensions, whereas the standard left-handed neutrinos are confined to the four-dimensional brane [79]. Mixing between the right-handed *Kaluza-Klein* modes and the standard neutrinos would change the mixing patterns predicted by the three-flavor model. The effects could manifest, for example, as distortions in the disappearance spectrum of ν_μ. The rich oscillation structure visible in DUNE, measured with its high-resolution detector using both beam and atmospheric oscillations, could provide further opportunities to probe for this type of new physics.

3.8.5 Search for Lorentz and CPT Violation

Lorentz invariance and its associated CPT symmetry are foundational aspects of the Standard Model. However, the Standard Model is thought to be a low-energy limit of a more fundamental theory that unifies quantum physics with gravity at the Planck scale. As a result, an underlying theory can induce violations of Lorentz invariance and violations of CPT symmetry that can generate experimentally observable signals of Planck-scale physics. The Standard-Model Extension (SME) [80, 81, 82] is an effective field theory that contains the Standard Model, general relativity, and all possible operators that break Lorentz symmetry. (Since CPT violation implies Lorentz violation, the SME necessarily includes operators that break CPT symmetry.) Within the SME framework, the probability for neutrino oscillations depends on the direction of neutrino propagation within a Sun-centered inertial frame [83, 84]. For a long-baseline experiment with both the neutrino beam source and detector fixed to the surface of the Earth, the Earth's rotation causes the direction of neutrino propagation to change with sidereal time. The SME theory thus predicts a sidereal dependence of the observed beam neutrino rate. DUNE has the potential to perform studies that explore regimes never previously investigated and to improve existing sensitivities obtained in other neutrino experiments. For example, the baseline of 1300 km offers an advantage because the sensitivity to Lorentz and CPT violation grows linearly with the baseline. The beam orientation for DUNE is different from other experiments such as MINOS or T2K, so the combinations of coefficients for Lorentz and CPT violation appearing in the DUNE mixing probabilities are distinct. Additionally, the wide range of energy for the beam neutrinos and the ability to investigate both neutrino and antineutrino channels are advantageous.

3.9 Experimental Requirements

The technical designs of LBNF and the DUNE detectors must fulfill the scientific objectives described in Chapter 2. The following is a summary of the high-level scientific requirements for the neutrino oscillation physics. Details of the scientific and technical requirements for LBNF/DUNE deriving from the scientific objectives can be found in reference [85].

3.9.1 Neutrino Beam Requirements

LBNF must be designed for approximately twenty years of operation, in order to provide adequate exposure for the DUNE experiment. During its lifetime, the facility must be able to accommodate various target and focusing configurations to enable tuning of the neutrino energy spectrum, and must be suitable for upgraded targets and horns as technology improves and the primary proton beam power increases. Such flexibility is an essential requirement for a facility that will operate over multiple decades. The energy range of the neutrino beam must be adaptable, in order to address new questions in neutrino physics that may come up during such a long period.

The DUNE experiment requires that the LBNF facility provides a neutrino beamline and the conventional facilities to support it. The global science requirements on the LBNF beamline are as follows:

- The neutrino beam spectrum shall cover the energy region of the first two oscillation maxima affected by muon-neutrino conversion from the atmospheric parameters. For a baseline of 1300 km, with the current knowledge of parameters, the first two nodes are expected to be approximately 2.4 and 0.8 GeV. The matter effects dominate over the CP effects above 3 GeV and the CP effect dominates below 1.5 GeV. Adequate number of electron neutrino events with good energy resolution will allow DUNE to exploit this spectral information to determine mass hierarchy, CP phase, and a precise value of θ_{13} unambiguously. The beam spectrum will also allow muon disappearance measurement with two nodes.

- The beam shall be sign-selected to provide separate neutrino and antineutrino beams with high purity to enable measurement of CP violation mass hierarchy, and precision oscillation measurement.

- The electron neutrino content in the beam shall be kept small so that the systematic errors on the additional background have a small impact on the CP phase measurement (compared to the statistical error).

- The neutrino beam spectrum shall extend beyond the first maximum to higher energies, while maintaining a high signal-to-background ratio to obtain the maximum number of charged-current signal events. This will allow precision probes of the PMNS parameters that govern neutrino oscillations.

- The beam shall be aimed at the far detector with an angular accuracy that allows the deter-

mination of the far detector spectrum using the near detector measurements. The angular accuracy shall not be the dominant factor in the determination of oscillation parameters.

- The beam shall be capable of operating with a single-turn, fast-extracted primary proton beam from the Main Injector with greater than 2 MW of power. The fast extraction enables short spills which are essential for good cosmic ray background rejection for detectors.

- The beamline shall be able to accept a range of Main Injector proton energies that is well matched to the oscillation physics requirements. Proton beam energies of around 60 GeV are optimal for measurement simultaneous measurements of CP violation and MH, while higher energy beams (the maximum possible from the Main Injector is 150 GeV) can probe physics beyond the 3-flavor mixing, and probe ν_τ appearance with higher statistics. The power and protons-on-target available from the MI as a function of proton beam energy is summarized in Table 3.1.

3.9.2   Far Detector Requirements

The DUNE Far Detector (FD) requirements relevant to long-baseline neutrino oscillation physics include:

- Identification of Electron Neutrino and Antineutrino Events: The FD shall be capable of identifying electron neutrino and antineutrino charged current beam events in sufficient numbers within the fiducial volume of the detector to enable precision measurements of the parameters that govern $\nu_\mu \to \nu_e$ oscillations. The neutrino flavor of the event will be identified by clearly identifying the primary final state charged electron. The total energy of the charged current event shall be measured.

- Muon Neutrino and Antineutrino Events: The FD shall be capable of identifying muon neutrino and antineutrino charged current beam events in sufficient numbers within the fiducial volume of the detector and identify the primary muon particle emerging from the main event vertex. The total energy of the charged current event shall be measured.

- Multiple tracks and Electromagnetic Showers: The FD shall be capable of identifying events with multiple electromagnetic showers and non-showering particles produced within the fiducial volume of the detector.

- Baseline Length: A baseline of sufficient length shall be established between the neutrino beam facility and a far detector facility so that the difference between muon to electron neutrino conversion for the two cases of neutrino mass ordering can be clearly separated from the variation due to the CP phase, leading to unique determination of the CP phase.

- Cosmic Ray Shielding: The FD shall be located at a depth to reduce the number of in-time (within the beam spill time) cosmic ray background so that it does not contribute more than 1% of the final beam neutrino sample.

- CP Phase Measurement: The total number of observed electron-neutrino and electron-antineutrino type events – including consideration of background – shall be sufficient to measure the CP phase to better than 3σ at the maximum CP violation.

- Time Accuracy: Individual event times shall be measured with sufficient time accuracy to allow correlation of event times between detectors that are geographically separated. In the case of long-baseline oscillations, this would include correlation between the DUNE near and far detectors.

3.9.3 Near Detector Requirements

The DUNE Near Detector (ND) requirements relevant to long-baseline neutrino oscillation physics include:

- FD measurements not limited by ND: ND measurements shall be of sufficient precision to ensure that when extrapolated to FD to predict the FD event spectra without oscillations, the associated systematic error must be significantly less than the statistical error over the lifetime of the experiment.

- Muon Neutrino and Antineutrino Flux measurements: The ND shall measure the absolute and relative muon neutrino and antineutrino spectra separately. See Sections 3.6.2 3.6.4 for discussions of the required flux uncertainty and current studies.

- Electron Neutrino and Antineutrino Flux measurements: The ND shall measure the electron-neutrino and antineutrino contamination spectra of the beam separately in order to render the CP measurement as precise as possible.

- Background Measurements: The ND shall measure rates, kinematic distributions and detailed topologies of physics processes that could mimic signal events in the FD nuclear targets. This measurement shall be made with sufficient resolution to allow FD background calculation with precision that does not limit the oscillation measurements.

- Cross section measurements I: The ND will measure CC and NC differential cross sections separately as a function of energy.

- Cross section measurements II: The ND shall characterize various exclusive and semi-exclusive processes such as quasi-elastic interactions, resonance production, deep inelastic scattering, and neutrino-electron and neutrino-proton elastic scattering.

- Cross section measurements III: The ND shall measure the neutrino nucleus cross section off various targets like Hydrogen, Ar, Fe, Ca, and C.

Chapter 4

Nucleon Decay and Atmospheric Neutrinos

4.1 Nucleon Decay

4.1.1 Physics Motivation

Grand Unified Theories (GUTs) unite the three gauge interactions of particle physics – strong, weak, and electromagnetic – into one single force, and as a consequence, make predictions about baryon number violation and proton lifetime that may be within reach of DUNE. The theoretical motivation for the study of proton decay has a long and distinguished history [86, 87, 88] and has been reviewed many times [89, 90, 91]. Early GUTs provided the original motivation for proton-decay searches in kiloton-scale detectors placed deep underground to limit backgrounds [92]. The $22.5-$kt Super–Kamiokande experiment extended the search for proton decay by more than an order of magnitude relative to the previous generation of experiments. Contemporary reviews [93, 94, 95] discuss the strict limits already set by Super–Kamiokande and the context of the proposed next generation of larger underground experiments such as Hyper-Kamiokande and DUNE.

Although no evidence for proton decay has been detected, lifetime limits from the current generation of experiments already constrain the construction of many contemporary GUT models. In some cases, these limits are approaching the upper bounds of what these models will allow. This situation points naturally toward continuing the search with new, highly capable underground detectors, especially those with improved sensitivity to specific proton decay modes favored by GUT models. In particular, the exquisite imaging, particle identification and calorimetric response of the DUNE LArTPC Far Detector opens the possibility of obtaining evidence for nucleon decay on the basis of a single well reconstructed event.
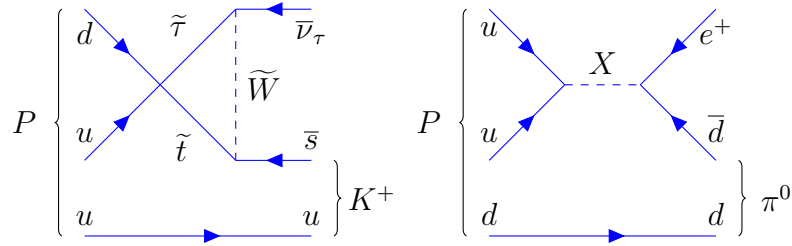
Figure 4.1: Feynman diagrams for proton decay modes from supersymmetric GUT, $p^+ \rightarrow K^+\overline{\nu}$ (left) and gauge-mediation GUT models, $p^+ \rightarrow e^+\pi^0$ (right).

4.1.2   Proton Decay Modes

The strength of the DUNE experiment is particularly evident in its capabilities to detect two prominent decay modes, shown in Figure 4.1. The decay $p \rightarrow e^+\pi^0$ arises from gauge mediation and is often predicted to have the higher branching fraction. In this mode, the total mass of the proton is converted into the electromagnetic shower energy of the positron and two photons from π^0 decay, with a net momentum vector near zero. This channel is demonstrably the more straightforward experimental signature for a water Cherenkov detector.

The second key mode is $p \rightarrow K^+\overline{\nu}$. This mode is dominant in most supersymmetric GUTs, many of which also favor other modes involving kaons in the final state. Among the modes with a *charged* kaon in the final state, $p \rightarrow K^+\overline{\nu}$ is uniquely interesting for DUNE: since stopping kaons have a higher ionization density than lower-mass particles, an LArTPC could identify the K^+ track with high efficiency. In addition, many final states of K^+ decay would be fully reconstructible in an LArTPC.

Although significant attention will be focused on the above benchmark modes, the nucleon decay program at DUNE will be a broad effort. Many other allowed modes of proton or bound neutron into antilepton plus meson that also conserve $B - L$ have been identified. And other modes that conserve $B + L$, or that decay only into leptons, have been hypothesized. In addition to nucleon decay, another promising way of probing baryon number violation in DUNE is through the search for the spontaneous conversion of neutrons into antineutrons in the nuclear environment. While these are less well motivated theoretically, opportunistic experimental searches cost little and could have a large payoff.

Figure 4.2 shows a comparison of experimental limits on key decay modes to the ranges of lifetimes predicted by an assortment of GUTs. The limits are dominated by recent results from Super–Kamiokande.

From this figure it is clear that an experiment such as DUNE with sensitivity to proton lifetimes between 10^{33} and 10^{35} years will probe a large number of GUT models, and thus will present a compelling opportunity for discovery. Even if no proton decay is detected, stringent lifetime limits will constrain the models: minimal SU(5) was ruled out by the early work of IMB and Kamiokande, and minimal SUSY SU(5) is considered to be ruled out by Super–Kamiokande. In most cases, another order of magnitude in improved limits will not rule out specific models but will constrain their allowed parameters; this could allow identification of less favored models that would require
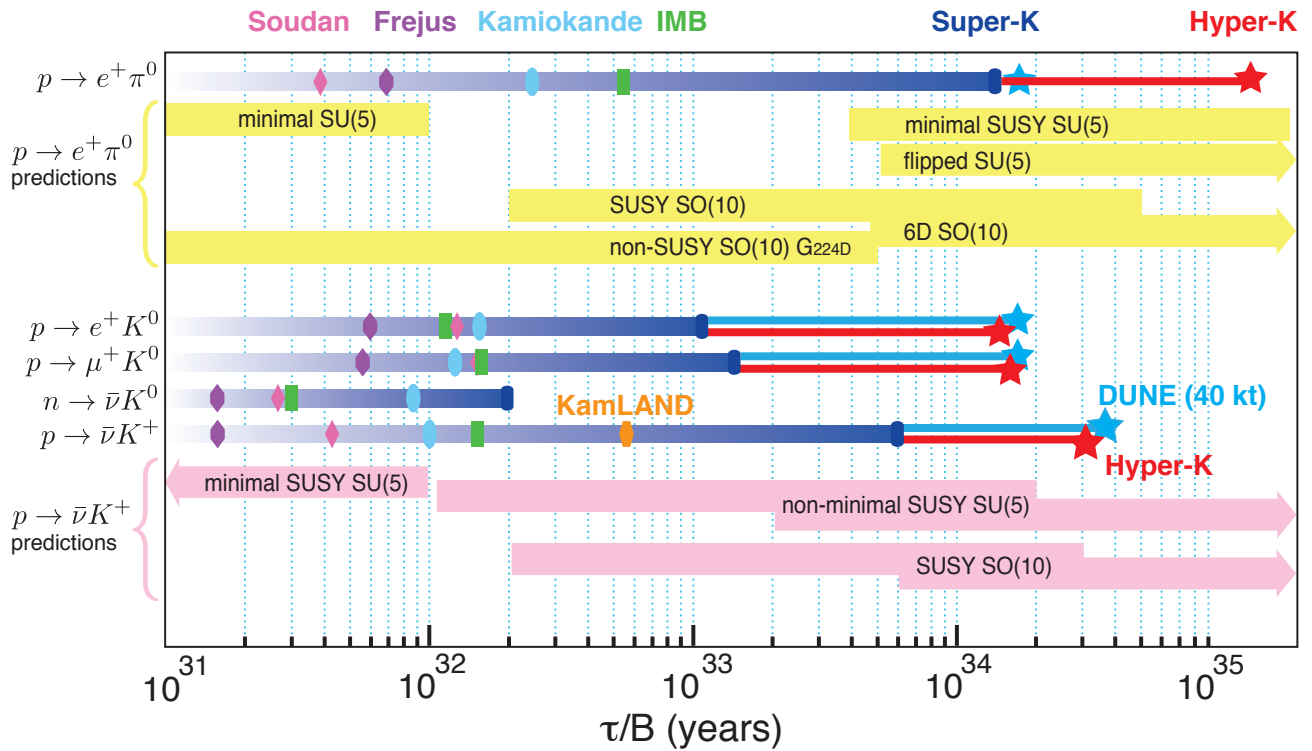
Figure 4.2: Current nucleon decay lifetime limits [24, 96] (90% C.L.) compared with ranges predicted by Grand Unified Theories. The upper section is for $p \to e^+\pi^0$, most commonly caused by gauge mediation. The lower section is for SUSY-motivated models, which commonly predict decay modes with kaons in the final state. Marker symbols other than stars indicate published experimental limits, as labeled by the colors on top of the figure. The stars represent projected limits for several recently proposed future experiments, calculated based on Poisson statistics including background, assuming that detected event yields equal the expected background.

fine-tuning in order to accommodate the data.

It is also clear from Figure 4.2 that it will not be easy for a LArTPC-based detector to make significant inroads on the $p \to e^+\pi^0$ channel, where background-free high-efficiency searches are possible with large water Cherenkov detectors at a lower cost per kt. For this reason, the focus of the remaining discussion is on the channels with kaons, in particular $p \to K^+\bar{\nu}$. However, it is important to note that the full-scale DUNE far detector would be able to provide confirming evidence for $p \to e^+\pi^0$ should a signal for this channel start to develop in the next-generation water detector at the few-times-10^{34}-year level.

4.1.3   Signatures for Nucleon Decay in DUNE

Extensive surveys [97, 98] of nucleon decay efficiency and background rates for large LArTPCs with various depth/overburden conditions provide the starting point for the assessment of DUNE's capabilities. Table 4.1 lists selected modes where LArTPC technology exhibits a significant performance advantage (per kt) over the water Cherenkov technology. This section focuses on the capabilities of DUNE for the $p \to K^+\bar{\nu}$ channel, which is seen as the most promising from theoretical and experimental considerations. Much of the discussion that follows can be applied to the other channels with kaons listed in the table.

Table 4.1: Efficiencies and background rates (events per Mt · year) for nucleon decay channels of interest for a large underground LArTPC [97], and comparison with water Cherenkov detector capabilities. The entries for the water Cherenkov capabilities are based on experience with the Super–Kamiokande detector [99].

Decay Mode	Water Cherenkov		Liquid Argon TPC	
	Efficiency	Background	Efficiency	Background
$p \to K^+\bar{\nu}$	19%	4	97%	1
$p \to K^0\mu^+$	10%	8	47%	< 2
$p \to K^+\mu^-\pi^+$			97%	1
$n \to K^+e^-$	10%	3	96%	< 2
$n \to e^+\pi^-$	19%	2	44%	0.8

The key signature for $p \to K^+\bar{\nu}$ is the presence of an isolated charged kaon (which would also be monochromatic for the case of free protons, with $p =340\,\mathrm{MeV}/c$). Unlike the case of $p \to e^+\pi^0$, where the maximum detection efficiency is limited to 40–45% because of inelastic intranuclear scattering of the π^0, the kaon in $p \to K^+\bar{\nu}$ emerges intact (because the kaon momentum is below threshold for inelastic reactions) from the nuclear environment of the decaying proton $\sim 97\%$ of the time. Nuclear effects come into play in other ways, however: the kaon momentum is smeared by the proton's Fermi motion and shifted downward by re-scattering [100].

In LArTPC detectors, the K^+ can be tracked, its momentum measured by range, and its identity positively resolved via detailed analysis of its energy-loss profile. This is in sharp contrast with water detectors, in which the K^+ momentum is below Cherenkov threshold. Additionally, all decay

modes can be cleanly reconstructed and identified in an LArTPC, including those with neutrinos, since the decaying proton is nearly at rest. With this level of detail, it is possible for a single event to provide overwhelming evidence for the appearance of an isolated kaon of the right momentum originating from a point within the fiducial volume. The strength of this signature is clear from cosmogenic-induced kaons observed by the ICARUS Collaboration in the cosmic-ray (CR) test run of half of the T600 detector, performed at a surface installation in Pavia [101] and in high-energy neutrino interactions with the full T600 in the recent CNGS (CERN Neutrinos to Gran Sasso) run [102]. Figure 4.3 shows a sample event from the CNGS run in which the kaon is observed as a progressively heavily ionizing track that crosses into the active liquid argon volume, stops, and decays to $\mu\nu$, producing a muon track that also stops and decays such that the Michel-electron track is also visible.

References [19, 98, 103] present detailed examinations of possible backgrounds, including those arising from cosmic ray interactions in the detector and surrounding rock, atmospheric neutrino interactions in the detector, and reconstruction failures. Table 4.2 summarizes the results of those background studies. All together, our estimate of total background events in the $p \to K^+\overline{\nu}$ sample is less than 1 per $\mathrm{Mt} \cdot \mathrm{year}$.

Table 4.2: Background sources and mitigation strategies for the $p \to K^+\overline{\nu}$ search in DUNE

Background Source	Mitigation Strategy
Internal cosmic ray spallation	Energy threshold
External cosmogenic K^+ production	Depth, fiducialization
External cosmogenic K^0 production +internal charge-exchange to K^+	Cuts on other secondaries
Atmospheric ν $\Delta S = 0$ processes	Cut on associated strange baryon
Atmospheric ν $\Delta S = 1$ processes	Cabibbo-suppressed, lepton ID
Atmospheric ν with π mis-ID	dE/dx discrimination, 236 MeV muon track
Reconstruction pathologies	dE/dx profiles vs track length

4.1.4 Summary of Expected Sensitivity to Key Nucleon Decay Modes

Based on the expected signal efficiency and upper limits on the background rates, the expected limit on the proton lifetime as a function of running time in DUNE for $p \to K^+\overline{\nu}$ is shown in Figure 4.4.

The current limits on the $p \to \overline{\nu}K^+$ were set by Super–Kamiokande. This figure demonstrates that improving these limits significantly beyond that experiment's sensitivity would require a LArTPC
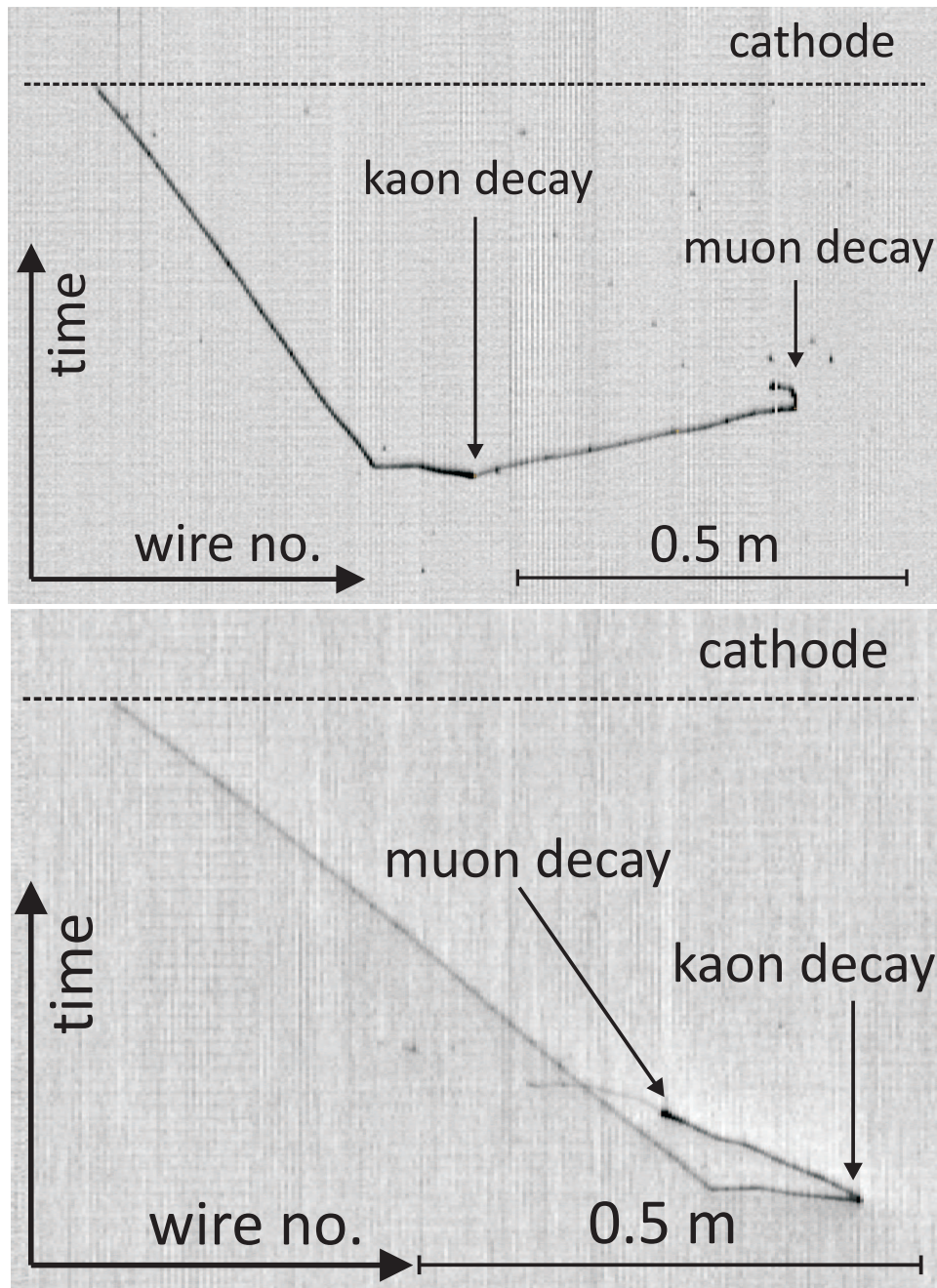
Figure 4.3: Event display for a decaying kaon candidate $K \to \mu\nu_\mu$ $\mu \to e\nu_e\nu_\mu$ in the ICARUS T600 detector observed in the CNGS data (K: 90 cm, 325 MeV; μ : 54 cm, 147 MeV; e : 13 cm, 27 MeV). The top figure shows the signal on the collection plane, and the bottom figure shows the signal on the second induction plane [102].

detector of at least 10 kt, installed deep underground. A 40−kt detector will improve the current limits by an order of magnitude after running for two decades. Clearly a larger detector mass would improve the limits even more in that span of time.
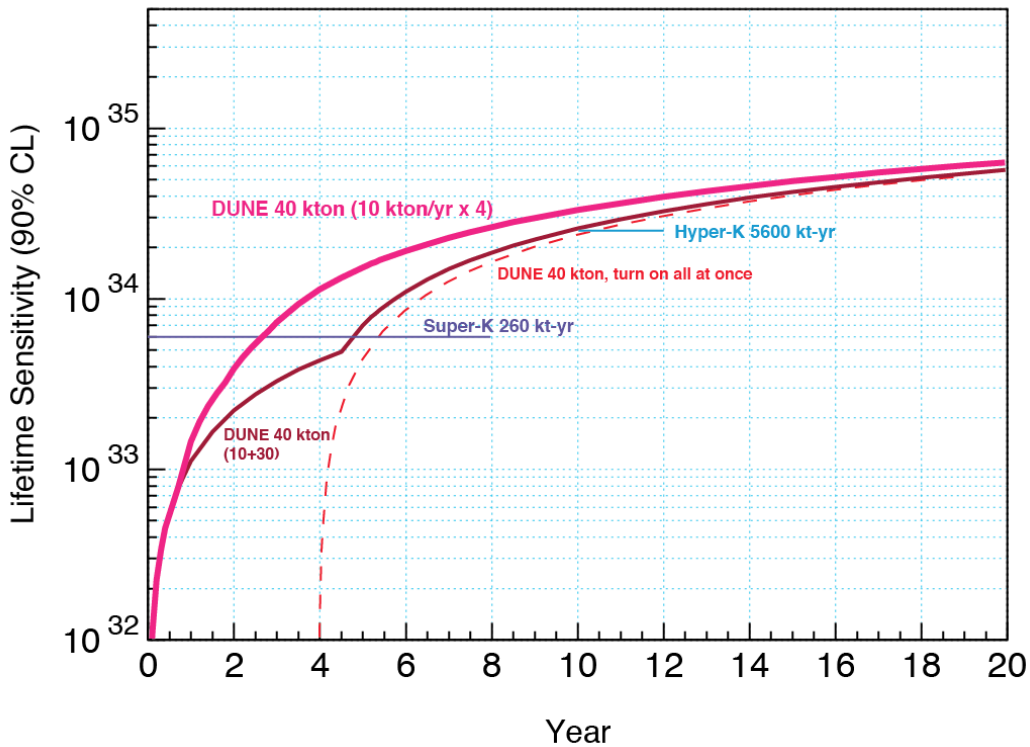
Figure 4.4: Proton decay lifetime limit for $p \rightarrow K^+\bar{\nu}$ as a function of time for underground LArTPCs starting with an initial 10 kt and adding another 10 kt each year for four years, for a total of 40 kt. For comparison, the current limit from SK and a projected limit from Hyper-K is also shown. The limits are at 90% C.L., calculated for a Poisson process including background, assuming that the detected events equal the expected background.

4.2   Atmospheric Neutrinos

Atmospheric neutrinos provide a unique tool to study neutrino oscillations: the oscillated flux contains all flavors of neutrinos and antineutrinos, is very sensitive to matter effects and to both Δm^2 values, and covers a wide range of L/E. In principle, all oscillation parameters could be measured, with high complementarity to measurements performed with a neutrino beam. Atmospheric neutrinos are of course available all the time, which is particularly important before the beam becomes operational. They also provide a laboratory in which to search for exotic phenomena where the dependence of the flavor-transition and survival probabilities on energy and path length can be defined. The DUNE far detector, with its large mass and the overburden to protect it from backgrounds, is an ideal tool for these studies. The following discussion will focus on the measurement of the oscillation parameters in which the role of atmospheric neutrinos is most important.

The sensitivity to oscillation parameters has been evaluated with a dedicated simulation, reconstruction and analysis chain. The fluxes of each neutrino species were computed at the far detector location, after oscillation. Interactions in the LAr medium were simulated with the GENIE event generator. Detection thresholds and energy resolutions based on full simulations were applied to the outgoing particles, to take into account detector effects. Events were classified as Fully Con-

tained (FC) or Partially Contained (PC) by placing the vertex at a random position inside the detector and tracking the lepton until it reached the edge of the detector. Partially Contained events are those where a final state muon exits the detector. The number of events expected for each flavor and category is summarized in Table 4.3.

Table 4.3: Atmospheric neutrino event rates including oscillations in $350\,\text{kt}\cdot\text{year}$ with a LArTPC, fully or partially contained in the detector fiducial volume.

Sample	Event Rate
fully contained electron-like sample	14,053
fully contained muon-like sample	20,853
partially contained muon-like sample	6,871

Figure 4.5 shows the expected L/E distribution for high-resolution, muon-like events from a $350\,\text{kt}\cdot\text{year}$ exposure. The data provide excellent resolution of the first two oscillation nodes, even when taking into account the expected statistical uncertainty. In performing oscillation fits, the data in each flavor/containment category are binned in energy and zenith angle.
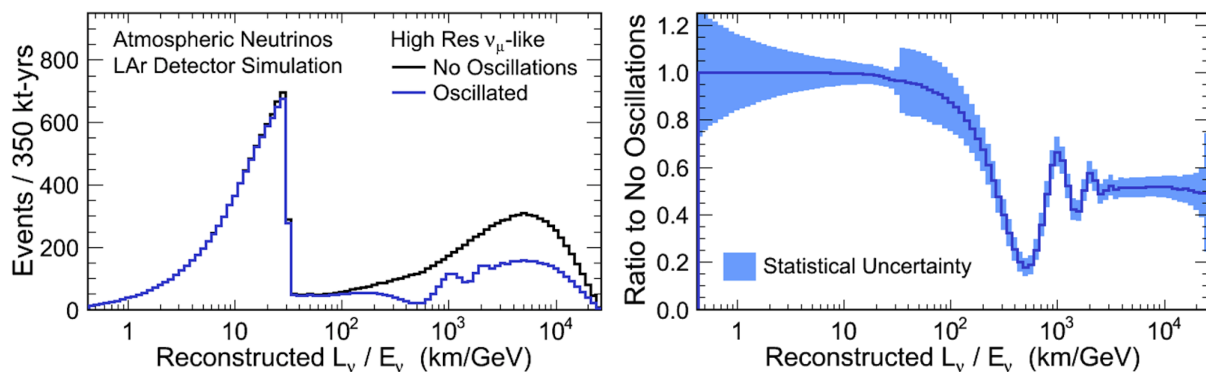
Figure 4.5: Reconstructed L/E Distribution of 'High-Resolution' μ-like atmospheric neutrino events in a $350\,\text{kt}\cdot\text{year}$ exposure with and without oscillations (left), and the ratio of the two (right), with the shaded band indicating the size of the statistical uncertainty.

When neutrinos travel through the Earth, the MSW resonance influences electron neutrinos in the few-GeV energy range. More precisely, the resonance occurs for ν_e in the case of normal mass hierarchy (NH, $\Delta m_{32}^2 > 0$), and for $\bar{\nu}_e$ in the case of inverted mass hierarchy (IH, $\Delta m_{32}^2 < 0$). This is illustrated in Figure 4.6.

The mass hierarchy (MH) sensitivity can be greatly enhanced if neutrino and antineutrino events can be separated. The DUNE detector will not be magnetized; however, its high-resolution imaging offers possibilities for tagging features of events that provide statistical discrimination between neutrinos and antineutrinos. For the sensitivity calculations that follow, two such tags were included: a proton tag and a decay electron tag.

Figure 4.7 shows the MH sensitivity as a function of the fiducial exposure. Over this range of fiducial exposures, the sensitivity goes essentially as the square root of the exposure, indicating that the measurement is not systematics-limited. Unlike for beam measurements, the sensitivity to
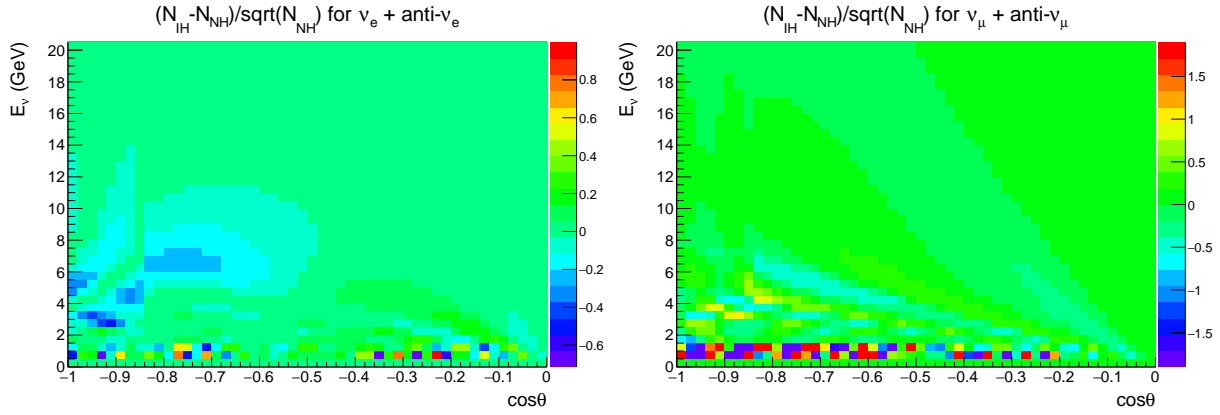
Figure 4.6: Statistical significance of the difference in expected event rates for NH and IH for electron neutrino events (left) and muon neutrino events (right), as a function of neutrino energy and zenith angle, for a $350\,\text{kt}\cdot\text{year}$ exposure.

MH with atmospheric neutrinos is nearly independent of the CP-violating phase. The sensitivity comes from both electron neutrino appearance as well as muon neutrino disappearance, and is strongly dependent on the true value of θ_{23}, as shown in Figure 4.7. Despite the much smaller mass, DUNE would have comparable sensitivity to Hyper-Kamiokande regarding atmospheric neutrino analyses [104] due to the higher detector resolution.
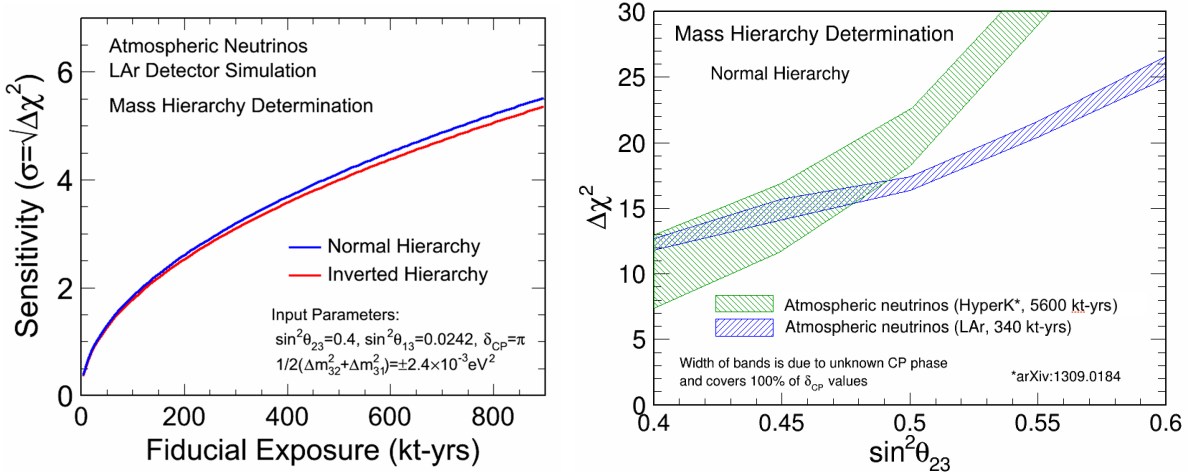
Figure 4.7: Sensitivity to mass hierarchy using atmospheric neutrinos as a function of fiducial exposure in a liquid argon detector (left), and as a function of the true value of θ_{23} (right). For comparison, Hyper-K sensitivities are also shown [104].

In the two-flavor approximation, neutrino oscillation probabilities depend on $\sin^2(2\theta)$, which is invariant when changing θ to $\pi/2 - \theta$. In this case, the octant degeneracy remains for θ_{23} in the leading order terms of the full three-flavor oscillation probability, making it impossible to determine whether $\theta_{23} < \pi/4$ or $\theta_{23} > \pi/4$. Accessing full three-flavor oscillation with atmospheric neutrinos will provide a handle for solving the ambiguity.

These analyses will provide an approach complementary to that of beam neutrinos. For instance, they should enable resolution of degeneracies that can be present in beam analyses, since the MH

sensitivity is essentially independent of δ_{CP}. Atmospheric neutrino data will be acquired even in the absence of the beam, and will provide a useful sample for the development of reconstruction software and analysis methodologies. Atmospheric neutrinos provide a window into a range of new physics scenarios, and may allow DUNE to place limits on CPT violation [83], non-standard interactions [105], mass-varying neutrinos [106], sterile neutrinos [107], and Lorentz invariance violation [84].

4.3   Indirect Search for WIMPs at the DUNE Far Detector

If the true nature of DM does indeed involve a weakly interacting particle (WIMP) with a mass in the 100's of GeV range, one of the main search strategies involves looking in astrophysical data for anomalous signals from the annihilation (or decay) of a WIMP into SM particles, like neutrinos. Signals of DM via neutrinos can come from such distant objects as the galactic center, the center of the Sun or even the Earth [108, 109, 110, 111, 112]. As our solar system moves through the DM halo, WIMPs interact with nuclei and become trapped in a body's gravitational well. Over time, the WIMPs accumulate near the core of the body, enhancing the possibility of annihilation. The high-energy neutrinos ($E \sim m_{\mathrm{WIMP}}$) from these annihilations can free-stream through the astrophysical body and emerge roughly unaffected (although oscillation and matter effects can slightly alter the energy spectrum). For the Sun, the background of neutrinos is produced at much lower energies via the nuclear fusion process. Thus, the detection of high-energy neutrinos pointing from the Sun and detected in the DUNE far detector would be clear evidence of DM annihilation. Since the DUNE far detector has relatively large mass, of the order tens of kt, it can act as a "neutrino telescope" and be used to search for signals of DM annihilations coming from the Sun and/or the core of the Earth. IceCube [113] and Super-Kamiokande [114] have searched for WIMPs with masses from a few to a few hundred GeV/c^2 using this method, but have not observed a signal of DM annihilation into neutrinos. These indirect-detection experiments are limited by atmospheric neutrino background. Compared to these experiments, which are based on Cherenkov light detection, the DUNE LArTPC can provide much better angular resolution. This would substantially reduce the background in the direction of the expected WIMP-induced neutrino signal, and could potentially provide competitive limits in the low-WIMP-mass range. Studies are needed to investigate the sensitivity of DUNE for indirect WIMP detection.

4.4   Detector Requirements

Physics with atmospheric neutrino interactions and searches for nucleon decays have several requirements that are not necessarily in common with the beam-related physics program. Detector mass and depth plays a more critical role here; the atmospheric "beam" is fixed, and the number of nucleons available to decay obviously depends on the number of nuclei in the detector. The DUNE Far Detector Requirements [85] specific to searches for proton decay and measurements of the atmospheric neutrino flux are as follows:

- Far Detector Depth: The far detector shall be located at sufficient depth to allow detection

of atmospheric neutrinos and proton decay with negligible backgrounds from cosmogenic sources. Depth plays a greater role for these physics topics than for long-baseline neutrino oscillations, because of the lack of a beam gate coincidence. As discussed in the previous sections, cosmic ray interactions in the surrounding rock and detector dead regions can lead to critical backgrounds, or create difficulties for reconstruction algorithms. Analyses of backgrounds [92, 97, 98, 19] has shown that a depth of 4850 ft is sufficient to reduce these backgrounds to negligible levels.

- Far Detector Mass: The far-detector fiducial size multiplied by the duration of operation [expressed in kiloton-years] shall be sufficient to yield a scientifically competitive result on proton decay. As Figure 4.4 shows, a $10-$kt detector can exceed the existing Super-Kamiokande limits for the $p \to K^+ + \bar{\nu}$ nucleon decay channel in five years, and the full $40-$kt scope in a much shorter time than that. For atmospheric neutrinos, a detector mass of 40 kt will achieve a mass hierarchy determination of better than 3σ in 10 years.

- Far Detector DAQ: The far detector DAQ must enable continuous recording of data, outside of any beam gate, and retain enough information from the front end (including photon system) through the DAQ chain to enable a trigger on events of interest. The DAQ must keep any information that would allow the identification of putative events, and its livetime fraction should be higher than the efficiency of all other cuts placed on the data. The trigger system itself must be able to provide information that allows linking of tracks in different modules of the far detector.

- Far Detector Particle ID: It is required that the separation of K^+'s and π^+'s in the Far Detector be sufficient to ensure that much less than one event leak into the $p \to K^+ \bar{\nu}$ sample. Unlike the long-baseline physics, proton decay physics requires a rare-process search; therefore small tails from e.g., atmospheric neutrino interactions creating π^+s that are misidentified could be very damaging.

- Far Detector Energy Resolution: It is required that the energy resolution be known well enough that its uncertainty is a negligible contribution to the measurement of the atmospheric neutrino energy spectrum of all flavors and that this uncertainty have a negligible impact on background predictions for proton decay.

Chapter 5

Supernova Neutrino Bursts and Low-energy Neutrinos

5.1 Overview

The DUNE experiment will be sensitive to neutrinos in the few tens of MeV range, which create short electron tracks in liquid argon, potentially accompanied by a few gamma rays. This regime is of particular interest for detection of the burst of neutrinos from a galactic core-collapse supernova (the primary focus of this chapter). The sensitivity of DUNE is primarily to *electron flavor* supernova neutrinos, and this capability is unique among existing and proposed supernova neutrino detectors for the next decades. Neutrinos from other astrophysical sources are also potentially detectable. The low-energy event regime has several reconstruction, background and triggering challenges.

The observation of neutrinos from the celebrated SN1987A core collapse [115, 116] in the Large Magellanic Cloud outside the Milky Way provided qualitative validation of the basic physical picture of core-collapse and provided powerful constraints on numerous models of new physics. At the same time, the statistics were sparse and many questions remain. A high-statistics observation of a nearby supernova neutrino burst would be possible with the current generation of detectors. Such an observation would shed light on the nature of the astrophysical event, as well as on the nature of neutrinos themselves. Sensitivity to the different flavor components of the flux is highly desirable.

5.1.1 The Stages of Core Collapse

As a result of nuclear burning throughout a massive star's lifetime, the inner region of the star forms an "onion" structure, with an iron core at the center surrounded by concentric shells of lighter elements (silicon, oxygen, neon, magnesium, carbon, etc.). Eventually the core collapses,

causing a core-collapse supernova[1].

As the star ages, its iron core, at temperatures of $T \sim 10^{10}$ K and densities of $\rho \sim 10^{10}$ g/cm^3, continuously loses energy through neutrino emission caused by pair annihilation and plasmon decay. Since iron does not burn, there is no mechanism to replenish this lost energy within the core, and the core continues to contract and heat up. Meanwhile, the shells around it burn, producing iron that gravitates to the core, adding mass to it. When the core reaches the critical mass of about $1.4M_\odot$ of Fe, a stable configuration is no longer possible. At this point, as electrons are absorbed by the protons and some iron is disintegrated by thermal photons, the pressure support is suddenly removed and the core collapses essentially in free fall, reaching speeds of about a quarter of the speed of light. [2]

The collapse of the core suddenly halts after $\sim 10^{-2}$ seconds, as the density reaches nuclear (and up to supra-nuclear) values. The core then bounces and a shock wave forms. The extreme physical conditions of this core, in particular the densities of order $10^{12} - 10^{14}$ g/cm^3, create a medium that is opaque even to neutrinos; the temperature of this core is $\lesssim 30$ MeV, which is relatively *cold*. At this stage, the gravitational energy of the collapse is stored mostly in the degenerate Fermi sea of electrons ($E_F \sim 200$ MeV) and electron neutrinos, which are in equilibrium with each other, and the core's lepton number is trapped.

A point is reached where the trapped energy and lepton number both escape from the core, carried by the least interacting particles, i.e., neutrinos, according to the Standard Model. A tremendous amount of energy, some 10^{53} ergs, is released in a time span of a few seconds by 10^{58} neutrinos and antineutrinos of all flavors, with energies of ~ 10 MeV. A small fraction of this energy is absorbed by beta reactions that form a shock wave. This shock wave blasts away the rest of the star creating a spectacular explosion, which, curiously enough, is only a tiny perturbation from the energetics point of view.

Over 99% of all gravitational binding energy of the $1.4M_\odot$ collapsed core – some 10% of its rest mass – has now been emitted as neutrinos. The resulting central object then settles to a neutron star or a black hole.

5.1.2   Observable Signals from the Explosion

The flavor content and spectra of the neutrinos emitted from the neutrinosphere (the surface of neutrino trapping) change throughout the phases of the core collapse, and the neutrino signal provides information on the supernova's evolution.

The signal starts with a short, sharp *neutronization* (or *break-out*) burst primarily composed of ν_e. This quick and intense burst is followed by an *accretion* phase lasting some hundreds of milliseconds, depending on the progenitor star mass, as matter falls onto the collapsed core and the shock is stalled at the distance of perhaps ~ 200 km. The gravitational binding energy of

---

[1]In this chapter "Supernova" always refers to a "core-collapse supernova."

[2]Other collapse mechanisms are possible: an "electron-capture" supernova does not reach the final burning phase before highly degenerate electrons break apart nuclei and trigger a collapse.

the accreting material powers the neutrino luminosity during this stage. The *cooling* phase that follows, lasting ~10 seconds, represents the main part of the signal, over which the proto-neutron star sheds its trapped energy.

Some fairly generic features of the neutrinos emitted in each stage are illustrated in Figure 5.1, based on a 1-dimensional model of [117] and reproduced from [118].
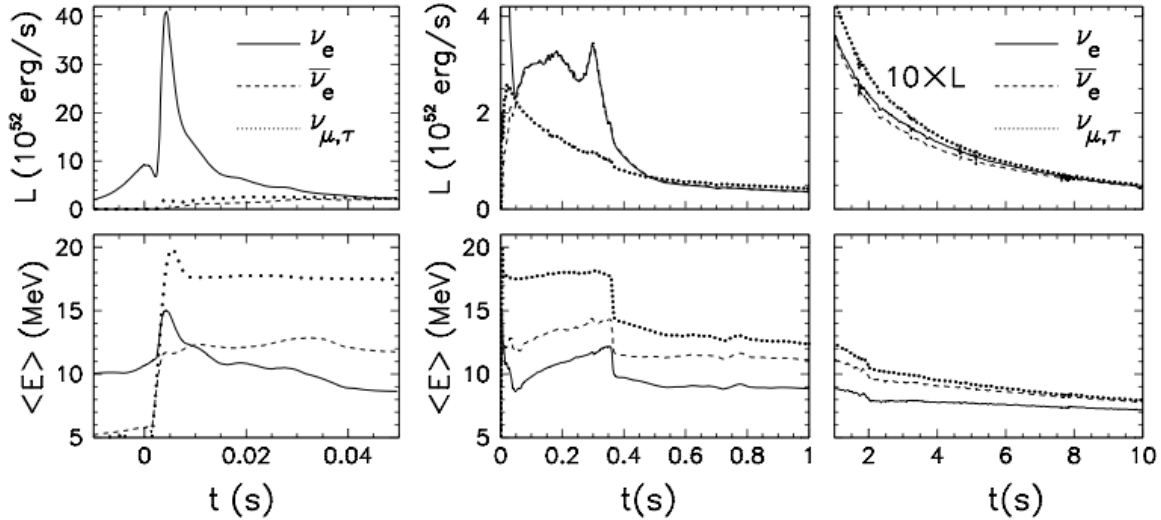
Figure 5.1: Expected core-collapse neutrino signal from the "Basel" model [117], for a 10.8 $M_\odot$ progenitor. The left plots show the very early signal, including neutronization burst; the middle plots show the accretion phase, and the right plots show the cooling phase. Across the top, luminosities as a function of time are shown. Across the bottom, the plots show average energy as a function of time for the ν_e, $\bar{\nu}_e$ and $\nu_{\mu,\tau}$ flavor components of the flux (fluxes for ν_μ, $\bar{\nu}_\mu$, ν_τ, and $\bar{\nu}_\tau$ should be identical). Figure courtesy of [118].

The physics of neutrino decoupling and spectrum formation is far from trivial, owing to the energy dependence of the cross sections and the roles played by both charged- and neutral-current reactions. Detailed transport calculations using methods such as Monte Carlo or Boltzmann solvers have been employed. It has been observed that spectra coming out of such simulations can typically be parameterized at a given moment in time by the following ansatz (e.g., [119, 120]):

$$\phi(E_\nu) = \mathcal{N} \left(\frac{E_\nu}{\langle E_\nu \rangle} \right)^\alpha \exp\left[-(\alpha + 1) \frac{E_\nu}{\langle E_\nu \rangle} \right] , \tag{5.1}$$

where E_ν is the neutrino energy, $\langle E_\nu \rangle$ is the mean neutrino energy, α is a "pinching parameter," and $\mathcal{N}$ is a normalization constant. Large α corresponds to a more *pinched* spectrum (suppressed high-energy tail). This parameterization is referred to as a *pinched-thermal* form. The different ν_e, $\bar{\nu}_e$ and ν_x, $x = \mu, \tau$ flavors are expected to have different average energy and α parameters and to evolve differently in time.

The initial spectra get further processed (permuted) by flavor oscillations; understanding these oscillations is very important for extracting physics from the detected signal.

5.1.3   Detection Channels and Interaction Rates in Liquid Argon

Liquid argon has a particular sensitivity to the ν_e component of a supernova neutrino burst, via charged-current (CC) absorption of ν_e on ^{40}Ar,

$$\nu_e + {}^{40}\text{Ar} \rightarrow e^- + {}^{40}\text{K}^*, \qquad (5.2)$$

for which the observables are the e^- plus de-excitation products from the excited K^* final state, as well as a $\bar{\nu}_e$ interaction and elastic scattering on electrons. Cross sections for the most relevant interactions are shown in Figure 5.2.
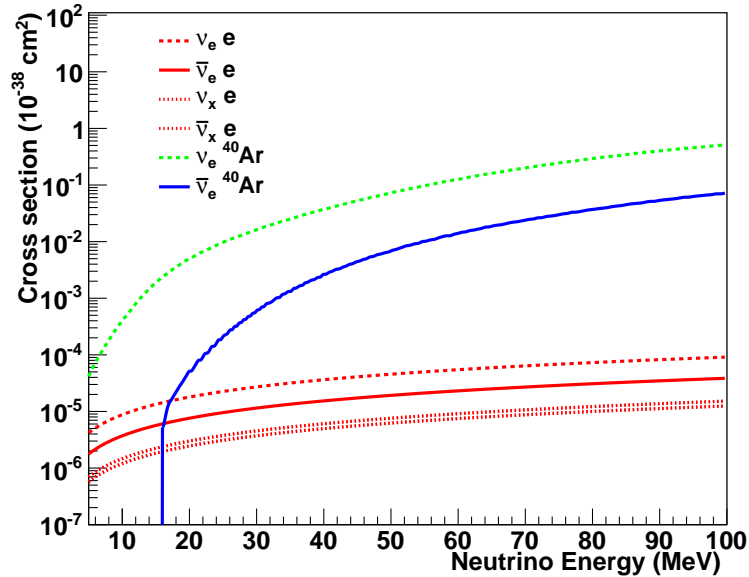
Figure 5.2: Cross sections for supernova-relevant interactions in argon [121, 122].

Neutral-current (NC) scattering on Ar nuclei by any type of neutrino, $\nu_x + \text{Ar} \rightarrow \nu_x + \text{Ar}^*$, is another process of interest for supernova detection in LAr detectors that is not yet fully studied. The signature is given by the cascade of de-excitation γs from the final-state Ar nucleus. A dominant 9.8-MeV Ar* decay line has been recently identified as a spin-flip M1 transition [123]. At this energy the probability of e^+e^- pair production is relatively high, offering a potentially interesting neutral-current tag.

The predicted event rate (NC or CC) from a supernova burst may be calculated by folding expected neutrino differential energy spectra in with cross sections for the relevant channels and with detector response; this is done using SNOwGLoBES [122], which uses Icarus detector resolution [124] and assumes a detection threshold of 5 MeV.

Table 5.1 shows rates calculated for the dominant interactions in argon for the "Livermore" model [125] (no longer preferred, but included for comparison with literature), and the "GKVM" model [126]; for the former, no oscillations are assumed; the latter assumes collective oscillation effects (see Section 5.2). There is a rather wide variation — up to an order of magnitude —

in event rate for different models, due to different numerical treatment (e.g., neutrino transport, dimensionality), physics input (nuclear equation of state, nuclear correlation and impact on neutrino opacities, neutrino-nucleus interactions) and oscillation effects. In addition, there is intrinsic variation in the nature of the progenitor and collapse mechanism. Furthermore, neutrino emission from the supernova may exhibit an emitted lepton-flavor asymmetry [127], which would lead to observed rates being direction-dependent.

Table 5.1: Event rates for different supernova models in 40 kt of liquid argon for a core collapse at 10 kpc, for ν_e and $\bar{\nu}_e$ charged-current channels and elastic scattering (ES) on electrons. Event rates will simply scale by active detector mass and inverse square of supernova distance. The "Livermore" model assumes no oscillations; "GKVM" assumes collective oscillation effects. Oscillations (both standard and "collective") will potentially have a large, model-dependent effect.

Channel	Events "Livermore" model	Events "GKVM" model
$\nu_e + {}^{40}\mathrm{Ar} \to e^- + {}^{40}\mathrm{K}^*$	2720	3350
$\bar{\nu}_e + {}^{40}\mathrm{Ar} \to e^+ + {}^{40}\mathrm{Cl}^*$	230	160
$\nu_x + e^- \to \nu_x + e^-$	350	260
Total	3300	3770

Figure 5.3 shows another example of an expected burst signal, for which a calculation with detailed time-dependence of the spectra is available [128] out to 9 seconds post-bounce. This model has relatively low luminosity but includes the standard robust neutronization burst. Note that the relative fraction of neutronization-burst events is quite high. Figure 5.4 shows the event channel breakdown for the same model. Clearly, the ν_e flavor dominates. Although other types of detectors, i.e., water and scintillator, have the capability to record ν_e events [129, 130], liquid argon offers the only prospect for observation of a large, clean supernova ν_e sample [131].

The number of signal events scales with mass and inverse square of distance as shown in Figure 5.5. For a collapse in the Andromeda galaxy, a 40-kt detector would observe a few events.

5.2   Neutrino Physics and Other Particle Physics

The key property of neutrinos that leads to a dominant role in supernova dynamics is the feebleness of their interactions. It then follows that should there be unknown, even weaker interactions or properties of neutrinos, or new, light (< 100 MeV) weakly interacting particles, they could alter the energy transport process and the resulting evolution of the nascent proto-neutron star. A core-collapse supernova can be thought of as a hermetic system that can be used to search for numerous types of new physics (e.g., [132, 133]). The list includes various Goldstone bosons (e.g., Majorons), neutrino magnetic moments, new gauge bosons (*dark photons*), *unparticles*, and extra-dimensional gauge bosons. The existing data from SN1987A already provide significant constraints on these scenarios, by confirming the basic energy balance of the explosion. At the same time, more precision is highly desirable and should be provided by the next galactic supernova.
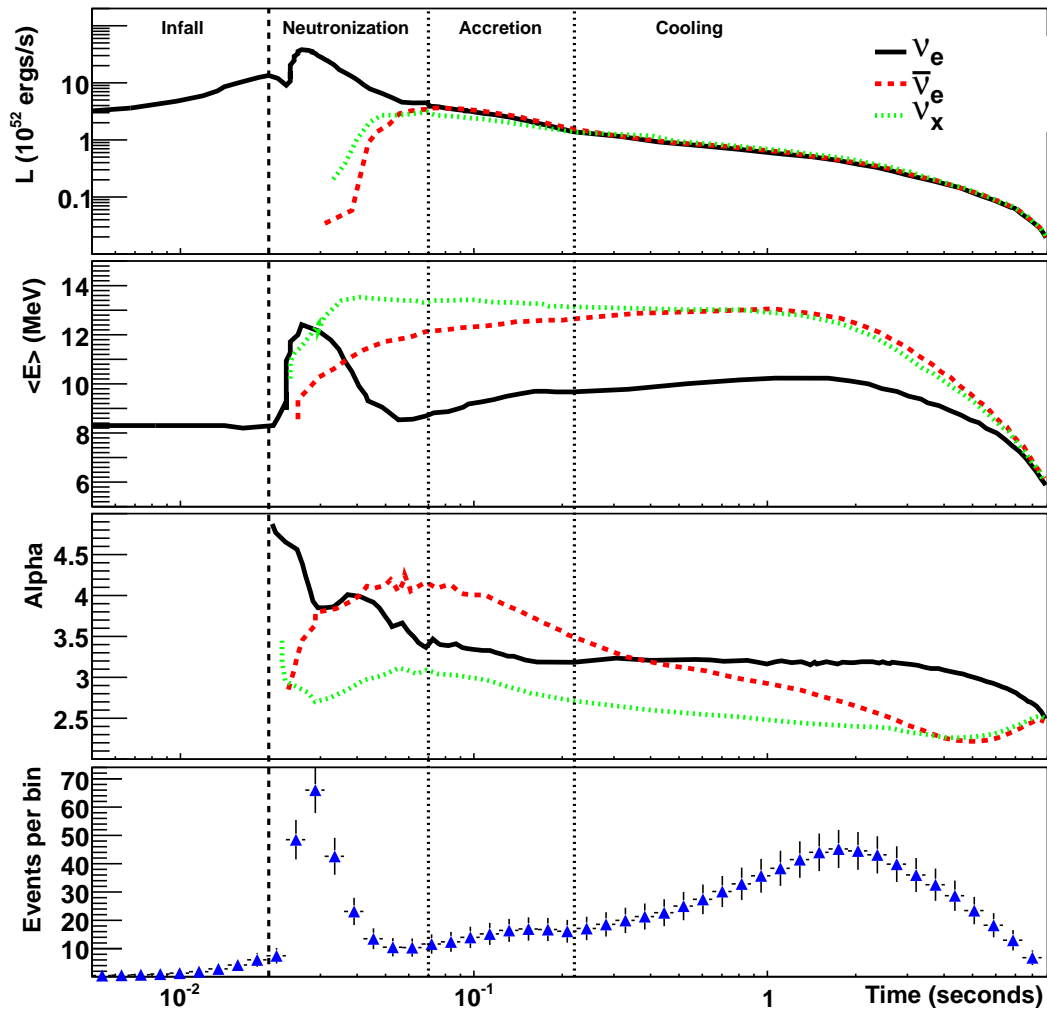
Figure 5.3: Expected time-dependent signal for a specific flux model for an electron-capture supernova [128] at 10 kpc. No oscillations are assumed. The top plot shows the luminosity as a function of time, the second plot shows average neutrino energy, and the third plot shows the α (pinching) parameter. The fourth (bottom) plot shows the total number of events (mostly ν_e) expected in 40 kt of liquid argon, calculated using SNOwGLoBES. Note the logarithmic binning in time; the plot shows the number of events expected in the given bin and the error bars are statistical. The vertical dashed line at 0.02 seconds indicates the time of core bounce, and the vertical lines indicate different eras in the supernova evolution. The leftmost time interval indicates the infall period. The next interval, from core bounce to 50 ms, is the neutronization burst era, in which the flux is composed primarily of ν_e. The next period, from 50 to 200 ms, is the accretion period. The final era, from 0.2 to 9 seconds, is the proto-neutron-star cooling period.
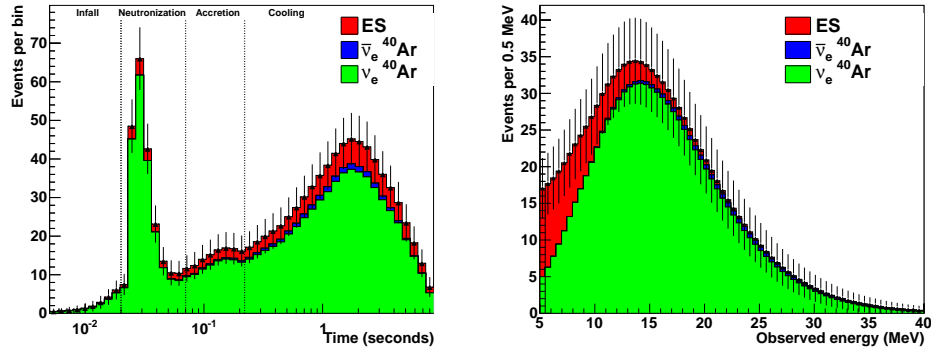
Figure 5.4: Left: Expected time-dependent signal in 40 kt of liquid argon for the electron-capture supernova [128] at 10 kpc, calculated using SNoWGLoBES [122], showing breakdown of event channels. Right: expected measured event spectrum for the same model, integrated over time.
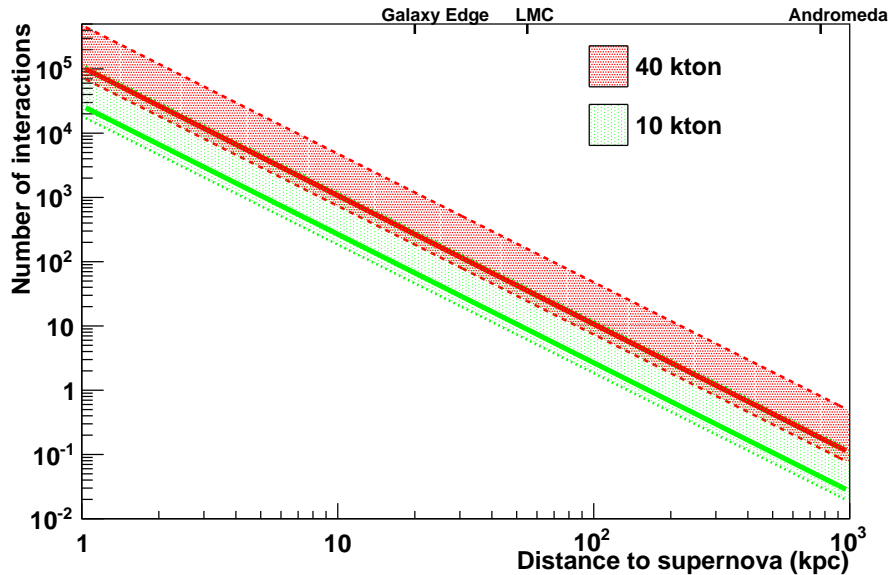
Figure 5.5: Estimated numbers of supernova neutrino interactions in DUNE as a function of distance to the supernova, for different detector masses (ν_e events dominate). The red band represents expected events for a 40-kt detector and the green band represents expected events for a 10-kt detector. The borders of these bands (dashed lines) limit a fairly wide range of possibilities for "Garching-parameterized" supernova flux spectra (Equation 5.1) with luminosity 0.5×10^{52} ergs over ten seconds. The optimistic upper line of a pair gives the number of events for average ν_e energy of $\langle E_{\nu_e} \rangle = 12$ MeV, and "pinching" parameter $\alpha = 2$; the pessimistic lower line of a pair gives the number of events for $\langle E_{\nu_e} \rangle = 8$ MeV and $\alpha = 6$. (Note that the luminosity, average energy and pinching parameters will vary over the time frame of the burst, and these estimates assume a constant spectrum in time. Oscillations will also affect the spectra and event rates.) The solid lines represent the integrated number of events for the specific time-dependent neutrino flux model in [128] (see Figs. 5.3 and 5.4; this model has relatively cool spectra and low event rates). Core collapses are expected to occur a few times per century, at a most-likely distance of around 10 to 15 kpc.
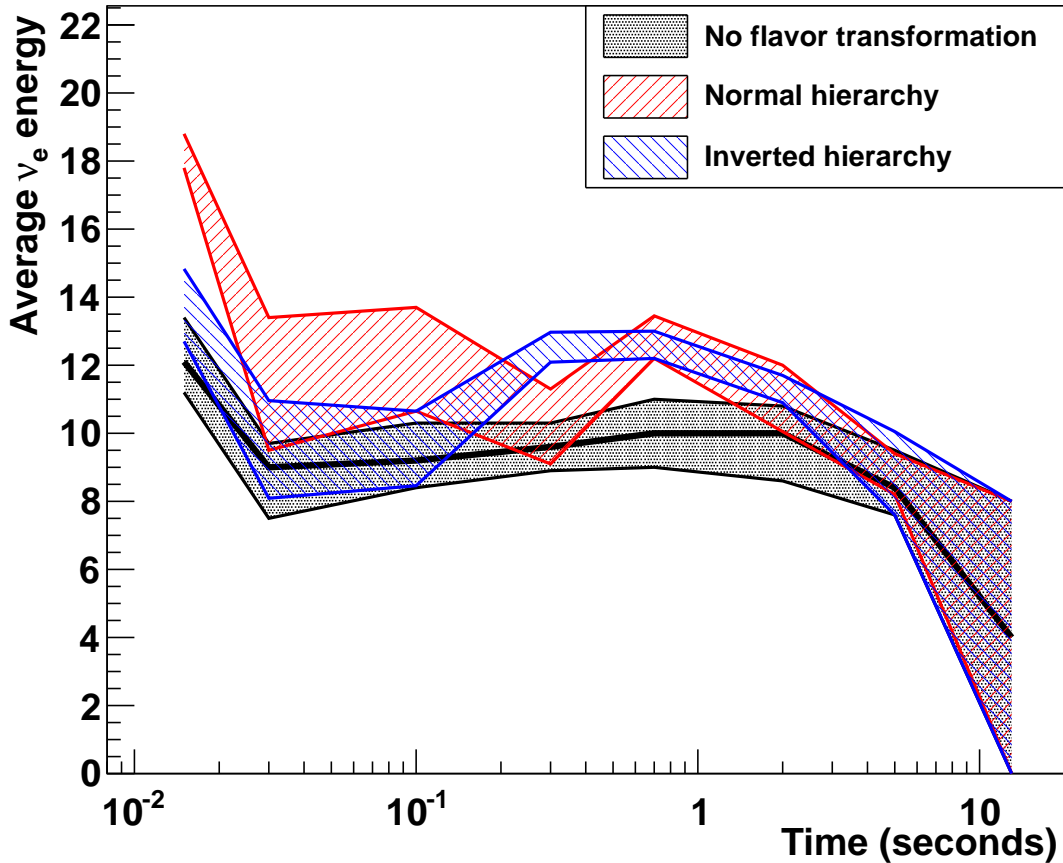
Figure 5.6:   Average ν_e energy from a simulated fit to the oscillated fluxes predicted by the Garching 1D model with a light (10.8 $M_\odot$) progenitor. DUNE's oscillation calculations included full multi-angle treatment of collective evolution, for two different mass hierarchy assumptions. The predicted events were then smeared with SNOwGLoBES and fit with a pinched-thermal spectrum as a function of time (assuming a supernova at 10 kpc and a 34 kt LAr detector). The bands represent 1σ error bars from the fit (assuming only statistical uncertainties). The solid black line is the true $\langle E_\nu \rangle$ for the unoscillated spectrum. Clearly, the rate of energy escape from the proto-neutron star can be gleaned by tracking ν_e spectra as a function of time.

The analysis of possible supernova events will make use of two types of information. First, the total energy of the emitted neutrinos will be compared with the expected release in the gravitational collapse. Note that measurements of all flavors, including ν_e, are needed for the best estimate of the energy release. Second, the rate of cooling of the proto-neutron state should be measured and compared with what is expected from diffusion of the standard neutrinos. This requires comparing one-second-interval time-integrated spectra successively as illustrated in Figure 5.6.

Because DUNE is mostly sensitive to ν_e, in order to enable inference of the fluxes of μ and τ flavors complementary $\bar{\nu}_e$ measurements are needed from water Cherenkov and scintillator detectors, as is a careful analysis of the oscillation pattern (see below). Measuring the energy loss rate will require sufficient statistics at late times and, once again, an understanding of the oscillation dynamics; this is evident in Figure 5.6 where oscillated and unoscillated cases are shown.

The flavor oscillation physics and its signatures are a major part of the physics program. Compared to the well understood case of solar neutrinos, supernova neutrino flavor transformations are much more involved. Besides the facts that neutrinos and antineutrinos of all flavors are emitted and there are two mass splittings – "solar" and "atmospheric" – the physics of the transformations is significantly richer. For example, several seconds after the onset of the explosion, the flavor conversion probability is affected by the expanding shock front and the turbulent region behind it. The conversion process in such a stochastic profile is qualitatively different from the adiabatic MSW effect in the smooth, fixed-density profile of the Sun.

Even more complexity is brought about by the coherent scattering of neutrinos off each other. This neutrino "self-refraction" results in highly nontrivial flavor transformations close to the neutrinosphere, typically within a few hundred kilometers from the center, where the density of streaming neutrinos is very high. Since the evolving flavor composition of the neutrino flux feeds back into the oscillation Hamiltonian, the problem is *nonlinear*. Furthermore, as the interactions couple neutrinos and antineutrinos of different flavors and energies, the oscillations are characterized by *collective* modes. This leads to very rich physics that has been the subject of intense theoretical interest over the last decade. A voluminous literature exists exploring these collective phenomena, e.g., [134, 135, 136, 137, 138, 139, 140, 141, 142, 143] the effects of which are not yet fully understood. A supernova burst is the only opportunity to study neutrino-neutrino interactions experimentally.

Matter effects in the Earth can also have a MH-dependent effect on the signal (e.g., [144]).

One may wonder whether all this complexity will impede the extraction of useful information from the future signal. In fact, the opposite is true: the new effects can *imprint* information about the inner workings of the explosion on the signal. The oscillations can modulate the characteristics of the signal (both event rates and spectra as a function of time), as seen in Figure 5.6. Moreover, the oscillations can imprint *non-thermal* features on the energy spectra, potentially making it possible to disentangle the effects of flavor transformations and the physics of neutrino spectra formation. This in turn should help illuminate the development of the explosion during the crucial first 10 seconds. It is important to note that the features depend on the unknown mass hierarchy, and therefore may help reveal it.

Figure 5.7 illustrates the effects of collective oscillations. These oscillations serve to permute
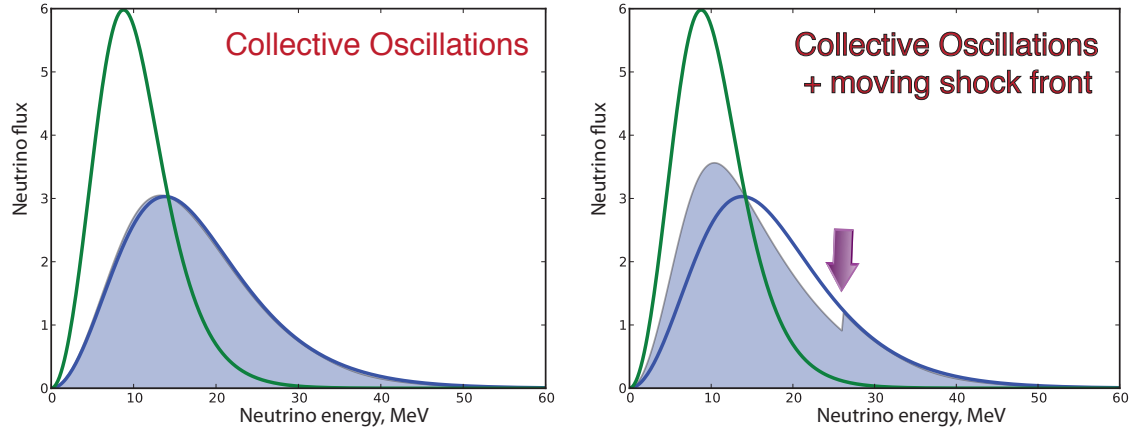
Figure 5.7: Both panels show solid lines that represent the simulated unoscillated ν_e (green, cooler) and ν_x (blue, hotter) fluxes. The filled curve shows the observed flux after the collective oscillations in the absence of (left) and presence of (right) the shock front. (Flux is shown in arbitrary units)

almost completely the original ν_e and $\nu_{\mu,\tau}$ spectra, so that the flux of observed electron neutrinos is noticeably hotter than the original one. Moreover, the shock front modulates the MSW conversion probability and imprints a non-thermal *step* in the spectrum. Below this step, the swap between the original ν_e and $\nu_{\mu,\tau}$ spectra is only partial. As the shock expands, the feature moves to higher energies, creating a "smoking-gun" signature that exists only in the neutrino channel.

As another example of a probe of new physics with supernova neutrinos or antineutrinos, a class of tests of Lorentz and CPT violation involves comparing the propagation of neutrinos with other species or of neutrinos of the same flavor but different energies [83, 145, 84, 146]. These amount to time-of-flight or dispersion studies.

Time-of-flight and dispersion effects lack the interferometric resolving power available to neutrino oscillations, but they provide sensitivity to Lorentz- and CPT-violating effects that cannot be detected via oscillations. The corresponding SME coefficients controlling these effects are called oscillation-free coefficients [84]. Supernova neutrinos are of particular interest in this context because of the long baseline, which implies sensitivities many orders of magnitude greater than available from time-of-flight measurements in beams. Observations of the supernova SN1987A yield constraints on the difference between the speed of light and the speed of neutrinos, which translates into constraints on isotropic and anisotropic coefficients in both the minimal and nonminimal sectors of the SME. Knowledge of the spread of arrival times constrains the maximum speed difference between SN1987A antineutrinos of different energies in the approximate range 10–40 MeV, which restricts the possible antineutrino dispersion and yields further constraints on SME coefficients [84].

Analyses of this type would be possible with DUNE if supernova neutrinos are observed. Key features for maximizing sensitivity would include absolute timing information to compare with photon spectral observations and relative timing information for different components of the neutrino energy spectrum. Significant improvements over existing limits are possible. Figure 5.8 displays DUNE supernova sensitivities to coefficients for Lorentz and CPT violation that leave neutrino

oscillations unaffected and so cannot be measured using atmospheric or long-baseline neutrinos. The figure assumes a supernova comparable to SN1987A (optimistically at a distance of 50 kpc). Studies of supernova neutrinos using DUNE can measure many coefficients (green) at levels that improve on existing limits (grey).
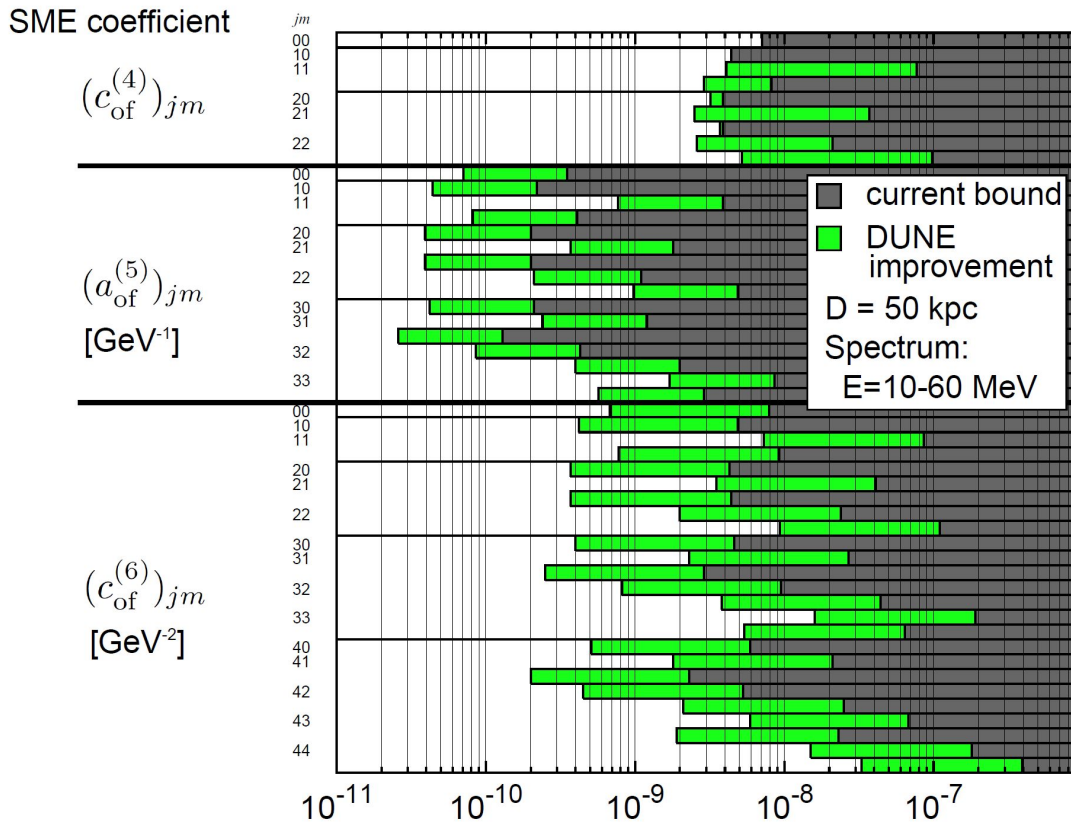
Figure 5.8: DUNE supernova sensitivities to oscillation-free coefficients for Lorentz and CPT violation. Studies of DUNE supernova neutrinos can measure many coefficients (green) at levels improving over existing limits (grey). These Lorentz- and CPT-violating effects leave oscillations unchanged and so are unobservable in atmospheric or long-baseline measurements [147].

Finally, via detection of time-of-flight delayed ν_e from the neutronization burst, DUNE will be able to probe neutrino mass bounds of $\mathcal{O}(1)$ eV for a 10-kpc supernova [148] (although will likely not be competitive with near-future terrestrial kinematic limits). If eV-scale sterile neutrinos exist, they will likely have an impact on astrophysical and oscillation aspects of the signal (e.g., [149, 150, 151]), as well as time-of-flight observables.

5.3   Astrophysics

A number of astrophysical phenomena associated with supernovae are expected to be observable in the supernova neutrino signal, providing a remarkable window into the event. In particular, the supernova explosion mechanism, which in the current paradigm involves energy deposition via neutrinos, is still not well understood, and the neutrinos themselves will bring the insight needed to confirm or refute the paradigm.

There are many other examples of astrophysical observables.

- The short initial "neutronization" burst, primarily composed of ν_e, represents only a small component of the total signal. However, oscillation effects can manifest themselves in an observable manner in this burst, and flavor transformations can be modified by the "halo" of neutrinos generated in the supernova envelope by scattering [152].

- The formation of a black hole would cause a sharp signal cutoff (e.g., [153, 154]).

- Shock wave effects (e.g., [155]) would cause a time-dependent change in flavor and spectral composition as the shock wave propagates.

- The standing accretion shock instability (SASI) [156, 157], a "sloshing" mode predicted by three-dimensional neutrino-hydrodynamics simulations of supernova cores, would give an oscillatory flavor-dependent modulation of the flux.

- Turbulence effects [158, 159] would also cause flavor-dependent spectral modification as a function of time.

Observation of a supernova neutrino burst in coincidence with gravitational waves (which would also be prompt, and could indeed provide a time reference for a time-of-flight analysis) would be especially interesting [160, 161, 162, 163].

The supernova neutrino burst is prompt with respect to the electromagnetic signal and therefore can be exploited to provide an early warning to astronomers [164, 165]. Additionally, a liquid argon signal [166] is expected to provide some pointing information, primarily from elastic scattering on electrons. We note that not every core collapse will produce an observable supernova, and observation of a neutrino burst in the absence of light would be very interesting.

Even non-observation of a burst, or non-observation of a ν_e component of a burst in the presence of supernovae (or other astrophysical events) observed in electromagnetic or gravitational wave channels, would still provide valuable information about the nature of the sources. Further, a long-timescale, sensitive search yielding no bursts will also provide limits on the rate of core-collapse supernovae.

We note that the better one can understand the astrophysical nature of core-collapse supernovae, the easier it will be to extract information about particle physics. DUNE's capability to characterize the ν_e component of the signal is unique and critical.

5.4   Additional Astrophysical Neutrinos

5.4.1   Solar Neutrinos

Intriguing questions in solar neutrino physics remain, even after data from the Super-K and SNO [167, 168] experiments explained the long-standing mystery of missing solar neutrinos [169] as due to flavor transformations. Some unknowns, such as the fraction of energy production via the CNO cycle in the Sun, flux variation due to helio-seismological modes that reach the solar core, or long-term stability of the solar core temperature, are astrophysical in nature. Others directly impact particle physics. Can the MSW model explain the amount of flavor transformation as a function of energy, or are non-standard neutrino interactions required? Do solar neutrinos and reactor antineutrinos oscillate with the same parameters?

Detection of solar and other low-energy neutrinos is challenging in a LArTPC because of relatively high intrinsic detection energy thresholds for the charged-current interaction on argon (>5 MeV). Compared with other technologies, a LArTPC offers a large cross section and unique potential signatures from de-excitation photons. Aggressive R&D efforts in low-energy triggering and control of background from radioactive elements may make detection of solar neutrinos in DUNE possible.

Signatures of solar neutrinos in DUNE are elastic scattering on electrons as well as CC absorption of ν_e on ^{40}Ar (equation 5.2), which has a 4.5-MeV energy threshold and a large cross section compared to elastic scattering on electrons. Furthermore, the CC absorption differential cross section (the interaction products track neutrino energy closely) potentially enables precise solar-neutrino spectral measurements. The solar neutrino event rate in a $40-$kt LArTPC, assuming a roughly $4.5-$MeV neutrino energy threshold and 31% ν_e survival, is 122 per day.

The solar neutrino physics potential of a large LArTPC depends on the ability to pick up a low-energy electron, light collection of the photon-triggering system, and, critically, on background suppression. The decay of the naturally occurring ^{39}Ar produces β's with a $567-$keV endpoint and an expected rate of 10 MHz per 10 kt of liquid argon. This limits the fundamental reach of DUNE to neutrino interactions with visible energies above 1 MeV. Cosmic-muon and fast-neutrino interactions with the ^{40}Ar nucleus (which are rather complex compared to interactions on ^{16}O or ^{12}C) are likely to generate many long-lived spallation products which could limit the detection threshold for low-energy neutrinos. ^{40}Cl, a beta emitter with an endpoint of 7.48 MeV, is a dominant source of background at energies above 5 MeV, and is expected to be produced with a rate on the order of 10 per kiloton of LAr per day at 4850 ft.

The ICARUS collaboration has reported a $10-$MeV threshold [170]. Assuming the detector itself has low enough radioactivity levels, this threshold level would enable a large enough detector to measure the electron flavor component of the solar ^{8}B neutrino flux with high statistical accuracy. It could thereby further test the MSW flavor transformation curve with higher statistical precision and potentially better energy resolution. In addition to these solar matter effects, solar neutrinos also probe terrestrial matter effects with the variation of the ν_e flavor observed with solar zenith angle while the Sun is below the horizon — the day/night effect (reported recently in [171]). The comparison of solar and reactor disappearance tests CPT invariance as well as other new physics.

5.4.2 Diffuse Supernova Background Neutrinos

Galactic supernovae are relatively rare, occurring somewhere between once and four times a century. In the Universe at large, however, thousands of neutrino-producing explosions occur every hour. The resulting neutrinos — in fact most of the neutrinos emitted by all the supernovae since the onset of stellar formation — suffuse the Universe. Known as the *diffuse supernova neutrino background (DSNB)*, their energies are in the few-to-$30-$MeV range. The DSNB has not yet been observed, but an observation would greatly enhance our understanding of supernova-neutrino emission and the overall core-collapse rate [172].

A liquid argon detector such as DUNE's far detector is sensitive to the ν_e component of the diffuse relic supernova neutrino flux, whereas water Cherenkov and scintillator detectors are sensitive to the antineutrino component. However, backgrounds in liquid argon are as yet unknown, and a huge exposure ($>500\,\mathrm{kt} \cdot \mathrm{years}$) would likely be required for observation. With tight control of backgrounds, DUNE — in the long term — could play a unique and complementary role in the physics of relic neutrinos.

Background is a serious issue for DSNB detection. The solar *hep* neutrinos, which have an endpoint at $18.8\,\mathrm{MeV}$, will determine the lower bound of the DSNB search window ($\sim 16\,\mathrm{MeV}$). The upper bound is determined by the atmospheric ν_e flux and is around $40\,\mathrm{MeV}$. Although the LArTPC provides a unique sensitivity to the electron-neutrino component of the DSNB flux, early studies indicate that due to this lower bound of $\sim 16\,\mathrm{MeV}$, DUNE would need a huge mass of liquid argon — of order $100\,\mathrm{kt}$ — to get more than 4σ evidence for the diffuse supernova flux in five years [173]. The expected number of relic supernova neutrinos, N_{DSNB}, that could be observed in a $40-\mathrm{kt}$ LArTPC detector in ten years [173] assuming normal hierarchy is:

$$N_{\mathrm{DSNB}} = 46 \pm 10 \quad 16\,\mathrm{MeV} \leq E_e \leq 40\,\mathrm{MeV} \tag{5.3}$$

where E_e is the energy of the electron from the CC interaction as shown in Equation 5.2.

The main challenge for detection of such a low rate of relic neutrinos in a LArTPC is understanding how much of the large spallation background from cosmic-ray interactions with the heavy argon nucleus leaks into the search window. Some studies have been done [174] but more work is needed.

5.4.3 Other Low-Energy Neutrino Sources

We note some other potential sources of signals in the tens-of-MeV range that may be observable in DUNE. These include neutrinos from accretion disks [175] and black-hole/neutron star mergers [176]. These will create spectra not unlike those from core-collapse events, and with potentially large fluxes. However they are expected to be considerably rarer than core-collapse supernovae within an observable distance range. There may also be signatures of dark-matter WIMP annihilations in the low-energy signal range [177, 178].

5.5 Detector Requirements

For supernova burst physics, the detector must be able to detect and reconstruct events in the range 5–100 MeV. As for proton decay and atmospheric neutrinos, no beam trigger will be available; therefore there must be special triggering and DAQ requirements that take into account the short, intense nature of the burst, and the need for prompt propagation of information in a worldwide context. The DUNE Far Detector Requirements [85] specific to supernova burst neutrinos are as follows:

- Far Detector Depth: The signal to background ratio shall be sufficiently large to identify the burst (<100 seconds) from a core-collapse supernova within 20 kpc (within the Milky Way). This will require a detector located at sufficient depth for cosmic-ray-related background, including spallation-induced events, to be sufficiently low. Furthermore, backgrounds from radioactivity or other sources must also be sufficiently low. Preliminary studies [179] indicate that backgrounds at 4850 ft (including both cosmogenics and intrinsic radioactivity) will be sufficiently low, although more work is needed.

- Far Detector Triggering and DAQ: The far detector shall be capable of collecting information for a supernova burst within the Milky Way. Events are expected within a time window of approximately 10 seconds, but possibly over an interval as long as several tens of seconds; a large fraction of the events are expected within approximately the first second of the burst. The data acquisition buffers shall be sufficiently large and the data acquisition system sufficiently robust to allow full capture of neutrino event information for a supernova as close as 0.1 kpc. At 10 kpc, one expects thousands of events within approximately 10 seconds, but a supernova at a distance of less than 1 kpc would result in $10^5 - 10^7$ events over 10 seconds.

  The far detector shall have high uptime (>90%) with little event-by-event deadtime to allow the capture of low-probability astrophysical events that could occur at any time with no external trigger. Supernova events are expected to occur a few times per century within the Milky Way galaxy. For any 10-year period, the probability of a supernova could be 20 to 30%. Capturing such an event at the same time as many of the other detectors around the Earth is very important.

  The DUNE detector systems shall be configured to provide information to other observatories on possible astrophysical events (such as a galactic supernova) in a short enough time to allow global coordination. To obtain maximum scientific value out of a singular astronomical event, it is very important to inform all other observatories (including optical ones) immediately, so that they can begin observation of the evolution of the event.

- Far Detector Event Reconstruction: The far detector shall be capable of collecting low energy (<100 MeV) charged-current electron neutrino interactions on ^{40}Ar nuclei that arrive in a short period of time. The final-state electron (or positron) shall be detected and its energy measured. An energy threshold of 5 MeV or better is highly desirable; most supernova burst events are expected to have energy depositions in the range 5–50 MeV. Energy and event time resolution must be sufficient to resolve interesting physics features of the burst. Preliminary studies suggest that resolution measured by Icarus for low-energy events [124]

should be adequate, and that approximately millisecond event time resolution should be sufficient to resolve features such as the neutronization burst and the preceding short notch due to neutrino trapping in the ν_e spectrum (see the luminosity curve of Figure 5.3), given adequate statistics.

Detection of gamma ray photons from the final-state excited nucleus could lead to additional electronics requirements.

The other low-energy physics described in Section 5.4 typically requires event reconstruction capabilities similar to supernova-burst physics; however, background requirements are much more stringent for these (especially for DSNB). Realistic background conditions in the few-tens-of-MeV range are not currently very well understood. These physics topics do not drive detector requirements, although it may still be possible for DUNE to address them if backgrounds can be kept sufficiently well under control.

Chapter 6

Near Detector Physics

6.1 Introduction and Motivation

The LBNF neutrino beam used to study neutrino oscillations in DUNE is an extended source at the near site, therefore every single spectrum induced by the neutrino charged (CC) and neutral (NC) current interactions — ν_μ-CC, $\bar{\nu}_\mu$-CC, ν_e-CC, $\bar{\nu}_e$-CC, and the NC — is different when measured at the far detector versus the near detector. In order to achieve the systematic precision for the signal and background events in the far detector, which ideally should always be lower than the corresponding statistical error, the near detector measurements — including neutrino fluxes, cross sections, topology of interactions and smearing effects — must be unfolded and extrapolated to the far detector location. The charge, ID, and the momentum vector resolution of particles produced in the neutrino interactions are key to constraining the systematic uncertainties in the predictions at far detector.

To this end, it is useful to recall that for the LBNF low-energy reference beam (80-GeV protons, 1.07 MW, 1.47×10^{21} POT/year), the event rates expected at the 40-kt far detector per year are 2900 (1000) for the $\nu_\mu(\bar{\nu}_\mu)$ disappearance channel and 230 (45) for the $\nu_e(\bar{\nu}_e)$ appearance channel (for $\delta_{CP} = 0$, normal hierarchy and assumed best fit values of the mass-squared differences and mixings). For comparison, the raw event rates per ton of near detector target mass (without detector effects) for various neutrino interactions in the near detector at 574 m from the proton beam target are summarized in Table 6.1. The rates are indicated for a ton of target mass of Ar (Carbon) per 10^{20} protons-on-target. The mass of Ar in the near detector targets is required to have sufficient mass to provide $\times$ 10 the statistics of the far detector. Although the Ar-target design is preliminary, the Ar mass is expected to be approximately 100kg.

Importantly, given the scale and ambition of LBNF/DUNE, the near detector must offer a physics potential that is as rich as those offered by collider detectors. One of the main advantages of a high-resolution near detector built according to the reference design (detailed in Volume 4, Chapter 7 of this CDR) is that it will offer a rich panoply of physics spanning an estimated 100 topics and resulting in over 200 publications and theses during a ten-year operation.

Table 6.1: Estimated interaction rates on Ar (Carbon) in the neutrino (second column) and antineutrino (third column) beams per ton of detector for 1×10^{20} POT at 574 m assuming neutrino cross-section predictions from GENIE [180] and a $120-$GeV proton beam using the optimized design (Section 3.7.2). Processes are defined at the initial neutrino interaction vertex and thus do not include final-state effects. These estimates do not include detector efficiencies or acceptance [181, 182].

Production mode	ν_μ Events on Ar (Carbon)	$\overline{\nu}_\mu$ Events on Ar (Carbon)
CC QE ($\nu_\mu n \to \mu^- p$)	30,000 (28,000)	13,000 (15,000)
NC elastic ($\nu_\mu N \to \nu_\mu N$)	11,000 (11,000)	6,700 (68,00)
CC resonant ($\nu_\mu p \to \mu^- p\pi^+$)	21,000 (24,000)	0 (0)
CC resonant ($\nu_\mu n \to \mu^- n\pi^+ (p\pi^0)$)	23,000 (21,000)	0 (0)
CC resonant ($\bar{\nu}_\mu p \to \mu^+ p\pi^- (n\pi^0)$)	0 (0)	83,00 (7,800)
CC resonant ($\bar{\nu}_\mu n \to \mu^+ n\pi^-$)	0 (0)	12,000 (8,100)
NC resonant ($\nu_\mu p \to \nu_\mu p\pi^0 (n\pi^+)$)	7,000 (9,200)	0 (0)
NC resonant ($\nu_\mu n \to \nu_\mu n\pi^+ (p\pi^0)$)	9,000 (11,000)	0 (0)
NC resonant ($\bar{\nu}_\mu p \to \bar{\nu}_\mu p\pi^- (n\pi^0)$)	0 (0)	3,900 (4,300)
NC resonant ($\bar{\nu}_\mu n \to \bar{\nu}_\mu n\pi^-$)	0 (0)	4,700 (4,300)
CC DIS ($\nu_\mu N \to \mu^- X$ or $\bar{\nu}_\mu N \to \mu^+ X$)	95,000 (92,000)	24,000 (25,000)
NC DIS ($\nu_\mu N \to \nu_\mu X$ or $\bar{\nu}_\mu N \to \bar{\nu}_\mu X$)	31,000 (31,000)	10,000 (10,000)
CC coherent π^+ ($\nu_\mu A \to \mu^- A\pi^+$)	930 (1,500)	0 (0)
CC coherent π^- ($\bar{\nu}_\mu A \to \mu^+ A\pi^-$)	0 (0)	800 (1,300)
NC coherent π^0 ($\nu_\mu A \to \nu_\mu A\pi^0$ or $\bar{\nu}_\mu A \to \bar{\nu}_\mu A\pi^0$)	520 (840)	450 (720)
NC elastic electron ($\nu_\mu e^- \to \nu_\mu e^-$ or $\bar{\nu}_\mu e^- \to \overline{\nu_\mu} e^-$)	16 (18)	11 (12)
Inverse Muon Decay ($\nu_\mu e \to \mu^- \nu_e$)	9.5 (11)	0 (0)
Total CC	170,000 (170,000)	59,000 (61,000)
Total NC+CC	230,000 (230,000)	84,000 (87,000)

6.2 Physics Goals of the Near Detector

The physics goals of the DUNE near detector fall under three categories:

- constraining the systematic uncertainties in oscillation studies

- offering a generational advance in the precision measurements of neutrino interactions, e.g., cross sections, exclusive processes, electroweak and isospin physics, structure of nucleons and nuclei

- conducting searches for new physics covering unexplored regions, including heavy (sterile) neutrinos, large Δm^2 neutrino oscillations, light Dark Matter candidates, etc.

These three broad goals possess significant synergy. The physics requirements for the near detector are driven by the oscillation physics. However, the unprecedented neutrino fluxes available at LBNF and the challenging constraints required by the long-baseline program, especially those related to the CP measurement, also make the near detector imminently suitable for short-baseline precision physics. And conversely, conducting precision measurements of neutrino interactions will actually result in a reduction of systematic uncertainties on signal and background predictions in the far detector [183, 184, 19].

6.3 The Role of the Near Detector in Oscillation Physics

As illustrated in Chapter 3, studies on the impact of different levels of systematic uncertainties on the oscillation analysis indicate that uncertainties exceeding 1% for signal and 5% for backgrounds may result in substantial degradation of the sensitivity to CP violation and mass hierarchy. The near detector physics measurements discussed in this section are needed in order to match this level of systematic uncertainty.

The near detector will need to determine the relative abundance and energy spectrum of all *four* species of neutrinos in the LBNE beam. This requires measurement of ν_μ, $\bar{\nu}_\mu$, ν_e, and $\bar{\nu}_e$ via their CC-interactions, which in turn demands precise measurement of μ^-, μ^+, e^-, and e^+ in the near detector. Specifically, to measure both the small ν_e and $\bar{\nu}_e$ contamination in the beam with high precision, the detector would need to be able to distinguish e^+ from e^-. This last requirement is motivated by

1. the need to measure and identify $\nu - e$ NC elastic scattering (and calibrate the corresponding backgrounds) for the absolute flux measurements

2. the redundancy in determining the momentum distributions of the neutrinos' parent mesons, in particular, the K^0 mesons using $\bar{\nu}_e$-events, which are essential ingredients for predicting the far detector/near detector flux ratio as a function of energy

3. the measurement of the π^0 yield in CC and NC interactions from converted photons

4. the different composition in terms of QE, single-pion resonance, multi-pion resonance, and deep inelastic scattering (DIS) of CC and NC events originated by each of the four species in the far detector and near detector, respectively

Quantifying asymmetries between neutrinos and antineutrinos, such as energy scales and interaction topologies, which are relevant for the measurement of the CP-violating phase, is another job of the near detector. Since the reference near neutrino detector, the fine-grained tracker (FGT), is not identical to the far detector, it is not possible in long-baseline analyses to "cancel" the event reconstruction errors in a near-to-far ratio. The extent to which such a cancellation will limit the ultimate precision of the experiment has yet to be fully explored. Because of the low average density of the FGT (0.1 g/cm^3), however, DUNE will be able to measure the missing transverse momentum (p_T) vector in the CC processes, in addition to accurately measuring the lepton and hadron energies. This redundant missing-p_T vector measurement provides a most important constraint on the neutrino and antineutrino energy scales. Measurements of exclusive topologies like quasi-elastic, resonance and coherent meson production offer additional constraints on the neutrino energy scale.

In the disappearance studies, the absolute ν_μ- and $\bar{\nu}_\mu$ flux should be determined to $\simeq 3\%$ precision in $0.5 \leq E_\nu \leq 8$ GeV so as to eliminate uncertainties in the neutrino and antineutrino cross sections affecting the oscillation measurements. For precision measurements of electroweak and QCD physics, a similar precision is required at higher energies.

For precision ν_μ- and $\bar{\nu}_\mu$-disappearance channels, the far detector/near detector ratio of the number of neutrinos (ν_μ and $\bar{\nu}_\mu$) at a given E_ν bin in $0.5 \leq E_\nu \leq 8$ GeV range should be known to $\simeq 1-2\%$ precision. The capability to precisely measure the muon momenta and the low-hadronic energy of the near detector will enable this precision.

NC processes constitute one of the largest backgrounds to all appearance and disappearance oscillation channels. It is therefore important for the near detector to make a precise measurement of the NC cross section relative to CC as a function of the hadronic energy, E_{Had}.

A precise measurement of π^0 and photon yields by the near detector in *both* ν-induced NC and CC interactions is essential; this is the most important background to the ν_e- and $\bar{\nu}_e$ appearance at low energies.

The $\pi^\pm$ content in CC and NC hadronic jets is the most important background to the ν_μ- and $\bar{\nu}_\mu$ disappearance coming from the hadronic $\pi^\pm \to \mu^\pm$; it can also be a background to the appearance channel at lower energies. By separately measuring the momenta of π^+ and π^- produced in each of the CC- and NC-induced hadronic shower, the ND will in situ measure the $\pi^\pm$ content in CC and NC events, and hence the corresponding backgrounds to the disappearance signal.

Precise near detector measurements leading to characterization of various exclusive (semi-exclusive) channels such as Quasi-Elastic (QE), resonance (Res), coherent-mesons and Deep-Inelastic-Scattering (DIS) will yield in situ constraints on the nuclear effects from both initial and final interaction (FSI).

The near detector will quantify the neutrino-argon cross section by measuring interactions off Ar, Ca, C, H, etc. targets. The goal is to provide a consistent model, as opposed to an empirical parameterization, for the nuclear effects.

Finally, the near detector will constrain NC and CC backgrounds to the $\tau-$ appearance in the far detector. One of the unique capabilities of the liquid argon (LAr) far-detector is identification of the tau appearance with high fidelity. The ND measurements would considerably reduce the error in the production of the tau-lepton (large x_{BJ} data) and would constrain the backgrounds that mimic the tau signal.

The above requirements suggest a high-resolution, magnetized near detector for identifying and measuring e^+, e^-, μ^-, μ^+, π^0, $\pi^{+,-}$ and protons with high efficiency.

6.4   Precision Measurements at the Near Detector

Over a five-year run in neutrino mode, the intense neutrino source at LBNF will provide $\mathcal{O}(100)$ million neutrino interactions in a 7-t near detector; and about 0.4 times as many in antineutrino mode. The high-resolution, fine-grained near detector described in Volume 4: *The DUNE Detectors at LBNF* would offer not only the requisite systematic precision for oscillation studies, but also a generational advance in the precision measurements and unique searches that a neutrino beam can provide. This section outlines the salient physics reach of this detector; further details can be found in [184] and [19]. Discussed first are precision measurements that would support and impact the oscillation physics program, followed by examples of other non-oscillation-related physics measurements that would extend our knowledge of important aspects of particle physics.

6.4.1   Precision Measurements Related to Oscillation Physics

Using ν-electron NC scattering, the absolute neutrino flux can be determined to $\leq 3\%$ precision in the range $0.5 \leq E_\nu \leq 10$ GeV. Additionally, the ν-electron CC scattering leading to inverse muon decay would determine the absolute flux to $\simeq 3\%$ precision in $E_\nu \geq 20$ GeV region [185]. The DUNE near detector's ability to determine the background (primarily from ν_μ quasi-elastic scattering) to inverse muon decay *without* relying on $\bar{\nu}_\mu$ measurements or ad hoc extrapolations, such as made in CCFR [186], [187] and CHARM [188], allows such precisions, which are dominated by statistics. Importantly, the ability to extract the quasi-elastic $\bar{\nu}_\mu$-H interaction, via subtraction of hydrocarbon and pure carbon targets, would allow an extraction of the $\bar{\nu}_\mu$ absolute flux to a few percent precision. Furthermore, novel techniques such as the use of coherent-ρ meson production in the near detector combined with photo-production could provide a constraint on the absolute flux to $\simeq 5\%$ in the intermediate $5 \leq E_\nu \leq 20$ GeV region. We note that this near detector will be the first to in-situ-constrain the absolute flux to a level approaching $\sim 2.5\%$ precision.

The most promising method of determining the shape of ν_μ and $\bar{\nu}_\mu$ flux is by measuring the low-hadronic energy CC, the Low-ν_0 method [189]. The method, when combined with the empirical

parameterization of the $\pi^{\pm}$, $K^{\pm}$, and such hadroproduction data as would be available in the coming decade, permits a bin-to-bin precision of 1–2% on the flux spanning $1 \leq E_{\nu} \leq 50$ GeV. Recent model calculations by Bodek et al. [190] confirm these error estimates. Specifically, for the ν_{μ} and $\bar{\nu}_{\mu}$ disappearance the Low-ν_0 method would predict the far detector/near detector(E_{ν}) to 1–2% precision.

By precisely measuring the ν_{μ}-, $\bar{\nu}_{\mu}$-, ν_e-, $\bar{\nu}_e$-CC, the near detector will decompose the π^+, K^+, π^-, K^-, μ^+, μ^-, and K_L^0 contents of the beam, thus allowing a precise far detector/near detector(E_{ν}) prediction to a few percent. This ability lends a unique power to not only measure the cross sections of all four neutrino species, but also to allow sensitive searches for new physics, e.g., violation of universality and large-$\Delta \mathrm{m}^2$ oscillations, as discussed below.

For the δ_{CP} in particular, the near detector measurements would constrain the ν_e/ν_{μ} to $< 1\%$ and $\bar{\nu}_e/\bar{\nu}_{\mu}$ to $\simeq 1\%$ precision, thereby vastly reducing the associated error.

The high resolution measurements of E_{μ} and E_e and those of charged hadrons and the reconstruction of about one million K_S^0 and several million π^0 will provide a tight constraint on the (anti)neutrino energy scale. However, nuclear physics, including initial and final state interactions, affects the E_{ν}-scale and can affect ν differently from $\bar{\nu}$ interactions thus producing a spurious contribution to any measured CP-violating observable. The unique experimental handle on these seemingly intractable effects comes from a precise measurement of the missing transverse momentum **vector**, P_T^m afforded by the high-resolution near detector.

The ability to determine P_T^m affords an event-by-event identification of NC events. This is particularly crucial in order to decompose the background contributions to the ν_e or $\bar{\nu}_e$ appearance and the disappearance measurements.

The yields and momentum vector measurements of π^0, π^+, π^-, K^+, K^-, proton, K_S^0 and Λ particles in CC and NC, as a function of visible energy, will provide an "event generator" *measurement* for the far detector and constrain the "hadronization" error to $\leq 2.5\%$ associated with the far detector prediction.

In any long-baseline neutrino oscillation program, including LBNF/DUNE, the quasi-elastic (QE) interactions are special. First, the QE cross section is substantial, especially at the second oscillation maximum. Second, because of the simple topology — a muon and a proton — QE provides, to first order, a close approximation to E_{ν}. Precise momentum measurements of this two-track topology impose direct constraints on nuclear effects associated with both initial and final state interactions.

Resonance is the second most dominant interaction mode, besides deep inelastic scattering (DIS), in the LBNF/DUNE oscillation range, $0.5 \leq E_{\nu} \leq 10$ GeV. By measuring the complete topology of resonance, a high-resolution near detector will offer an unprecedented precision on the resonance cross section, and will provide in situ constraints on the nuclear effects.

Precision measurements of structure functions and differential cross sections would directly affect the oscillation measurements by providing accurate simulations of neutrino interactions. They would also offer measure of that background processes that are dependent upon the angular dis-

tribution of the outgoing lepton, i.e. x_{BJ}-distribution, in the far detector. Furthermore, the differential cross section measurements at the ND would constitute one of the most important ingredients to the 'QCD-fitting' enterprise: extraction of the parton distribution functions (PDF), benefiting not only neutrino physics but also hadron-collider analyses. Under the rubric of nucleon structure and QCD, the topics include:

1. Measurement of form factors and structure functions

2. QCD analysis, tests of perturbative QCD and quantitating the non-perturbative QCD effects

3. d/u Parton distribution functions at large x, which is the limiting error in the ν_τ-CC measurements/searches at the far detector

4. Sum rules and the strong coupling constant; and v) Quark-hadron duality

An integral part of the near detector physics program is a set of detailed measurements of (anti)neutrino interactions in argon and in a variety of nuclear targets including calcium, carbon, hydrogen (via subtraction), and steel. The goals are twofold, (1) obtain a model-independent direct measurement of nuclear effects in Ar using the FGT's ability to isolate $\nu(\bar{\nu})$ interactions off free hydrogen via subtraction of hydrocarbon and carbon targets; and (2) measure the neutrino-nuclear interactions so as to allow an accurate modeling of initial and final state effects. The studies would include the nuclear modification of form factors and structure functions, effects in coherent and incoherent regimes, nuclear dependence of exclusive and semi-exclusive processes, and nuclear effects including short-range correlations, pion-exchange currents, pion absorption, shadowing, initial-state interactions and final-state interactions.

6.4.2   Other Precision Measurements

Neutrinos and antineutrinos are the most effective probes for investigating electroweak physics. Interest in a precise determination of the weak mixing angle ($\sin^2 \theta_W$) at DUNE energies via neutrino scattering is twofold: (1) it provides a direct measurement of neutrino couplings to the Z boson, and (2) it probes a different scale of momentum transfer than LEP did by virtue of not being at the Z boson mass peak. The weak mixing angle can be extracted experimentally from several independent NC physics processes: (1) deep inelastic scattering off quarks inside nucleons: $\nu N \to \nu X$; (2) elastic scattering off electrons: $\nu e^- \to \nu e^-$; (3) elastic scattering off protons: $\nu p \to \nu p$; iv) coherent ρ^0 meson production. Note that these processes involve substantially different scales of momentum transfer, providing a tool to test the running of $\sin^2 \theta_W$ within a single experiment.

The most sensitive channel for $\sin^2 \theta_W$ in the DUNE near detector is expected to be the νN DIS through a precision measurement of the NC/CC cross-section ratio. This measurement will be dominated by systematic uncertainties, which can be accurately constrained by dedicated in situ measurements using the large CC samples and employing corresponding improvements in theory that will have evolved over the course of the experiment. Using the existing knowledge of structure functions and cross-sections we expect a relative precision of about 0.35% on $\sin^2 \theta_W$,

with the default low-energy LBNF beam. An increase of the fluxes with a beam upgrade and/or a one year run with a high energy tuning of the neutrino spectrum would allow a substantial reduction of uncertainties down to about 0.2%. This level of precision is comparable to colliders (LEP) and offers a shot at discovery.

The various independent channels measured in the DUNE near detector can be combined though global electroweak fits, further optimizing the sensitivity to electroweak parameters. The level of precision achievable as well as the richness of the physics measurements put the DUNE near detector electroweak program on par with the gold standard electroweak measurements at LEP.

One of the most compelling physics topics accessible to the DUNE-near detector in the LBNF-beam is the isospin physics using neutrino and antineutrino interactions. Given the statistics and a commensurate resolution of near detector, for the first time we have a chance to test the Adler sum-rule to a few percent level, and perhaps claim a discovery. Precision test of sum-rules is a rich ground for finding something new, refuting the prevalent wisdom. An added motivation is the possibility of isospin asymmetry in nucleons .

To accomplish this, neutrino and anti-neutrino scattering off hydrogen is needed. Whereas the Adler sum rule is the prize, the $\bar{\nu}_\mu$-H and ν_μ-H scattering will provide (a) the absolute flux normalization via low-Q^2 $\bar{\nu}_\mu$-QE interactions, and (b) will be crucial to achieve a model-independent measurement of nuclear effects in the neutrino-nuclear interactions.

The question of whether strange quarks contribute substantially to the vector and axial-vector currents of the nucleon remains unresolved. A large observed value of the strange-quark contribution to the nucleon spin (axial current), Δs, would enhance our understanding of the proton structure.

The strange *axial vector* form factors are poorly determined. The most direct measurement of Δs, which does not rely on the difficult measurements of the g_1 structure function at very small values of the Bjorken variable x, can be obtained from (anti)neutrino NC elastic scattering off protons.

The low-density magnetized tracker in DUNE near detector can provide a good proton reconstruction efficiency as well as high resolution on both the proton angle and energy, down to $Q^2 \sim 0.07$ GeV^2. This capability will reduce the uncertainties in the extrapolation of the form factors to the limit $Q^2 \rightarrow 0$. About $2.0(1.2) \times 10^6$ $\nu p(\bar{\nu} p)$ events are expected after the selection cuts in the low-density tracker, yielding a statistical precision on the order of 0.1%.

6.5   New Physics Searches

A search for heavy neutrinos is intriguing. The most economic way to handle the problems of neutrino masses, dark matter and baryon asymmetry of the universe in a unified way may be to add to the SM three Majorana singlet fermions with masses roughly on the order of the masses of known quarks and leptons. The lightest of the three new leptons is expected to have a mass from 1 keV to 50 keV and play the role of the Dark Matter particle (for details and additional references, see [184] and [19]).

The most effective mechanism of sterile neutrino production is through weak two body and three body decays of heavy mesons and baryons. In the search for heavy neutrinos, the strength of the proposed high-resolution near detector, compared to earlier experiments lies in reconstructing the exclusive decay modes, including electronic, hadronic and muonic channels. Furthermore, the detector provides a means to constrain and measure the backgrounds using control samples. Preliminary investigations of these issues are ongoing and suggest that the FGT will have an order of magnitude higher sensitivity in exclusive channels than previous experiments did.

The near detector could potentially search for large Δm^2 oscillations. As has become evident over the past decade or more, there may be evidence from several distinct experiments that points towards the existence of sterile neutrinos with mass in the range 1 eV^2 (for details and additional references, see [184] and [19]). A short-baseline neutrino program has been initiated at Fermilab and elsewhere to clear the questions raised by these varying pieces of evidence.

Since the DUNE near detector is located at a baseline of several hundred meters and uses the LE beam, it has values of $L/E \sim 1$, which render it sensitive to these oscillations — if they exist. Due to the differences between neutrinos and antineutrinos, four possibilities have to be considered in the analysis: ν_μ disappearance, $\bar\nu_\mu$ disappearance, ν_e appearance and $\bar\nu_e$ appearance. It must be noted that the search for the high Δm^2 oscillations must be performed simultaneously with the in situ determination of the fluxes. To this end, it is necessary to obtain an independent prediction of the ν_e and $\bar\nu_e$ fluxes starting from the measured ν_μ and $\bar\nu_\mu$ CC distributions, since the ν_e and $\bar\nu_e$ CC distributions could be distorted by the appearance signal. An iterative procedure has been developed to handle this, details of which can be found in [184] and [19].

Recently, a great deal of interest has been generated in searching for DM at low-energy, fixed-target experiments. High-flux neutrino beam experiments, as DUNE is planned to be, have been shown to provide coverage of the DM and DM-mediator parameter space that can be covered by neither direct detection nor collider experiments. Upon striking the target, the proton beam can produce dark photons either directly through $pp(pn) \rightarrow \mathbf{V}$ or indirectly through the production of a π^0 or a η meson which then promptly decays into a SM photon and a dark photon. For the case of $m_V \geq 2m_{DM}$, the dark photons will quickly decay into a pair of DM particles. These relativistic DM particles from the beam will travel along with the neutrinos to the DUNE near detector. The DM particles can then be detected through neutral-current-like interactions either with electrons or nucleons in the detector.

Since the signature of DM events looks just like those of the neutrinos, the neutrino beam provides the major source of background for the DM signal. Several ways have been proposed to suppress neutrino backgrounds by using the unique characteristics of the DM beam. Since DM, due to much higher mass, will travel much more slowly than the neutrinos, the timing in the near detector becomes a discriminator. In addition, since the electrons struck by DM will be much more forward in direction, the angles of these electrons may be used to reduce backgrounds, taking advantage of the fine angular resolution of the DUNE near detector. Finally, a special run can be devised to turn off the focusing horn to significantly reduce the charged particle flux that will produce neutrinos. Further studies are required to determine appropriate hardware-parameter choices that could benefit these searches, including granularity, absorbers, timing resolution, DAQ-speed, etc. Studies are also required to determine if DUNE will effectively cover the important region in

parameter space between the MiniBooNE exclusion and the direct detection region of the most popular candidates.

DUNE will be the first long-baseline experiment possessing a large statistics of high-energy ν_μ, $\bar{\nu}_\mu$, and $\nu_e + \bar{\nu}_e$ CC and NC events measured with high precision in the liquid argon far detector. An obvious venue for discovery is to search for distortion at energies greater than 10 GeV, not envisioned by the PMNS mixing.

DUNE will also be the first long-baseline experiment with the capability to reconstruct ν_τ-appearance with high statistics. The paucity of measured ν_τ-CC motivates searching for new physics. The role of near detector — where no τ is expected — will be to accurately "calibrate" background topologies in the NC and CC interactions, most notably at large x_{bj}.

6.6 Summary

The DUNE near detector, as embodied in the FGT reference design, will offer a rich physics portfolio that will not only support and buttress the oscillation program at the far detector, but also extend our knowledge of fundamental interactions and the structure of nucleons and nuclei, possibly leading to the discovery of new phenomena. It will do so by providing tracking of charged particles at levels of a precision unattained by previous experiments. In the above, we have tried to summarize these capabilities and provide a glimpse of its impact on the overall DUNE physics program.

Chapter 7

Summary of Physics

The primary science goals of DUNE are drivers for the advancement of particle physics. The questions being addressed are of wide-ranging consequence: the origin of flavor and the generation structure of the fermions (i.e., the existence of three families of quark and lepton flavors), the physical mechanism that provides the CP violation needed to generate the Baryon Asymmetry of the Universe, and the high energy physics that would lead to the instability of matter. Achieving these goals requires a dedicated, ambitious and long-term program.

Observation of $\mathcal{O}(1000)$ $\nu_\mu \to \nu_e$ events in the DUNE LArTPCs can be achieved with moderate exposures of around $300 \text{ kt} \cdot \text{MW} \cdot \text{year}$, depending on the beamline design. When coupled with a highly capable near detector and sophisticated analysis techniques to control systematics to a few percent, this level of statistics will enable discovery (5σ) of CP violation if it is near maximal, and an unambiguous highly precise measurement of the mass hierarchy for all possible values of δ_{CP}. With an optimized beam design, a precision of $10°$ on $\delta_{\text{CP}} = 0$ is also achievable with this level of exposure. Exposures of 850 to $1320 \text{ kt} \cdot \text{MW} \cdot \text{year}$ (depending on the beam design) would be needed to reach 3σ sensitivity to CP violation for 75% of all values of δ_{CP} — the goal set by the P5 advisory panel. The example staging plan for DUNE, detailed in Chapter 2 of Volume 1: *The LBNF and DUNE Projects*, would enable DUNE to meet the P5 goal in less than 14 years with an optimized beam design. It is important to note that exposures in the range of 100–$160 \text{ kt} \cdot \text{MW} \cdot \text{year}$ are sufficient to find evidence (3σ) for CP violation if it is near maximal. These exposures are consistent with the minimal requirement of achieving $120 \text{ kt} \cdot \text{MW} \cdot \text{year}$ set by P5. No experiment can provide 100% coverage of δ_{CP} values, since CP violation effects vanish as $\delta_{\text{CP}} \to 0$ or π. Higher exposures — with more detector mass or higher proton beam power — will enable high precision probes of the three-flavor model of neutrino mixing, improving sensitivities to new effects including the presence of sterile neutrinos and non-standard interactions.

The DUNE far detector will significantly extend lifetime sensitivity for specific nucleon decay modes by virtue of its high detection efficiency relative to water Cherenkov detectors and its low background rates. As an example, DUNE has enhanced capability for detecting the $p \to K^+\overline{\nu}$ channel, where lifetime predictions from supersymmetric models extend beyond, but remain close to, the current (preliminary) Super-Kamiokande limit of $\tau/B > 5.9 \times 10^{33}$ year (90% CL). Supersymmetric GUT models in which the $p \to K^+\overline{\nu}$ channel mode is dominant also favor other

modes involving kaons in the final state, thus enabling a rich program of searches for nucleon decay in the DUNE LArTPC detectors.

In a core-collapse supernova, over 99% of all gravitational binding energy of the $1.4 M_\odot$ collapsed core — some 10% of its rest mass — is emitted in neutrinos. The neutrinos are emitted in a burst of a few tens of seconds duration, with about half in the first second. Energies are in the range of a few tens of MeV, and the luminosity is divided roughly equally between the three known neutrino flavors. Compared to existing water Cerenkov detectors, liquid argon has a unique sensitivity to the electron-neutrino (ν_e) component of the flux, via the absorption interaction on ^{40}Ar. The ν_e component of the flux dominates the very early stages of the core-collapse, including the "neutronization" burst. The observation of the neutrino signal from a core-collapse supernova in the DUNE LArTPCs will thus provide unique and unprecedented information on the mechanics of supernovas, in addition to enabling the search for new physics. The sensitivity of the DUNE LArTPCs to low energy ν_e will also enable unique measurements with other astrophysical neutrinos, such as solar neutrinos.

A highly capable near neutrino detector is required to provide precision measurements of neutrino interactions, which in the medium to long term are essential for controlling the systematic uncertainties in the long-baseline oscillation physics program. Furthermore, since the near detector data will feature very large samples of events that are amenable to precision reconstruction and analysis, they can be exploited for sensitive studies of electroweak physics and nucleon structure, as well as for searches for new physics in unexplored regions (heavy sterile neutrinos, high-Δm^2 oscillations, light Dark Matter particles, and so on).

The DUNE experiment is a world-leading international physics experiment, bringing together the world's neutrino community as well as leading experts in nucleon decay and particle astrophysics, to explore key questions at the forefront of particle physics and astrophysics. The highly capable beam and detectors will enable a large suite of new physics measurements with potential groundbreaking discoveries.

References

[1] Particle Physics Project Prioritization Panel, "US Particle Physics: Scientific Opportunities; A Strategic Plan for the Next Ten Years," 2008. `http://science.energy.gov/~/media/hep/pdf/files/pdfs/p5_report_06022008.pdf`.

[2] `http://espp2012.ifj.edu.pl/index.php`.

[3] J. Schechter and J. Valle, "Neutrino Masses in SU(2) x U(1) Theories," *Phys.Rev.*, vol. D22, p. 2227, 1980.

[4] M. Gonzalez-Garcia, M. Maltoni, and T. Schwetz, "Updated fit to three neutrino mixing: status of leptonic CP violation," *JHEP*, vol. 1411, p. 052, 2014.

[5] F. Capozzi, G. Fogli, E. Lisi, A. Marrone, D. Montanino, *et al.*, "Status of three-neutrino oscillation parameters, circa 2013," *Phys.Rev.*, vol. D89, no. 9, p. 093018, 2014.

[6] D. Forero, M. Tortola, and J. Valle, "Neutrino oscillations refitted," *Phys.Rev.*, vol. D90, no. 9, p. 093006, 2014.

[7] S. F. King, A. Merle, S. Morisi, Y. Shimizu, and M. Tanimoto, "Neutrino Mass and Mixing: from Theory to Experiment," *New J.Phys.*, vol. 16, p. 045018, 2014.

[8] A. de Gouvea *et al.*, "Working Group Report: Neutrinos." arXiv:1310.4340 [hep-ex], 2013.

[9] S. Boucenna, S. Morisi, M. Tortola, and J. Valle, "Bi-large neutrino mixing and the Cabibbo angle," *Phys.Rev.*, vol. D86, p. 051301, 2012.

[10] P. Harrison, D. Perkins, and W. Scott, "Tri-bimaximal mixing and the neutrino oscillation data," *Phys.Lett.*, vol. B530, p. 167, 2002.

[11] R. Mohapatra, S. Antusch, K. Babu, G. Barenboim, M.-C. Chen, *et al.*, "Theory of neutrinos: A White paper," *Rept.Prog.Phys.*, vol. 70, pp. 1757–1867, 2007.

[12] C. H. Albright and M.-C. Chen, "Model Predictions for Neutrino Oscillation Parameters," *Phys.Rev.*, vol. D74, p. 113006, 2006.

[13] H. Nunokawa, S. J. Parke, and J. W. Valle, "CP Violation and Neutrino Oscillations," *Prog.Part.Nucl.Phys.*, vol. 60, pp. 338–402, 2008.

[14] M. Bass *et al.*, "Baseline optimization for the measurement of CP violation, mass hierarchy, and θ_{23} octant in a long-baseline neutrino oscillation experiment," *Phys.Rev.*, vol. D91, no. 5, p. 052015, 2015.

[15] M. V. Diwan, "The Case for a super neutrino beam," *Frascati Phys. Ser.*, vol. 35, pp. 89–109, 2004. [,89(2004)].

[16] M. V. Diwan *et al.*, "Very long baseline neutrino oscillation experiments for precise measurements of mixing parameters and CP violating effects," *Phys. Rev.*, vol. D68, p. 012002, 2003.

[17] P. Huber, M. Lindner, and W. Winter, "Simulation of long-baseline neutrino oscillation experiments with GLoBES (General Long Baseline Experiment Simulator)," *Comput.Phys.Commun.*, vol. 167, p. 195, 2005.

[18] P. Huber, J. Kopp, M. Lindner, M. Rolinec, and W. Winter, "New features in the simulation of neutrino oscillation experiments with GLoBES 3.0: General Long Baseline Experiment Simulator," *Comput.Phys.Commun.*, vol. 177, pp. 432–438, 2007.

[19] C. Adams *et al.*, "The Long-Baseline Neutrino Experiment: Exploring Fundamental Symmetries of the Universe." arXiv:1307.7335 [hep-ex], 2013.

[20] C. Andreopoulos *et al.*, "The GENIE Neutrino Monte Carlo Generator," *Nucl. Instrum. Meth.*, vol. A614, pp. 87–104, 2010.

[21] X. Qian, A. Tan, W. Wang, J. Ling, R. McKeown, *et al.*, "Statistical Evaluation of Experimental Determinations of Neutrino Mass Hierarchy," *Phys.Rev.*, vol. D86, p. 113011, 2012.

[22] M. Blennow, P. Coloma, P. Huber, and T. Schwetz, "Quantifying the sensitivity of oscillation experiments to the neutrino mass ordering," *JHEP*, vol. 1403, p. 028, 2014.

[23] C. Jarlskog, "A Basis Independent Formulation of the Connection Between Quark Mass Matrices, CP Violation and Experiment," *Z.Phys.*, vol. C29, pp. 491–497, 1985.

[24] J. Beringer *et al.*, "Review of Particle Physics (RPP)," *Phys.Rev.*, vol. D86, p. 010001, 2012.

[25] W. Marciano and Z. Parsa, "Intense neutrino beams and leptonic CP violation," *Nucl.Phys.Proc.Suppl.*, vol. 221, pp. 166–172, 2011.

[26] K. Abe *et al.*, "Measurements of neutrino oscillation in appearance and disappearance channels by the T2K experiment with 6.6E20 protons on target," *Phys.Rev.*, vol. D91, no. 7, p. 072010, 2015.

[27] C. Zhang, "Recent Results From The Daya Bay Experiment." 2015.

[28] A. Sousa, "First MINOS+ Data and New Results from MINOS." 2015.

[29] P. Adamson *et al.*, "Electron neutrino and antineutrino appearance in the full MINOS data sample," *Phys.Rev.Lett.*, vol. 110, no. 17, p. 171801, 2013.

[30] P. Adamson *et al.*, "Neutrino and Antineutrino Inclusive Charged-current Cross Section Measurements with the MINOS Near Detector," *Phys.Rev.*, vol. D81, p. 072002, 2010.

[31] L. Aliaga *et al.*, "Design, Calibration, and Performance of the MINERvA Detector," *Nucl.Instrum.Meth.*, vol. A743, pp. 130–159, 2014.

[32] C. Adams, J. Alonso, A. Ankowski, J. Asaadi, J. Ashenfelter, *et al.*, "The Intermediate Neutrino Program." 2015.

[33] M. Day and K. S. McFarland, "Differences in quasielastic cross sections of muon and electron neutrinos," *Phys. Rev. D*, vol. 86, p. 053003, Sep 2012.

[34] U. Mosel, O. Lalakulich, and K. Gallmeister, "Energy reconstruction in the long-baseline neutrino experiment," *Phys. Rev. Lett.*, vol. 112, p. 151802, Apr 2014.

[35] M. Antonello *et al.*, "A Proposal for a Three Detector Short-Baseline Neutrino Oscillation Program in the Fermilab Booster Neutrino Beam." 2015.

[36] C. Adams, C. Andreopoulos, J. Asaadi, B. Baller, M. Bishai, *et al.*, "LAr1-ND: Testing Neutrino Anomalies with Multiple LAr TPC Detectors at Fermilab." 2013.

[37] MicroBooNE Collaboration, "The MicroBooNE Technical Design Report." `http://microboone-docdb.fnal.gov/cgi-bin/ShowDocument?docid=1821`, 2012.

[38] C. Rubbia, M. Antonello, P. Aprili, B. Baibussinov, M. B. Ceolin, *et al.*, "Underground operation of the ICARUS T600 LAr-TPC: first results," *JINST*, vol. 6, p. P07011, 2011.

[39] P. Adamson *et al.*, "LArIAT: Liquid Argon TPC in a Test Beam." FERMILAB-PROPOSAL-1034, 2013.

[40] H. Berns *et al.*, "The CAPTAIN Detector and Physics Program." 2013.

[41] Q. Wu *et al.*, "A Precise measurement of the muon neutrino-nucleon inclusive charged current cross-section off an isoscalar target in the energy range $2.5 < E(nu) < 40$-GeV by NOMAD," *Phys.Lett.*, vol. B660, pp. 19–25, 2008.

[42] V. Lyubushkin *et al.*, "A Study of quasi-elastic muon neutrino and antineutrino scattering in the NOMAD experiment," *Eur.Phys.J.*, vol. C63, pp. 355–381, 2009.

[43] S. Mishra, R. Petti, and C. Rosenfeld, "A High Resolution Neutrino Experiment in a Mag-

netic Field for Project-X at Fermilab," *PoS*, vol. NUFACT08, p. 069, 2008.

[44] "Hadron Production Measurements for Fermilab Neutrino Beams," 2014. Addendum to NA61 SPSC-P-330 `https://cds.cern.ch/record/1955140/files/SPSC-P-330-ADD-7.pdf`.

[45] D. Rein and L. M. Sehgal, "Coherent pion production in neutrino reactions," *Nuclear Physics B*, vol. 223, no. 1, pp. 29 – 44, 1983.

[46] C. Berger and L. M. Sehgal, "Partially conserved axial vector current and coherent pion production by low energy neutrinos," *Phys. Rev. D*, vol. 79, p. 053003, Mar 2009.

[47] L. Alvarez-Ruso, L. S. Geng, S. Hirenzaki, and M. J. V. Vacas, "Charged current neutrino-induced coherent pion production," *Phys. Rev. C*, vol. 75, p. 055501, May 2007.

[48] L. Alvarez-Ruso, L. S. Geng, and M. J. V. Vacas, "Neutral current coherent pion production," *Phys. Rev. C*, vol. 76, p. 068501, Dec 2007.

[49] A. Higuera *et al.*, "Measurement of Coherent Production of $\pi^{\pm}$ in Neutrino and Antineutrino Beams on Carbon from E_{ν} of 1.5 to 20 GeV," *Phys.Rev.Lett.*, vol. 113, no. 26, p. 261802, 2014.

[50] B. Eberly *et al.*, "Charged Pion Production in ν_{μ} Interactions on Hydrocarbon at $\langle E_{\nu} \rangle$= 4.0 GeV." 2014.

[51] L. Aliaga, O. Altinok, A. Bercellie, A. Bodek, A. Bravar, *et al.*, "Single neutral pion production by charged-current $\bar{\nu}_{\mu}$ interactions on hydrocarbon at $\langle E_{\nu} \rangle$ = 3.6 GeV." 2015.

[52] E. Hernández, J. Nieves, and M. Valverde, "Weak pion production off the nucleon," *Phys. Rev. D*, vol. 76, p. 033005, Aug 2007.

[53] B. Tice *et al.*, "Measurement of Ratios of ν_{μ} Charged-Current Cross Sections on C, Fe, and Pb to CH at Neutrino Energies 2-20 GeV," *Phys.Rev.Lett.*, vol. 112, no. 23, p. 231801, 2014.

[54] L. Alvarez-Ruso, Y. Hayato, and J. Nieves, "Progress and open questions in the physics of neutrino cross sections at intermediate energies," *New Journal of Physics*, vol. 16, no. 7, p. 075015, 2014.

[55] S. Dytman and A. Meyer, "Final state interactions in GENIE," *AIP Conf.Proc.*, vol. 1405, pp. 213–218, 2011.

[56] O. Buss, T. Gaitanos, K. Gallmeister, H. van Hees, M. Kaskulov, *et al.*, "Transport-theoretical Description of Nuclear Reactions," *Phys.Rept.*, vol. 512, pp. 1–124, 2012.

[57] O. Benhar, F. Garibaldi, G. Urciuoli, C. Mariani, C. Jen, *et al.*, "Measurement of the Spectral Function of ^{40}Ar through the $(e, e'p)$ reaction." 2014.

[58] M. Bass, "Neutrino Oscillation Parameter Sensitivity in Future Long-Baseline Experiments,"

[59] K. Anderson, B. Bernstein, D. Boehnlein, K. R. Bourkland, S. Childress, *et al.*, "The NuMI Facility Technical Design Report," 1998.

[60] S. Agarwalla *et al.*, "Optimised sensitivity to leptonic CP violation from spectral information: the LBNO case at 2300 km baseline," 2014.

[61] S. Mikheev and A. Y. Smirnov, "Resonance Amplification of Oscillations in Matter and Spectroscopy of Solar Neutrinos," *Sov.J.Nucl.Phys.*, vol. 42, pp. 913–917, 1985.

[62] L. Wolfenstein, "Neutrino Oscillations in Matter," *Phys.Rev.*, vol. D17, pp. 2369–2374, 1978.

[63] J. Valle, "Resonant Oscillations of Massless Neutrinos in Matter," *Phys.Lett.*, vol. B199, p. 432, 1987.

[64] E. Roulet, "MSW effect with flavor changing neutrino interactions," *Phys.Rev.*, vol. D44, pp. 935–938, 1991.

[65] S. Davidson, C. Pena-Garay, N. Rius, and A. Santamaria, "Present and future bounds on nonstandard neutrino interactions," *JHEP*, vol. 0303, p. 011, 2003.

[66] M. Gonzalez-Garcia and M. Maltoni, "Phenomenology with Massive Neutrinos," *Phys.Rept.*, vol. 460, pp. 1–129, 2008.

[67] C. Biggio, M. Blennow, and E. Fernandez-Martinez, "General bounds on non-standard neutrino interactions," *JHEP*, vol. 0908, p. 090, 2009.

[68] J. Barranco, O. Miranda, C. Moura, and J. Valle, "Constraining non-standard neutrino-electron interactions," *Phys.Rev.*, vol. D77, p. 093014, 2008.

[69] F. Escrihuela, M. Tortola, J. Valle, and O. Miranda, "Global constraints on muon-neutrino non-standard interactions," *Phys.Rev.*, vol. D83, p. 093002, 2011.

[70] H. Davoudiasl, H.-S. Lee, and W. J. Marciano, "Long-Range Lepton Flavor Interactions and Neutrino Oscillations," *Phys.Rev.*, vol. D84, p. 013009, 2011.

[71] A. Aguilar-Arevalo *et al.*, "Evidence for neutrino oscillations from the observation of anti-neutrino(electron) appearance in a anti-neutrino(muon) beam," *Phys.Rev.*, vol. D64, p. 112007, 2001.

[72] A. Aguilar-Arevalo *et al.*, "A Search for electron neutrino appearance at the $\Delta m^2 \sim 1 \text{eV}^2$ scale," *Phys.Rev.Lett.*, vol. 98, p. 231801, 2007.

[73] A. Aguilar-Arevalo *et al.*, "Improved Search for $\bar{\nu}_\mu \rightarrow \bar{\nu}_e$ Oscillations in the MiniBooNE Experiment," *Phys.Rev.Lett.*, vol. 110, p. 161801, 2013.

[74] G. Mention, M. Fechner, T. Lasserre, T. Mueller, D. Lhuillier, *et al.*, "The Reactor Antineutrino Anomaly," *Phys.Rev.*, vol. D83, p. 073006, 2011.

[75] C. Giunti and M. Laveder, "Statistical Significance of the Gallium Anomaly," *Phys.Rev.*, vol. C83, p. 065504, 2011.

[76] P. Adamson *et al.*, "Active to sterile neutrino mixing limits from neutral-current interactions in MINOS," *Phys.Rev.Lett.*, vol. 107, p. 011802, 2011.

[77] N. Klop and A. Palazzo, "Imprints of CP violation induced by sterile neutrinos in T2K," *Phys.Rev.*, vol. D91, no. 7, p. 073017, 2015.

[78] D. Hollander and I. Mocioiu, "Minimal 3+2 sterile neutrino model at LBNE," *Phys.Rev.*, vol. D91, no. 1, p. 013002, 2015.

[79] P. Machado, H. Nunokawa, F. P. d. Santos, and R. Z. Funchal, "Large Extra Dimensions and Neutrino Oscillations." 2011.

[80] D. Colladay and V. A. Kostelecky, "CPT violation and the standard model," *Phys.Rev.*, vol. D55, pp. 6760–6774, 1997.

[81] D. Colladay and V. A. Kostelecky, "Lorentz violating extension of the standard model," *Phys.Rev.*, vol. D58, p. 116002, 1998.

[82] V. A. Kostelecky, "Gravity, Lorentz violation, and the standard model," *Phys.Rev.*, vol. D69, p. 105009, 2004.

[83] V. A. Kostelecky and M. Mewes, "Lorentz and CPT violation in neutrinos," *Phys.Rev.*, vol. D69, p. 016005, 2004.

[84] A. Kostelecky and M. Mewes, "Neutrinos with Lorentz-violating operators of arbitrary dimension," *Phys.Rev.*, vol. D85, p. 096005, 2012.

[85] Diwan, M. and others, "Draft LBNF/DUNE requirements spreadsheet," tech. rep., 2015. DUNE DocDB 112.

[86] J. C. Pati and A. Salam, "Is Baryon Number Conserved?," *Phys.Rev.Lett.*, vol. 31, pp. 661–664, 1973.

[87] H. Georgi and S. Glashow, "Unity of All Elementary Particle Forces," *Phys.Rev.Lett.*, vol. 32, pp. 438–441, 1974.

[88] S. Dimopoulos, S. Raby, and F. Wilczek, "Proton Decay in Supersymmetric Models," *Phys.Lett.*, vol. B112, p. 133, 1982.

[89] P. Langacker, "Grand Unified Theories and Proton Decay," *Phys.Rept.*, vol. 72, p. 185, 1981.

[90] W. de Boer, "Grand unified theories and supersymmetry in particle physics and cosmology," *Prog.Part.Nucl.Phys.*, vol. 33, pp. 201–302, 1994.

[91] P. Nath and P. Fileviez Perez, "Proton stability in grand unified theories, in strings and in branes," *Phys.Rept.*, vol. 441, pp. 191–317, 2007.

[92] A. Bernstein *et al.*, "Report on the Depth Requirements for a Massive Detector at Homestake (LBNE:DocDB-34)," 2009. arXiv:0907.4183 [hep-ex].

[93] S. Raby, T. Walker, K. Babu, H. Baer, A. Balantekin, *et al.*, "DUSEL Theory White Paper," 2008.

[94] G. Senjanovic, "Proton decay and grand unification," *AIP Conf.Proc.*, vol. 1200, pp. 131–141, 2010.

[95] T. Li, D. V. Nanopoulos, and J. W. Walker, "Elements of F-ast Proton Decay," *Nucl.Phys.*, vol. B846, pp. 43–99, 2011.

[96] H. Nishino *et al.*, "Search for Nucleon Decay into Charged Anti-lepton plus Meson in Super-Kamiokande I and II," *Phys.Rev.*, vol. D85, p. 112001, 2012.

[97] A. Bueno, Z. Dai, Y. Ge, M. Laffranchi, A. Melgarejo, *et al.*, "Nucleon decay searches with large liquid argon TPC detectors at shallow depths: Atmospheric neutrinos and cosmogenic backgrounds," *JHEP*, vol. 0704, p. 041, 2007.

[98] J. Klinger, V. Kudryavtsev, M. Richardson, and N. Spooner, "Muon-induced background to proton decay in the $p \rightarrow K^+\nu$ decay channel with large underground liquid argon TPC detectors," 2015.

[99] E. Kearns, "Future Experiments for Proton Decay. Presentation at ISOUPS (International Symposium: Opportunities in Underground Physics for Snowmass), Asilomar, May 2013," 2013.

[100] D. Stefan and A. M. Ankowski, "Nuclear effects in proton decay," *Acta Phys.Polon.*, vol. B40, pp. 671–674, 2009.

[101] S. Amerio *et al.*, "Design, construction and tests of the ICARUS T600 detector," *Nucl.Instrum.Meth.*, vol. A527, pp. 329–410, 2004.

[102] M. Antonello, B. Baibussinov, P. Benetti, E. Calligarich, N. Canci, *et al.*, "Precise 3D track reconstruction algorithm for the ICARUS T600 liquid argon time projection chamber detector," *Adv.High Energy Phys.*, vol. 2013, p. 260820, 2013.

[103] A. Blake, "Studying Atmospheric Neutrino Backgrounds to $p \rightarrow K^+\bar{\nu}$ Decay.," tech. rep., 2014. LBNE DocDB 8836.

[104] E. Kearns *et al.*, "Hyper-Kamiokande Physics Opportunities," 2013.

[105] A. Chatterjee, P. Mehta, D. Choudhury, and R. Gandhi, "Testing non-standard neutrino matter interactions in atmospheric neutrino propagation," 2014.

[106] K. Abe *et al.*, "Search for Matter-Dependent Atmospheric Neutrino Oscillations in Super-Kamiokande," *Phys.Rev.*, vol. D77, p. 052001, 2008.

[107] K. Abe *et al.*, "Limits on sterile neutrino mixing using atmospheric neutrinos in Super-Kamiokande," *Phys.Rev.*, vol. D91, p. 052019, 2015.

[108] W. H. Press and D. N. Spergel, "Capture by the sun of a galactic population of weakly interacting massive particles," *Astrophys.J.*, vol. 296, pp. 679–684, 1985.

[109] J. Silk, K. A. Olive, and M. Srednicki, "The Photino, the Sun and High-Energy Neutrinos," *Phys.Rev.Lett.*, vol. 55, pp. 257–259, 1985.

[110] T. Gaisser, G. Steigman, and S. Tilav, "Limits on Cold Dark Matter Candidates from Deep Underground Detectors," *Phys.Rev.*, vol. D34, p. 2206, 1986.

[111] A. Gould, "Resonant Enhancements in WIMP Capture by the Earth," *Astrophys.J.*, vol. 321, p. 571, 1987.

[112] M. Cirelli, N. Fornengo, T. Montaruli, I. A. Sokalski, A. Strumia, *et al.*, "Spectra of neutrinos from dark matter annihilations," *Nucl.Phys.*, vol. B727, pp. 99–138, 2005.

[113] M. Aartsen *et al.*, "Search for dark matter annihilations in the Sun with the 79-string IceCube detector," *Phys.Rev.Lett.*, vol. 110, no. 13, p. 131302, 2013.

[114] K. Choi *et al.*, "Search for neutrinos from annihilation of captured low-mass dark matter particles in the Sun by Super-Kamiokande," *Phys.Rev.Lett.*, vol. 114, no. 14, p. 141301, 2015.

[115] R. Bionta, G. Blewitt, C. Bratton, D. Casper, A. Ciocio, *et al.*, "Observation of a Neutrino Burst in Coincidence with Supernova SN 1987a in the Large Magellanic Cloud," *Phys.Rev.Lett.*, vol. 58, p. 1494, 1987.

[116] K. Hirata *et al.*, "Observation of a Neutrino Burst from the Supernova SN 1987a," *Phys.Rev.Lett.*, vol. 58, pp. 1490–1493, 1987.

[117] T. Fischer, S. Whitehouse, A. Mezzacappa, F.-K. Thielemann, and M. Liebendorfer, "Protoneutron star evolution and the neutrino driven wind in general relativistic neutrino radiation hydrodynamics simulations," *Astron.Astrophys.*, vol. 517, p. A80, 2010.

[118] M. Wurm *et al.*, "The next-generation liquid-scintillator neutrino observatory LENA," *Astropart.Phys.*, vol. 35, pp. 685–732, 2012.

[119] H. Minakata, H. Nunokawa, R. Tomas, and J. W. Valle, "Parameter Degeneracy in Flavor-Dependent Reconstruction of Supernova Neutrino Fluxes," *JCAP*, vol. 0812, p. 006, 2008.

[120] I. Tamborra, B. Muller, L. Hudepohl, H.-T. Janka, and G. Raffelt, "High-resolution supernova neutrino spectra represented by a simple fit," *Phys.Rev.*, vol. D86, p. 125031, 2012.

[121] I. Gil Botella and A. Rubbia, "Oscillation effects on supernova neutrino rates and spectra and detection of the shock breakout in a liquid argon TPC," *JCAP*, vol. 0310, p. 009, 2003.

[122] `http://www.phy.duke.edu/~schol/snowglobes`.

[123] A. Hayes. Private communication.

[124] S. Amoruso *et al.*, "Measurement of the mu decay spectrum with the ICARUS liquid argon TPC," *Eur.Phys.J.*, vol. C33, pp. 233–241, 2004.

[125] T. Totani, K. Sato, H. E. Dalhed, and J. R. Wilson, "Future detection of supernova neutrino burst and explosion mechanism," *Astrophys. J.*, vol. 496, pp. 216–225, 1998.

[126] J. Gava, J. Kneller, C. Volpe, and G. C. McLaughlin, "A dynamical collective calculation of supernova neutrino signals," *Phys. Rev. Lett.*, vol. 103, p. 071101, 2009.

[127] I. Tamborra, F. Hanke, H.-T. Janka, B. Mueller, G. G. Raffelt, *et al.*, "Self-sustained asymmetry of lepton-number emission: A new phenomenon during the supernova shock-accretion phase in three dimensions," *Astrophys.J.*, vol. 792, p. 96, 2014.

[128] L. Hudepohl, B. Muller, H.-T. Janka, A. Marek, and G. Raffelt, "Neutrino Signal of Electron-Capture Supernovae from Core Collapse to Cooling," *Phys.Rev.Lett.*, vol. 104, p. 251101, 2010.

[129] R. Laha and J. F. Beacom, "Gadolinium in water Cherenkov detectors improves detection of supernova ν_e," *Phys.Rev.*, vol. D89, p. 063007, 2014.

[130] R. Laha, J. F. Beacom, and S. K. Agarwalla, "New Power to Measure Supernova ν_e with Large Liquid Scintillator Detectors." arXiv:1412.8425 [hep-ph], 2014.

[131] K. Scholberg, "Supernova Neutrino Detection," *Ann.Rev.Nucl.Part.Sci.*, vol. 62, pp. 81–103, 2012.

[132] D. N. Schramm and J. W. Truran, "New physics from Supernova SN1987A," *Phys. Rept.*, vol. 189, pp. 89–126, 1990.

[133] G. G. Raffelt, "Particle Physics from Stars," *Ann. Rev. Nucl. Part. Sci.*, vol. 49, pp. 163–216, 1999.

[134] H. Duan, G. M. Fuller, and Y.-Z. Qian, "Collective neutrino flavor transformation in supernovae," *Phys.Rev.*, vol. D74, p. 123004, 2006.

[135] G. L. Fogli, E. Lisi, A. Marrone, and A. Mirizzi, "Collective neutrino flavor transitions in supernovae and the role of trajectory averaging," *JCAP*, vol. 0712, p. 010, 2007.

[136] G. G. Raffelt and A. Y. Smirnov, "Self-induced spectral splits in supernova neutrino fluxes," *Phys.Rev.*, vol. D76, p. 081301, 2007.

[137] G. G. Raffelt and A. Y. Smirnov, "Adiabaticity and spectral splits in collective neutrino transformations," *Phys.Rev.*, vol. D76, p. 125008, 2007.

[138] A. Esteban-Pretel, A. Mirizzi, S. Pastor, R. Tomas, G. Raffelt, *et al.*, "Role of dense matter in collective supernova neutrino transformations," *Phys.Rev.*, vol. D78, p. 085012, 2008.

[139] H. Duan and J. P. Kneller, "Neutrino flavour transformation in supernovae," *J.Phys.G*, vol. G36, p. 113201, 2009.

[140] B. Dasgupta, A. Dighe, G. G. Raffelt, and A. Y. Smirnov, "Multiple Spectral Splits of Supernova Neutrinos," *Phys.Rev.Lett.*, vol. 103, p. 051105, 2009.

[141] H. Duan, G. M. Fuller, and Y.-Z. Qian, "Collective Neutrino Oscillations," *Ann.Rev.Nucl.Part.Sci.*, vol. 60, pp. 569–594, 2010.

[142] H. Duan and A. Friedland, "Self-induced suppression of collective neutrino oscillations in a supernova," *Phys.Rev.Lett.*, vol. 106, p. 091101, 2011.

[143] M.-R. Wu, Y.-Z. Qian, G. Martinez-Pinedo, T. Fischer, and L. Huther, "Effects of neutrino oscillations on nucleosynthesis and neutrino signals for an 18 $M_\odot$ supernova model," *Phys.Rev.*, vol. D91, no. 6, p. 065016, 2015.

[144] S. Choubey, B. Dasgupta, A. Dighe, and A. Mirizzi, "Signatures of collective and matter effects on supernova neutrinos at large detectors." 2010.

[145] V. A. Kostelecky and M. Mewes, "Lorentz and CPT violation in the neutrino sector," *Phys.Rev.*, vol. D70, p. 031902, 2004.

[146] J. S. Diaz, V. A. Kostelecky, and M. Mewes, "Perturbative Lorentz and CPT violation for neutrino and antineutrino oscillations," *Phys.Rev.*, vol. D80, p. 076007, 2009.

[147] J. Diaz, A. Kostelecky, and M. Mewes. Private communication.

[148] F. Rossi-Torres, M. Guzzo, and E. Kemp, "Boundaries on Neutrino Mass from Supernovae Neutronization Burst by Liquid Argon Experiments," 2015.

[149] P. Keranen, J. Maalampi, M. Myyrylainen, and J. Riittinen, "Sterile neutrino signals from supernovae," *Phys.Rev.*, vol. D76, p. 125026, 2007.

[150] I. Tamborra, G. G. Raffelt, L. Hudepohl, and H.-T. Janka, "Impact of eV-mass sterile neutrinos on neutrino-driven supernova outflows," *JCAP*, vol. 1201, p. 013, 2012.

[151] A. Esmaili, O. Peres, and P. D. Serpico, "Impact of sterile neutrinos on the early time flux from a galactic supernova," *Phys.Rev.*, vol. D90, no. 3, p. 033013, 2014.

[152] J. F. Cherry, J. Carlson, A. Friedland, G. M. Fuller, and A. Vlasenko, "Halo Modification of a Supernova Neutronization Neutrino Burst," *Phys.Rev.*, vol. D87, p. 085037, 2013.

[153] J. F. Beacom, R. Boyd, and A. Mezzacappa, "Black hole formation in core collapse supernovae and time-of-flight measurements of the neutrino masses," *Phys.Rev.*, vol. D63, p. 073011, 2001.

[154] T. Fischer, S. C. Whitehouse, A. Mezzacappa, F. K. Thielemann, and M. Liebendorfer, "The neutrino signal from protoneutron star accretion and black hole formation." 2008.

[155] R. C. Schirato and G. M. Fuller, "Connection between supernova shocks, flavor transformation, and the neutrino signal." 2002.

[156] F. Hanke, A. Marek, B. Muller, and H.-T. Janka, "Is Strong SASI Activity the Key to Successful Neutrino-Driven Supernova Explosions?," *Astrophys.J.*, vol. 755, p. 138, 2012.

[157] F. Hanke, B. Mueller, A. Wongwathanarat, A. Marek, and H.-T. Janka, "SASI Activity in Three-Dimensional Neutrino-Hydrodynamics Simulations of Supernova Cores," *Astrophys.J.*, vol. 770, p. 66, 2013.

[158] A. Friedland and A. Gruzinov, "Neutrino signatures of supernova turbulence." 2006.

[159] T. Lund and J. P. Kneller, "Combining collective, MSW, and turbulence effects in supernova neutrino flavor evolution." 2013.

[160] N. Arnaud, M. Barsuglia, M.-A. Bizouard, V. Brisson, F. Cavalier, *et al.*, "Detection of a close supernova gravitational wave burst in a network of interferometers, neutrino and optical detectors," *Astropart.Phys.*, vol. 21, pp. 201–221, 2004.

[161] C. Ott, E. O'Connor, S. Gossan, E. Abdikamalov, U. Gamma, *et al.*, "Core-Collapse Supernovae, Neutrinos, and Gravitational Waves," *Nucl.Phys.Proc.Suppl.*, vol. 235-236, pp. 381–387, 2013.

[162] B. Mueller, H.-T. Janka, and A. Marek, "A New Multi-Dimensional General Relativistic Neutrino Hydrodynamics Code of Core-Collapse Supernovae III. Gravitational Wave Signals from Supernova Explosion Models," *Astrophys.J.*, vol. 766, p. 43, 2013.

[163] A. Nishizawa and T. Nakamura, "Measuring Speed of Gravitational Waves by Observations of Photons and Neutrinos from Compact Binary Mergers and Supernovae," *Phys.Rev.*, vol. D90, no. 4, p. 044048, 2014.

[164] P. Antonioli *et al.*, "Snews: The supernova early warning system," *New J. Phys.*, vol. 6, p. 114, 2004.

[165] K. Scholberg, "The SuperNova Early Warning System," *Astron. Nachr.*, vol. 329, pp. 337–339, 2008.

[166] A. Bueno, I. Gil Botella, and A. Rubbia, "Supernova neutrino detection in a liquid argon TPC." 2003.

[167] S. Fukuda *et al.*, "Solar B-8 and hep neutrino measurements from 1258 days of Super-Kamiokande data," *Phys.Rev.Lett.*, vol. 86, pp. 5651–5655, 2001.

[168] Q. Ahmad *et al.*, "Measurement of the rate of nu/e + d -> p + p + e- interactions produced by B-8 solar neutrinos at the Sudbury Neutrino Observatory," *Phys.Rev.Lett.*, vol. 87, p. 071301, 2001.

[169] B. Cleveland, T. Daily, J. Davis, Raymond, J. R. Distel, K. Lande, *et al.*, "Measurement of the solar electron neutrino flux with the Homestake chlorine detector," *Astrophys.J.*, vol. 496, pp. 505–526, 1998.

[170] A. Guglielmi, "Status and early events from ICARUS T600," *Nucl.Phys*, vol. B (Proc. Suppl.) 229-232, pp. 342–346, 2012.

[171] A. Renshaw *et al.*, "First Indication of Terrestrial Matter Effects on Solar Neutrino Oscillation," *Phys.Rev.Lett.*, vol. 112, no. 9, p. 091805, 2014.

[172] J. F. Beacom, "The Diffuse Supernova Neutrino Background," *Ann.Rev.Nucl.Part.Sci.*, vol. 60, pp. 439–462, 2010.

[173] A. Cocco, A. Ereditato, G. Fiorillo, G. Mangano, and V. Pettorino, "Supernova relic neutrinos in liquid argon detectors," *JCAP*, vol. 0412, p. 002, 2004.

[174] D. Barker, D. Mei, and C. Zhang, "Muon-Induced Background Study for an Argon-Based Long Baseline Neutrino Experiment," *Phys.Rev.*, vol. D86, p. 054001, 2012.

[175] O. Caballero, G. McLaughlin, and R. Surman, "Neutrino Spectra from Accretion Disks: Neutrino General Relativistic Effects and the Consequences for Nucleosynthesis," *Astrophys.J.*, vol. 745, p. 170, 2012.

[176] O. Caballero, G. McLaughlin, R. Surman, and R. Surman, "Detecting neutrinos from black hole neutron stars mergers," *Phys.Rev.*, vol. D80, p. 123004, 2009.

[177] C. Rott, J. Siegal-Gaskins, and J. F. Beacom, "New Sensitivity to Solar WIMP Annihilation using Low-Energy Neutrinos," *Phys.Rev.*, vol. D88, p. 055005, 2013.

[178] N. Bernal, J. Martĩŋn-Albo, and S. Palomares-Ruiz, "A novel way of constraining WIMPs annihilations in the Sun: MeV neutrinos," *JCAP*, vol. 1308, p. 011, 2013.

[179] Gehman, V.M. and others, "Low-Energy Backgrounds," tech. rep., 2014. LBNE DocDB 9470.

[180] C. Andreopoulos *et al.*, "The GENIE Neutrino Monte Carlo Generator," *Nucl. Instrum. Methods*, vol. A, no. 614, pp. 87–104, 2010.

[181] R. Petti and G. Zeller, "Nuclear Effects in Water vs. Argon," tech. rep. LBNE-doc-740.

[182] G. Zeller, "Expected Event Rates in the LBNE Near Detector," tech. rep. LBNE-doc-783.

[183] S.R.Mishra, R.Petti and C. Rosenfeld, "A High Resolution Neutrino Experiment in a Magnetic Field for Project-X," 2008. `http://www.fnal.gov/directorate/Longrange/Steering_Public/community_letters.html`.

[184] B.Chowdhary. R.Gandhi, C.S.Mishra, S.R.Mishra, J.Strait, "Detailed Project Report. Proposal submitted to DAE/DST.," tech. rep., 2012. LBNE DocDB 6704.

[185] Xinchun Tian, S.R.Mishra and R.Petti, "Absolute Flux Constraints.," tech. rep., Univ. of South Carolina, 2014. LBNE DocDB 9240 & 9418.

[186] S.R. Mishra *et al.* [CCFR Collaboration] *Phys. Rev. Lett.*, vol. 63, p. 132, 1989.

[187] S.R. Mishra *et al.* [CCFR Collaboration] *Phys. Lett. B*, vol. 252, p. 170, 1990.

[188] P. Vilain *et al.* [CHARM-II Collaboration] *Phys. Lett. B*, vol. 364, p. 121, 1995.

[189] S.R.Mishra, "Probing Hadron Structure with Neutrino Experiments." Review talk presented at *Workshop on Hadron Structure Functions and Parton Distributions*, Fermilab, April, 1990; World Scientific, 84-123 (1990), Ed. D. Geesaman *et al.*; Nevis Preprint # 1426, June 1990.

[190] A. Bodek, U. Sarica, D. Naples, and L. Ren, "Methods to Determine Neutrino Flux at Low Energies:Investigation of the Low ν Method," *Eur.Phys.J.*, vol. C72, p. 1973, 2012.